

学位論文

Observational studies on wet deposition mechanism
of black carbon particles

(ブラックカーボン粒子の湿性除去メカニズム
の観測的研究)

平成 28 年 12 月博士（理学）申請

東京大学大学院理学系研究科

地球惑星科学専攻

森 樹大

Abstract

1. Introduction

Black carbon (BC) aerosols are a type of carbonaceous aerosol emitted by incomplete combustion of fossil fuels and biomass. They strongly absorb solar radiation in the troposphere and heat the atmosphere. In addition, BC particles deposited onto snow-covered polar and mountainous regions accelerate snowmelt in these regions. However, there are large uncertainties in the prediction of the climate effects of BC because estimates of BC vertical distribution in the troposphere vary greatly among global climate models. One of the largest sources of uncertainty in predicted BC mass concentration and its vertical profile is in the global models' simplified treatment of the wet removal process. To improve the treatment of the BC wet removal process in the global models, a new observational approach for specifying the key process and parameter controlling the wet removal efficiency of BC is required.

This dissertation describes a new observational approach combining simultaneous observational methods for measuring the size distributions of BC in air and rainwater with data analysis methods to elucidate the key process and parameter controlling the wet removal efficiency of BC for each rain event.

2. Method

First, a new method for measuring the number and mass size distributions of BC particles suspended in rainwater was established. Second, theoretical and experimental evidence was provided to show that the BC size distribution in water changed little during cloud-precipitation processes and sample storage. Third, a data analysis method using a cloud parcel model was developed to infer the relative contributions of three distinct BC scavenging mechanisms (below-cloud impaction, nucleation, and

in-cloud impaction) in a precipitating cloud based on the measured size-dependence of wet removal efficiency.

2.1. Measurement methods

A standard single-particle soot photometer (SP2) measured the size-resolved number concentrations of BC in the air and the shell/core ratio (SCR: the ratio of the shell diameter of BC-containing particles to BC-core diameter). BC diameter is defined as a mass equivalent diameter (D_{BC}). A new measurement system combined a pneumatic nebulizer (Marin-5) with the SP2 enabled accurate measurement of the size-resolved number concentration of BC in rainwater. The extraction efficiency of the nebulizer was as high as 50% on average within the $70 < D_{BC} < 2000$ nm range, which is consistent with theoretical estimates. This measurement system was applied to the simultaneous measurement of size-resolved number concentrations in air and rainwater to observe D_{BC} -dependence of wet removal efficiency ($RE(D_{BC})$). It was defined as the ratio of size-resolved number concentration in rainwater to that in air.

2.2. Data analysis method

The data analysis method focused on the air parcel ascending from the atmospheric planetary boundary layer to the free troposphere via the moist convective process. BC particles within the air parcel are scavenged by below-cloud impaction, nucleation, and in-cloud impaction mechanisms. To investigate the relative contribution of the three scavenging mechanisms, three distinct scavenged number fractions of BC were calculated, assuming the updraft velocity (w) of the air parcel and the residence time (t) in a precipitating cloud. The optimum combination (w , t) was selected under the constraints of the measured D_{BC} -dependent wet removal efficiency and other observational data to explore the key mechanism controlling the BC wet removal efficiency for each rain event.

3. Results and Discussions

The new observational approach was applied at two observation sites: Hongo-campus of University of Tokyo and Cape Hedo in Okinawa, where fresh and aged pollutants are dominant, respectively. The D_{BC} dependence of $RE(D_{BC})$ showed remarkable differences depending on the precipitation event: in Tokyo, the $RE(D_{BC})$ often increased steeply with D_{BC} , but in Okinawa, such D_{BC} dependence was seldom observed. Comparing the relationship between D_{BC} dependence of $RE(D_{BC})$ and D_{BC} dependence of number fractions scavenged by nucleation and impaction mechanisms, the nucleation scavenging mechanism was almost dominant for BC-containing particles with $D_{BC} > 100$ nm. For a median $SCr > 1.2$ ($D_{BC}=200$ nm), BC-containing particles were efficiently removed by nucleation scavenging mechanism, independent of the hygroscopicity for BC-coating materials ($\kappa_{BC-coat}$) and maximum supersaturation (SS_{max}) in air. For a median $SCr < 1.1$ ($D_{BC}=200$ nm), the D_{BC} dependence of $RE(D_{BC})$ varied greatly, which was controlled by the change of cloud-condensation nuclei number fraction depending on $\kappa_{BC-coat}$ and SS_{max} . In other words, BC-containing particles with a median critical supersaturation (Sc) $< 0.1\%$ were efficiently scavenged by nucleation mechanism, whereas for a median $Sc > 0.1\%$, the D_{BC} dependence of $RE(D_{BC})$ varied greatly, which is calculated by using a median $SCr=1.2$ (for $D_{BC}=200$ nm) and average $\kappa_{BC-coat}$ (= 0.3).

4. Conclusion

This dissertation revealed that nucleation scavenging was the dominant mechanism for BC-containing particles with $D_{BC} > 100$ nm in precipitating clouds, and the key parameter controlling the nucleation scavenging was SCr . The wet removal efficiency of BC was almost 1 for thickly coated BC particles (median $SCr > 1.2$), whereas the efficiency for thinly coated BC particles (median $SCr < 1.1$) was highly variable, depending on SCr , $\kappa_{BC-coat}$ and SS_{max} .

To implement numerical simulation of BC wet removal in 3-D atmospheric aerosol models,

the resolution of SCr , $\kappa_{BC-coat}$, and SS_{max} should be improved for a median $SCr < 1.1$, especially in urban areas. Moreover, the development of a parameterization scheme classifying the removal and transport of aerosol particles by the Sc ($=0.1$) value will improve estimates of spatial and temporal distributions of not only BC but also other aerosol particles.

Contents

1. General Introduction.....	1
1.1. Atmospheric Aerosols.....	1
1.2. Climate Effects of BC.....	1
1.3.Current Issues.....	2
1.3.1. Global BC Mass Concentration.....	2
1.3.2. Treatment of Wet Removal Process in Aerosol Models.....	3
1.3.3. Observational Implications on the Wet Removal Process.....	4
1.4.Aim of this Dissertation.....	5
2. Establishment of New Observational Methods and Development of Data Analysis Methods.....	6
2.1 Measurement Method.....	6
2.1.1 Experimental Introduction.....	6
2.1.2 Methods.....	9
2.1.2.1 Nebulizer/Wide-Range SP2 Setup.....	9
2.1.2.2 Single-Particle Soot Photometer.....	11
2.1.2.2.1 Instrument Configuration.....	11
2.1.2.2.2 Selective Detection of Black Carbon Particles.....	12
2.1.2.3 Wide-Range SP2.....	15
2.1.2.3.1 Calibration of BC.....	15
2.1.2.3.2 Overall Performance of the WR-SP2.....	18
2.1.3 Methods: Extraction Efficiency of Marin-5.....	19
2.1.3.1 Theoretically-Estimated Extraction Efficiency.....	20

2.1.3.2	Extraction Efficiency	23
2.1.3.2.1	Number Concentration of Polystyrene Latex Spheres in Water.....	23
2.1.3.2.2	Extraction Efficiency with PSL Spheres and AquaBlack 162.....	23
2.1.4	Reproducibility	26
2.1.5	Estimates of Aerosolized Volume Fraction in the Marin-5 and the Droplet Distribution	27
2.1.5.1	Aerosolized Volume Fraction in the Marin-5.....	27
2.1.5.2	Droplet size distribution.....	30
2.1.6	Changes in BC size in the nebulizer	31
2.1.6.1	Experimental evaluation.....	31
2.1.6.2	Theoretical evaluation.....	34
2.1.7	Changes in BC particle size in cloud droplets	34
2.1.8	Size distribution of BC particles in rainwater	38
2.1.9	Experimental Setup for Observation	41
2.1.10	Experimental Summary	42
2.2	Data Analysis Method	44
2.2.1	Method	44
2.2.2	Nucleation Scavenging of BC Particles	48
2.2.2.1	Determination of Maximum Supersaturation in Air.....	50
2.2.2.2	Theoretically-Estimated Dry Shell/Core Ratio	51
2.2.3	Impaction Scavenging of BC Particles	53

2.2.4	Summary.....	56
3	Field Observation on Wet Removal Mechanism of Black Carbon in Tokyo and Okinawa.....	57
3.1	Observation Site.....	57
3.2	Results and Discussion.....	57
3.2.1	Meteorological Conditions.....	57
3.2.2	Vertical and Horizontal Aerosol Distributions.....	59
3.2.3	Dry Shell/Core Ratio and Chemical Compositions.....	60
3.2.4	Observed Wet Removal Efficiency.....	61
3.2.5	Relative Contribution of Scavenging Mechanisms of BC.....	62
3.2.6	Key Parameter Controlling Nucleation Scavenging of BC.....	68
3.2.7	Estimated Transport Efficiency of BC.....	69
3.2.8	Understandings of BC Vertical Transport Using Aircraft Observation Data.....	72
3.2.9	Uncertainty in Estimates Using the Data Analysis Method.....	74
3.2.9.1	Uncertainty in Estimate of F_{CCN} , $F_{bc(ic)-imp}$, and TE_{cal}	74
3.2.9.2	Uncertainty in Estimate of TE_{cal} due to Distribution of Updraft Velocity.....	75
3.2.9.3	Uncertainty in Estimate of F_{CCN} for BC-containing Particles with Organic Compounds.....	75
3.3	Summary.....	76
4	General Conclusions.....	79

Appendix.....	84
AppendixA1: Data-Processing Procedure for Calculating the Scavenged Number Fractions of BC	84
AppendixA1.1: Detailed calculation method of F_{bc-imp} and F_{ic-imp}	84
AppendixA1.2: Detailed calculation method of F_{ccn}	88
AppendixA2: Observed and Estimated Values in Tokyo and Okinawa.....	92
AppendixA3: Wet Deposition of Black Carbon at a Remote Site in the East China Sea.....	93
AppendixA4.....	122
References.....	125
Acknowledgements.....	138
Publication List.....	139

1. General Introduction

1.1. Atmospheric Aerosols

Atmospheric aerosols consisting of inorganic compounds (i.e. sulfate and nitrate), organic compounds, black carbon (BC), mineral dust, and sea salt, perturb radiation budget through various mechanisms. Major compounds such as sea salt and sulfates, serve as cloud-condensation nuclei (CCN) and effectively scatter sunlight. These aerosols reduce net downward radiation at the top of the atmosphere (TOA) by directly backscattering solar radiation and increasing cloud albedo via the Twomey effect [Twomey, 1974; Lohmann and Feichter, 2005].

Despite of their minority in terms of globally-averaged mass loading, strongly-light absorbing aerosol compounds such as BC and iron-oxide in mineral dust disturb the regional and global climates via different mechanisms. Sunlight absorption by aerosols in the troposphere and in snowpack increases net downward radiation at the TOA, and aerosol-induced heating of the troposphere affects the hydrologic cycle and cloudiness, depending on altitude and meteorological conditions [Ming and Persad, 2010; Hondnebrog and Samset, 2014]. The light-absorbing aerosols deposited onto snow-covered polar and mountainous regions accelerates snowmelt and reduce surface albedo in these region [Warren and Wiscombe, 1980; Hadley and Kirchstetter, 2012].

This dissertation focuses on BC, especially on the wet removal process which controls the global abundance and long-range transport of BC.

1.2 Climate Effects of BC

The BC is water-insoluble refractory compounds emitted from combustions of various

kind of fossil fuel and biomass, and is the most important light-absorbing compound in atmospheric aerosols [Bond et al., 2013]. In terms of globally-averaged direct radiative forcing at TOA, BC is estimated to be the third important contributor to positive forcing ($0.64\pm 0.58\text{Wm}^{-2}$), which is about 1/3 of total radiative forcing due to CO_2 [Intergovernmental Panel on Climate Change, 2013]. Global model's predictions of global-mean precipitation change associated with global-warming are sensitive to the BC emission scenario [Pendergrass and Hartmann, 2012]. Several model and observational studies suggest that monsoon precipitation patterns in and near Indian and Asian regions are substantially altered by atmospheric heating by BC [Menon et al., 2002; D'Errico et al., 2015]. In addition, BC is expected to be the most important agent of snow-darkening in most of sub-arctic and polar regions [Yasunari et al., 2015]. To understand the complex mechanisms by which BC perturbs the climate system, we need 3D-atmospheric aerosol models fully coupling dynamical, radiative, and chemical processes and their observational verifications.

1.3. Current Issues

1.3.1 Global BC Mass Concentration

In the framework of Aerosol Comparisons between Observations and Models (AeroCom) international project, the vertical concentration profiles of BC mass predicted by 13 different aerosol models were compared with observation data from four recent aircraft observation campaigns [Samset et al., 2014]. Predicted BC mass concentration typically differs greatly from observational data, and the disagreement of predicted BC concentration among different models is about one or two orders of magnitude. The global dataset of aerosol absorption optical depth (AAOD) provided by the ground-based remote

sensing network (Aerosol Robotic Network: AERONET, [Dubovik et al., 2002]) is also used to test the model's prediction of AAOD by BC. Bond et al. [2013] showed that the AeroCom models underestimated global BC-AAOD by a factor of about 3. These comparison results from the AeroCom project revealed large room for improvement in the model's ability to predict BC mass concentration.

One of the largest sources of uncertainty in predicted BC mass concentration is derived from the model's treatment of the wet removal process [Textor et al., 2006], as revealed from the sensitivity of predicted BC vertical distribution to the model's assumptions related to wet removal [Park et al. 2005]. The wet removal of aerosols in precipitating cloud systems is a multi-scale phenomenon wherein various chemical, microphysical, fluid dynamic, and thermodynamic processes strongly interact [Flossmann and Wobrock 2010]. An accurate first-principle numerical simulation from the regional to global atmosphere might be impossible even in the future. Thus, any atmospheric models used in climate studies need to adopt somewhat crude assumptions for the wet removal process.

1.3.2. Treatment of Wet Removal Process in Aerosol Models

The majority of current models attribute BC to either hydrophilic or hydrophobic BC, and assume that only hydrophilic BC is removed when precipitation occurs within each spatial grid [Donner et al., 2011; Lamarque et al., 2012; Sato et al., 2016]. This parameterization scheme is intended to simplify the simulation of the physical process by which the particles with lower critical supersaturation are preferentially incorporated into cloud droplets and removed by precipitation.

Recently, several attempts have been made to explicitly simulate changes in the

CCN activity of BC through aging processes in the atmosphere, by resolving the mixing state of BC with other inorganic and organic aerosols [Riemer et al., 2009, 2010; Oshima et al., 2009; Zaveri et al., 2010]. For example, Riemer et al. [2009] developed a particle-resolved aerosol box model (PartMC-MOSAIC) to simulate the time evolution of the particle mixing state in Lagrangian air parcel by explicitly calculating the condensation and coagulation processes experienced by individual particles. Because of the huge computational and memory costs, this type of particle-resolved model cannot be applied to 3D atmospheric models for climate studies. Some recent 3D atmospheric aerosol models also have attempted to resolve the BC mixing state in a less-detailed manner [Jacobson.2000, 2001; Bauer et al., 2008]. Jacobson [2001] simulated the evolution of the chemical composition of aerosols to treat the internal mixture of BC into the global model. Matsui et al. [2013a; 2014] developed a size- and BC-mixing-state-resolved 2D-bin aerosol module and applied it to the WRF-Chem atmospheric model.

Despite these efforts, little observational evidence has been collected to prove what type of sophisticated adjustments in models actually improve the prediction accuracy of BC wet removal process.

1.3.3. Observational Implications on the Wet Removal Process

Recent aircraft observations have showed that average BC particle size tends to be smaller in air masses which have experienced wet removal process [Moteki et al., 2012, Taylor et al. 2014; Kondo et al., 2016] during transport from the boundary layer to the free troposphere. These results show that the larger BC particles are removed more efficiently during precipitating moist convection, implying that the efficiency of wet removal of BC-containing aerosols is strongly affected by some particle-size dependent mechanisms.

Thus, it is very likely that some microphysical properties (e.g., particle size) of individual BC-containing particles actually affect wet removal efficiency through some physical mechanisms.

1.4. Aim of this Dissertation

At this stage, new observational results that would help to uncover the key process and parameter controlling BC wet removal efficiency are needed. Such observational results, if available, greatly helps to decide the strategy of further sophistications in current models. Such observational data would also be useful for testing various types of numerical simulation of wet removal processes.

This dissertation presents a novel observational approach for exploring the key process and parameter controlling the efficiency of BC wet removal. This approach can infer the relative contributions of three different physical mechanisms responsible for scavenging the BC-containing aerosols by water droplets, on the basis of the measured size-resolved number concentration of BC in air (before removal) and in rainwater (after removal). The contents of this dissertation are ordered as follows.

Chapter 2 presents the experimental and data analysis methods by which the observational approach is realized. A novel experimental procedure for measuring the size-resolved BC concentrations in rainwater, and other important experimental results are described in Chapter 2.1. An original data analysis method by which the relative contributions of BC scavenging mechanisms are inferred is described in Chapter 2.2. Chapter 3 presents observation results from two sites, Tokyo and Okinawa, wherein fresh and aged anthropogenic pollutants, respectively, can be sampled. Finally, Chapter 4 summarizes the important results and presents implications for future work.

2. Establishment of New Observational Methods and Development of Data Analysis Methods

2.1 Measurement Method

2.1.1 Experimental Introduction

BC mass concentration in rainwater has been measured by filter-based methods in many previous studies [Ogren et al., 1984; Dasch and Cadle, 1989; Ducret and Cachier, 1992; Armalis, 1999; Chýlek et al., 1999; Hadley et al., 2008; Cerqueira et al., 2010]. However, the microphysical properties (e.g., BC size: D_{BC}) of BC in rainwater have been unknown.

Recently, the size distribution and mass concentrations of BC particles in liquid water have been measured by a system consisting of an ultrasonic nebulizer (U5000AT: Cetac Technologies Inc., Omaha, NE, USA) and a single-particle soot photometer (SP2) in previous studies [McConnell et al., 2007; Ohata et al., 2011, 2013; Schwarz et al., 2012; Mori et al., 2014]. The U5000AT nebulizer converts the liquid water into small droplets on the surface of a piezoelectric transducer and dries the droplets to release some particles into the air. The extracted particles are transferred to the SP2, which measures the masses of individual BC particles by the laser-induced incandescence technique [Stephens et al., 2003; Moteki and Kondo, 2010]. The combined U5000AT/SP2 system can measure the size distribution and mass concentration of BC particles in rainwater and snow, typically requiring only 5 mL of liquid water sample [Ohata et al., 2011]. Ohata et al. [2011, 2013] and Mori et al. [2014] measured the size distributions of BC particles in rainwater and snow in two urban areas (Tokyo, 35.7°N, 139.8°E, and Sapporo, 43.1°N, 141.4°E) and at a remote site (Cape Hedo, 26.9°N, 128.7°E) in Japan. The extraction

efficiency of the U5000AT nebulizer is particle size dependent: Ohata et al. [2013] obtained an extraction efficiency of about 10% within the $200 < D_{BC} < 500$ nm range at the liquid and air flow rates used in their experiments, but for particles with $D_{BC} > 500$ nm, the extraction efficiency decreased sharply, resulting in large uncertainties in the measurement of BC size distributions.

Schwarz et al. [2012, 2013] observed a substantial fraction of BC particles within the $0.6 < D_{BC} < 2.0$ μm range in snow samples by using a collision-type nebulizer, suggesting the importance of measuring BC particles with $D_{BC} > 600$ nm and the necessity of improving extraction efficiency for large particle sizes. The extraction efficiency of the APEX-Q pneumatic nebulizer (Elemental Scientific Inc., Omaha, NE, USA) has been shown to be largely size independent within the $100 < D_{BC} < 1000$ nm range [Wendl et al., 2014]. Lim et al. [2014] measured the extraction efficiency of APEX-Q nebulizer to be about 72% within the $150 < D_{BC} < 600$ nm range at their flow rates. However, there are no demonstrated methods for accurately measuring the size distribution of BC particles with diameters up to a few micrometers in liquid water samples, for two main reasons. First, the extraction efficiencies of nebulizers for particles with $D_{BC} > 1.0$ μm have not been reliably evaluated. Second, incandescence signals of the SP2 used in previous studies were saturated for large BC particles (>1.0 μm) [Moteki and Kondo, 2010].

To overcome these difficulties, this Chapter 2.1 shows the expansion of the upper limit of the size range of BC particles detectable by SP2 and the combination of the SP2 with a pneumatic nebulizer for accurate measurements of BC particles with $D_{BC} < 2.0$ μm . Moreover, to better understand the wet deposition process of BC, possible changes in BC particle size during the condensational growth and nebulizer extraction process were experimentally and theoretically assessed. Finally, the simultaneous measurement of the

size-resolved BC mass concentrations in air and rainwater in Tokyo during summer 2014 was conducted to demonstrate reliability of the technique for field observation.

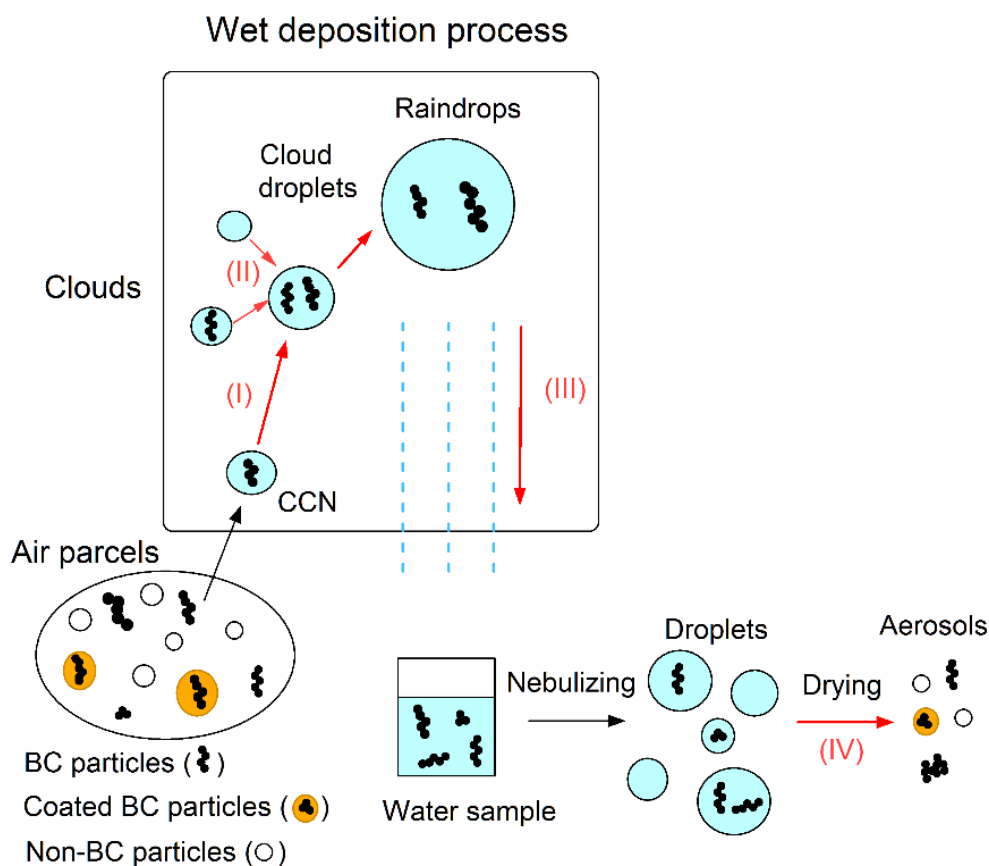


Figure 2.1. Schematic diagram of the wet deposition processes of BC and its extraction into air by a nebulizer: (I) growth of BC-containing particles into cloud droplets; (II) collision of cloud droplets; (III) formation of raindrops by coalescence of cloud droplets; (IV) extraction of BC from liquid water by the nebulizer. The size distributions and chemical composition of non-BC particles extracted by process (IV) are different from those in the air parcels.

2.1.2 Methods

Figure 2.1 illustrates the wet deposition processes of BC and its extraction from liquid water by a nebulizer. There are four important processes through which the sizes of BC particles might change: (I) Growth of BC-containing particles into cloud droplets, (II) collisional growth of cloud droplets, (III) formation of raindrops by coalescence, and (IV) extraction of BC particles from collected rainwater by the nebulizer. The effects of these processes are examined quantitatively in this chapter. First, the improved system for measuring the size distributions of BC particles in liquid water was described.

2.1.2.1 Nebulizer/Wide-Range SP2 Setup

Figure 2.2 shows the experimental setup for measuring the size distribution of BC particles in liquid water. The structure of the Marin-5 pneumatic nebulizer (Cetac Technologies Inc.) is shown in Figure 2.3. As shown in Figure 2.2, the water sample is fed into the Marin-5 nebulizer by a peristaltic pump (REGRO Analog; ISMATEC SA, Feldeggstrasse, Glatbrugg, Switzerland) at a constant flow rate ($V_{\text{pump}}: 3.0 \times 10^{-6} \text{ L s}^{-1}$). A portion of the introduced water is converted into droplets by the concentric pneumatic nebulizer, using dry air as the driving force at a constant flow rate ($F_{\text{neb}}: 16 \text{ cm}^3 \text{ s}^{-1}$ at standard temperature and pressure [STP]), and the diameters of the droplets are estimated (as described in section 2.1.5). Immediately after nebulization, the droplets are evaporated in a heated spray chamber at 140 °C, generating a mixture of BC particles, non-BC particles, and water vapor. A fraction of the non-aerosolized water sample is removed through the first drain. The particles and water vapor are transferred to a condenser at 3 °C. The water vapor condenses and is removed through the second and third drains. The extracted BC particles are introduced into a modified SP2 (a wide-range SP2; WR-SP2)

at a constant flow rate of $1.8 \text{ STP cm}^3 \text{ s}^{-1}$. The WR-SP2 measures the masses of individual BC particles with mass equivalent diameters between 70 and 4170 nm (Section 2.1.2.3).

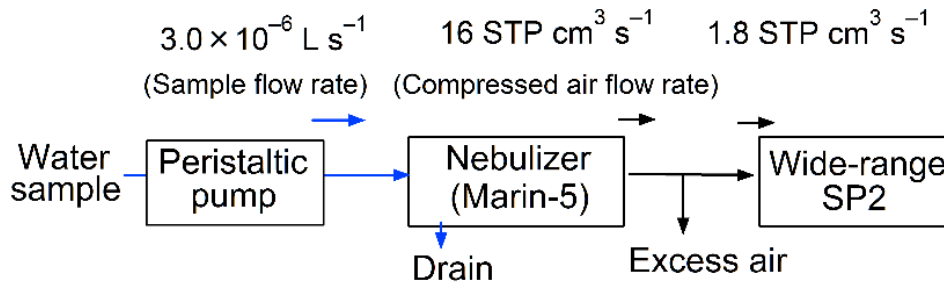


Figure 2.2. Experimental setup for measuring BC particles in rainwater and snow. Air flow rates are given in units of standard temperature and pressure (STP; 273 K and 1013 hPa) $\text{cm}^3 \text{ s}^{-1}$.

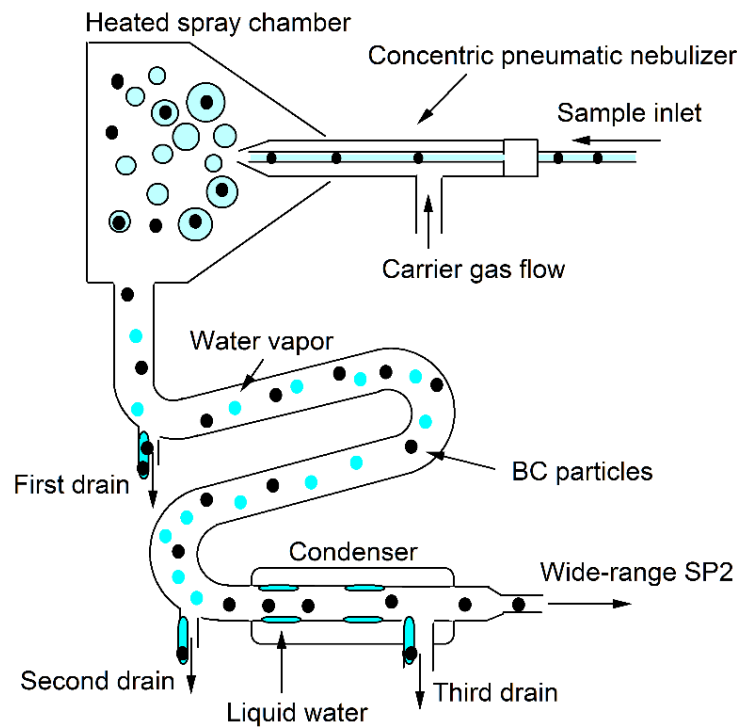


Figure 2.3. Schematic diagram of the Marin-5 pneumatic nebulizer.

2.1.2.2 Single-Particle Soot Photometer

2.1.2.2.1 Instrument Configuration

The SP2 is an instrument for measuring the size-resolved BC mass concentration by the laser-induced incandescence technique [Stephens et al., 2003; Moteki and Kondo, 2010]. A schematic diagram of a standard SP2 is shown in Figure 2.4 [Moteki and Kondo, 2010]. In the standard SP2, an air aerosol jet containing aerosol particles intersects an intra-cavity Nd:YAG laser beam ($\lambda = 1064$ nm). The laser is in a TEM₀₀ mode with a Gaussian intensity distribution. Two of the four detection channels are utilized for detecting incandescence in two different wavelength bands (a blue band at $\lambda = 300$ – 550 nm, and a red band at $\lambda = 580$ – 710 nm). Incandescence in the 300–550 nm band is detected by an H6779 photomultiplier tube (PMT; Hamamatsu Inc., Hamamatsu, Shizuoka, Japan) equipped with a KG5 band-pass filter (Schott Inc., Elmsford, NY, USA). Incandescence in the 580–710 nm band is detected by a H6779-02 PMT (Hamamatsu Inc.) equipped with a narrow band-pass filter (PB0640-140, Asahi Spectra Inc., Tokyo, Japan). The other detection channels are utilized for detecting scattered light at 1064 nm, which is detected by a Si-avalanche photodiode (APD; C30916E, Perkin–Elmer Inc., Waltham, MA, USA) and a position-sensitive Si-avalanche photodiode (PS-APD; C30927E-01, Perkin–Elmer Inc.). Each detection channel has high-gain and low-gain detectors and the sensitivity of the high-gain detectors is 10 times that of the low-gain detectors.

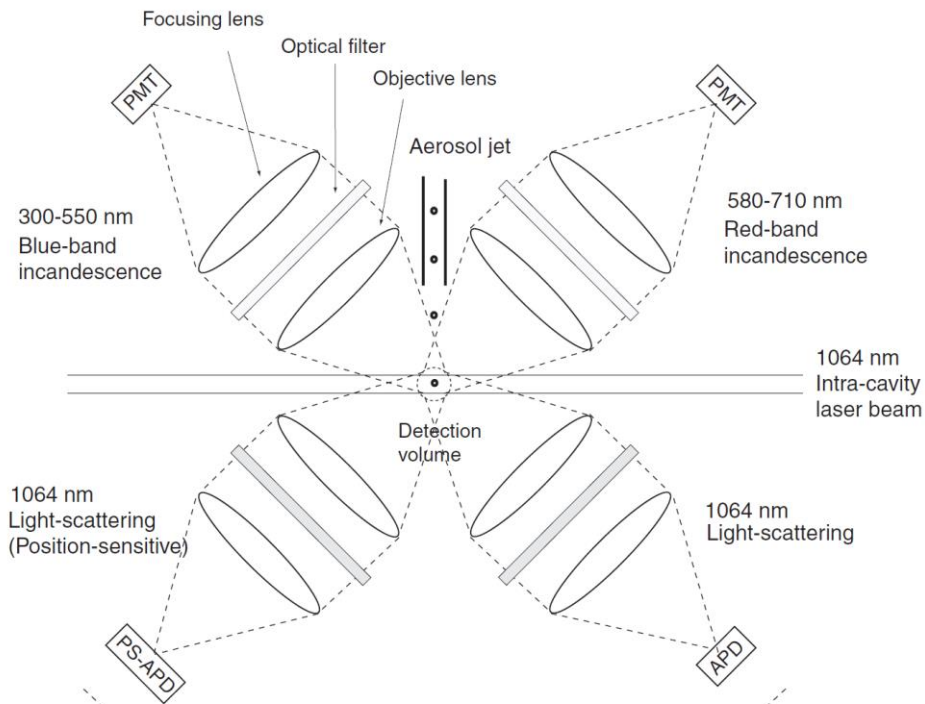


Figure 2.4. Schematic diagram of the single-particle soot photometer (SP2)

2.1.2.2.2 Selective Detection of Black Carbon Particles

Figure 2.5 schematically shows how BC-free (a non-absorbing) and BC-containing particles interact with the laser beam in the standard SP2. During transit of BC-free particles in the standard SP2 laser beam, a BC-free particle scatters the laser light and the scattering signal are detected by an APD (Figure 2.4). The standard SP2 is enabled to measure the optical diameter of the BC-free particles ($D_{\text{BC-free}}$) by using the relationship between the peak intensity of the scattering signal and the scattering cross section (C_s) of particles. The C_s is calculated by Mie theory, assuming the refractive index of spherical particles [Bohren and Huffman, 1983]. The detectable $D_{\text{BC-free}}$ ranged from 200 to 920 nm.

During transit of BC core particles in the standard SP2 laser beam, a BC core absorbs the energy and is heated to the vaporization temperature ($\sim 4000\text{K}$) to emit the incandescence radiation. The intensity of the incandescence light signal is detected by a H6779 PMT to measure the individual D_{BC} by using the relationship between the peak intensity and the individual BC mass, assuming a true density of BC particles of 1.8 g cm^{-3} [Moteki and Kondo, 2010]. These detail calibration is described in section 2.1.2.3.1. The detectable D_{BC} ranged from 70 to 920 nm in the standard SP2.

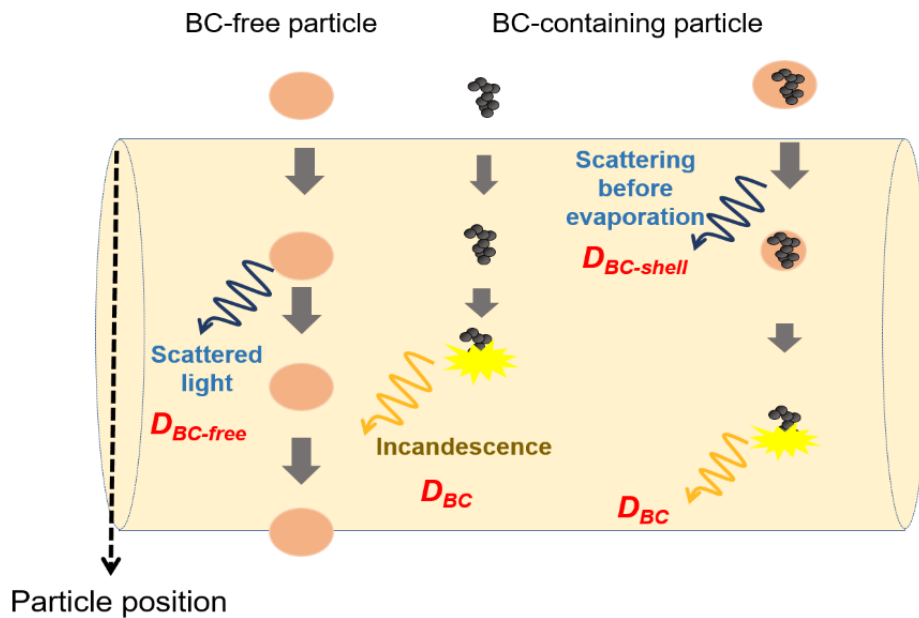


Figure 2.5. Schematic diagram of transit of aerosol particles introduced into the SP2 laser beam.

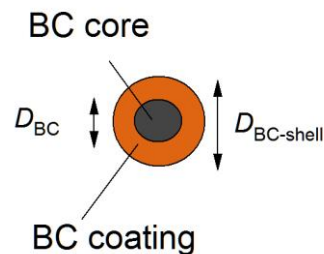


Figure 2.6. Schematic diagram of shell-core model

In addition, the standard SP2 measures the amount of coating on a BC-core particle. For quantitative explanation of the mixing state of BC-containing particles, a shell-core model is used in Figure 2.6. The dry shell/core ratio (SCr) is defined as follow:

$$\text{SCr} = D_{\text{BC-shell}} / D_{\text{BC}}, \quad (2.1)$$

where $D_{\text{BC-shell}}$ is the whole optical diameter of BC-containing particle. The $D_{\text{BC-shell}}$ is derived from the measurement of differential scattering cross section of particle integrated over the solid angle of light collection (ΔC_s) before the coating on a BC core starts to evaporate [Gao et al., 2007; Moteki and Kondo, 2008; Labored et al., 2012].

During transit of BC-containing particles in the standard SP2 laser beam, a BC-containing particle first emits the unperturbed scattering signal at the edge of laser beam. Thereafter, due to the heating of BC core, the coating on a BC core gradually evaporates until the particle enters the center of the laser beam. Thus, the measured scattering signal is non-Gaussian and is smaller than the reconstructed Gaussian scattering function of the unperturbed particle. To reconstruct the scattering amplitude of full Gaussian function, Gao et al. [2007] suggested the leading-edge method which fits the unperturbed scattering signal at the edge of laser beam (i.e. at the position of $\Delta C_s = 0$) to a Gaussian. This leading-edge method enables the measurement of individual $D_{\text{BC-shell}}$ by using the relationship between the reconstructed peak intensity and the C_s of BC-containing particles. The C_s of BC-containing particles is calculated by Mie theory, assuming the refractive indices of BC core and BC coating.

2.1.2.3 Wide-Range SP2

To expand the upper limit of the D_{BC} detectable by the standard SP2, the PS-APD was replaced with the H6779 PMT equipped with the KG5 filter and then the sensitivity of the PMT was lowered by a factor of about 140. Thus, WR-SP2 had three incandescence detection channels and one scattering detection channel. As a result, the detection limit was extended from 920 nm to 4170 nm, assuming a true density of BC particles of 1.8 g cm^{-3} [Moteki and Kondo, 2010].

2.1.2.3.1 Calibration of BC

The relationship between the peak intensity of the incandescent light and the individual BC mass is also crucial to quantify the individual D_{BC} . Fullerene soot samples (FS; Alpha Aeser Inc., Wardhill, MA, USA) are used for the calibration as standard BC samples [Moteki et al., 2010]. The experiment setup is shown in Figure 2.7. The laboratory BC samples were aerosolized from a water suspension by an atomizer and dried by a diffusion dryer with a silica gel. Thereafter, the individual BC masses were selected by an aerosol particle mass analyzer (APM model 3601, [Ehara et al., 1996; Tajima et al., 2011]) with a neutralizer and then introduced to the standard SP2. Due to the calibration, the relationship between the selected BC mass and measured incandescence signal is determined.

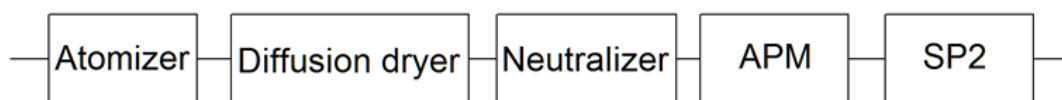


Figure 2.7. Experiment setup for measuring the relationship between the peak intensity of incandescence and the individual BC mass

Figure 2.8a shows the relationship between the peak incandescence signal (S) and the BC particle mass (M_{BC}) up to 30.0 fg ($D_{BC} = 317$ nm) for FS samples. The data for masses smaller than 10.0 fg ($D_{BC} = 220$ nm) was linearly fitted to derive the equation (2.2):

$$S = 2.2 \times 10^3 \times M_{BC} \quad (M_{BC} < 10.0 \text{ fg}). \quad (2.2)$$

The relationship was extrapolated to diameters up to 4170 nm, in the form of $S = a(M_{BC})^b$. The values of a and b were determined by least-squares fitting of the experimental data with $M_{BC} < 30.0$ fg:

$$S = 2.7 \times 10^3 \times (M_{BC})^{0.925} \quad (10.0 \text{ fg} \leq M_{BC}). \quad (2.3)$$

The value of b derived in this study is similar to that derived in our previous study [Moteki and Kondo, 2010].

For masses larger than 10.0 fg ($D_{BC} = 220$ nm), the calibration curve depends on the shapes of the BC particles, as demonstrated by Moteki and Kondo [2010], who also showed that the shapes can be represented by their effective densities (ρ_{eff}). Here, BC particles with ρ_{eff} of about 0.30 are called as non-compact (highly-branched aggregates), and those with ρ_{eff} of about 2.0 are called as compact (spherical). To estimate the uncertainties arising from the different shapes of the BC particles, the calibration curves were determined for BC particles with extremely non-compact ($b = 1.0$; equation (2.4)) and compact ($b = 0.667$; equation (2.5)) shapes for masses larger than 10.0 fg ($D_{BC} = 220$ nm) (Figure 2.8a):

$$S_{\text{non-compact}} = 2.2 \times 10^3 \times (M_{\text{BC}})^{1.0} \quad (10.0 \text{ fg} \leq M_{\text{BC}}) \quad (2.4)$$

$$S_{\text{compact}} = 4.8 \times 10^3 \times (M_{\text{BC}})^{0.667} \quad (10.0 \text{ fg} \leq M_{\text{BC}}) . \quad (2.5)$$

$S_{\text{non-compact}}$ and S_{compact} are the peak incandescence signals derived from the M_{BC} of particles with extremely non-compact and compact shapes, respectively. For BC particles with extremely non-compact and compact shapes, the parameter b approaches 1.0 and 2/3 (= 0.667), respectively, because each volume element and the surface area of the BC particles interact with the incident radiation [Moteki and Kondo, 2010]. Parameter a in equation (2.5) was determined so that the $S_{\text{non-compact}}$ value would equal the S_{compact} value at $M_{\text{BC}} = 10.0$ fg. As an example, Figure 2.8b shows the dependence of the mass size distributions of BC particles derived from the SP2 data for ambient air in Tokyo on the calibration curves (Figure 2.8a). The derived size distribution strongly depends on b in the extrapolated BC size range. Adachi et al [2010] showed that most BC particles were not completely compacted in high pollution area by using Transmission electron microscopy (TEM). Therefore, this study assumed that there were very few BC particles with extremely compact shapes in the air and rainwater.

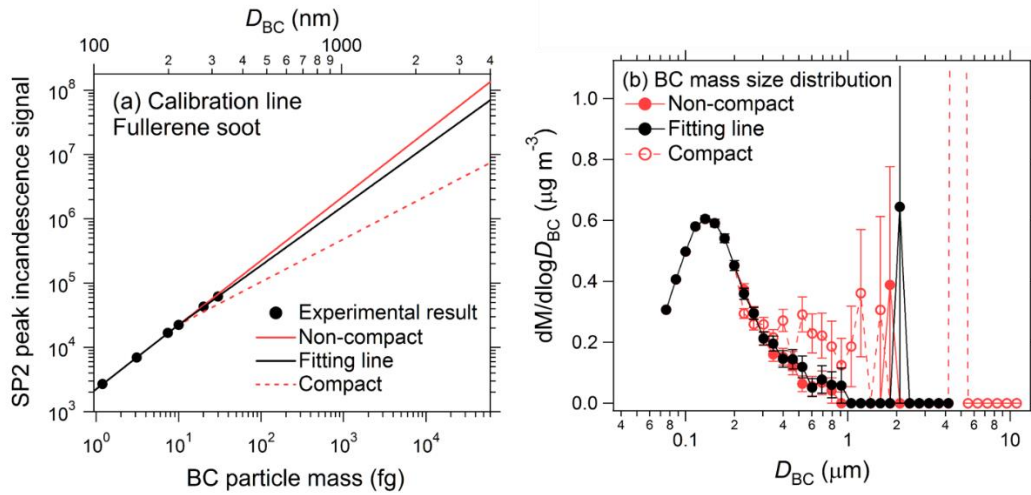


Figure 2.8. (a) Calibration curves of the WR-SP2 for fullerene soot and for extremely non-compact and compact shapes of BC particles. (b) Mass size distributions of BC particles in Tokyo air, determined by using the three different calibration curves. For the size distribution of BC particles with extremely compact shapes, the $dM/d\log D_{BC}$ value for $D_{BC} = 4780$ nm ($8.74 \mu\text{g m}^{-3}$) is not shown. Bars indicate 1σ of a Poisson distribution.

2.1.2.3.2 Overall Performance of the WR-SP2

To evaluate the overall performance of the WR-SP2, the simultaneous measurements of number and mass size distributions of BC in ambient Tokyo air by the standard SP2 and the WR-SP2 were conducted (Figure 2.9). Figure 2.9a also showed the ratios of the number concentrations of BC particles measured by the WR-SP2 to those measured by the standard SP2 for $D_{BC} < 300$ nm. For $D_{BC} > 300$ nm, the ratios are not shown, because BC particle counts were too low to be statistically meaningful. The number size distributions agreed to within 20% in the $70 < D_{BC} < 300$ nm range. The total BC mass and number concentrations in the $70 < D_{BC} < 920$ nm range agreed to within 5.3% and 1.4%, respectively.

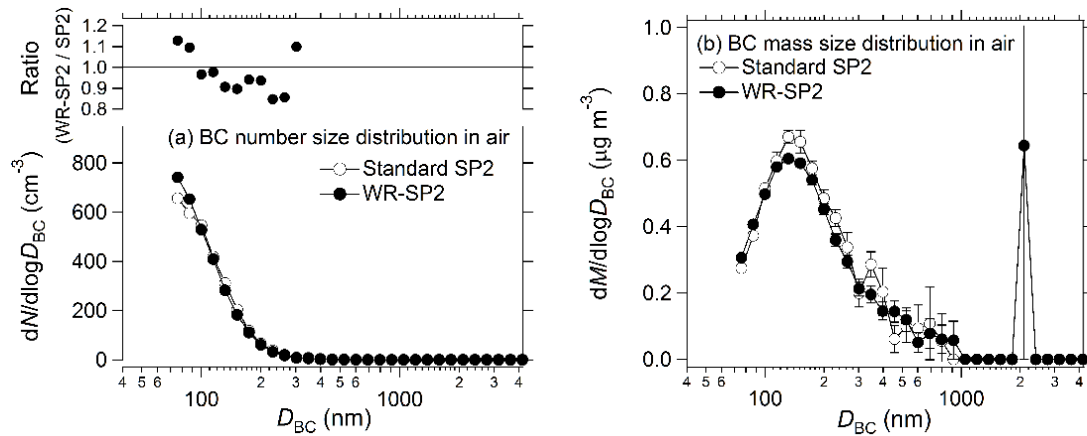


Figure 2.9. (a) Mean number size distributions of BC in Tokyo air measured by the standard SP2 and the WR-SP2 (bottom). The ratio of the number concentration measured by the WR-SP2 to that measured by the standard SP2 at different sizes is also shown (top). (b) Mean mass size distributions of BC in Tokyo air measured by the standard SP2 and the WR-SP2. Bars indicate 1σ of a Poisson distribution.

2.1.3 Methods: Extraction Efficiency of Marin-5

To make an accurate measurement of the number and mass size distributions of BC in rainwater, it is essential to determine how much BC particles are extracted from the water sample and transported to the WR-SP2; extraction efficiency (ϵ). In this section, first, the theoretically-calculated extraction efficiency (ϵ_{cal}) was described. Then, the extraction efficiency (ϵ_{exp}) was determined at the laboratory experiment, using the polystyrene latex (PSL) suspensions and BC standard samples. Finally, the ϵ_{exp} values were compared with the ϵ_{cal} values.

2.1.3.1 Theoretically-Estimated Extraction Efficiency

Some number fraction of BC particles in water samples is lost together with generated droplets during nebulization or lost by deposition on several walls during transport in the Marin-5/WR-SP2 sampling line. Therefore, the ε_{cal} was represented as the product of volume fraction of particles aerosolized by nebulization (F_{aerosol}) in the heated chamber and transport efficiency ($\eta_{\text{transport}}$) of aerosolized particles in the Marin-5/WR-SP2 sampling line after nebulization in equation (2.6);

$$\varepsilon_{\text{cal}}(D) = F_{\text{aerosol}} \times \eta_{\text{transport}}(D). \quad (2.6)$$

The size-resolved $\eta_{\text{transport}}(D)$ is derived from the number fraction of particles not lost by the deposition mechanism during the transit of that flow element ($\eta_{\text{flow element, mechanism}}$). In this calculation, four-distinct deposition mechanisms (gravitational setting, diffusional deposition, inertial deposition at a bend, and inertial deposition at flow constrictions) were considered under the condition of laminar flow in the sampling line. Equation (2.7) represents $\eta_{\text{transport}}(D)$, which is the product of the transport efficiencies for each mechanism in each flow element of the sampling transport system for that particle size [Baron and Willeke, 2001].

$$\eta_{\text{transport}}(D) = \prod_{\text{flow elements}} \prod_{\text{mechanisms}} \eta_{\text{flow element, mechanism}}(D). \quad (2.7)$$

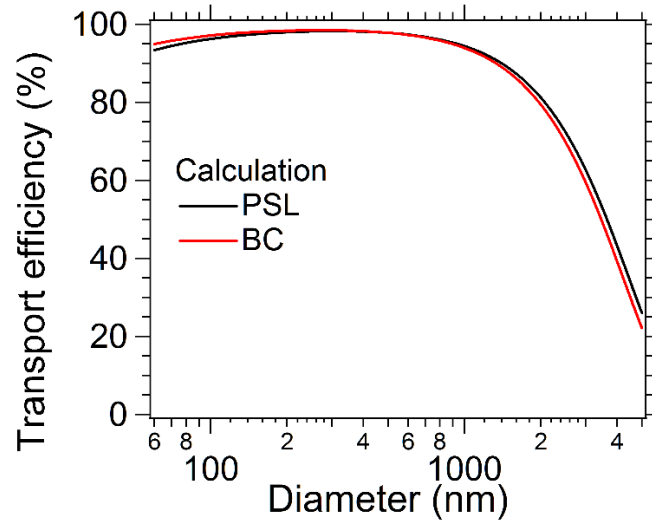
In this study, the Marin5/WR-SP2 sampling line was divided into 23 elements to calculate the size-resolved $\eta_{\text{flow element, mechanism}}$, considering the density and shape of particles. For spherical particles (PSL particles) and non-spherical particles (BC particles),

$\eta_{\text{transport}}(D)$ were calculated. The true density of BC (ρ_{BC}) and PSL (ρ_{PSL}) was assumed to be 1.8 (g/cc) and 1.05 (g/cc), respectively [Moteki and Kondo 2010]. The particle shape is represented by effective density (ρ_{eff}) for each particle (ρ_{eff} for BC = 0.5, ρ_{eff} for PSL = 1.0) [Moteki and Kondo 2010].

The theoretically-estimated $\eta_{\text{transport}}$ of aerosolized PSL and BC particles were shown in Figure 2.10a. The size-dependent $\eta_{\text{transport}}$ of PSL was found to be identical to that of BC, indicating that $\eta_{\text{transport}}$ was largely independent of BC shape. The $\eta_{\text{transport}}$ for $D_{\text{BC}} < 1000$ nm was changed little, while the $\eta_{\text{transport}}$ for $D_{\text{BC}} > 2000$ nm largely decreased. To understand the deposition mechanism for particles with $D_{\text{BC}} > 2000$ nm, the size-resolved $\eta_{\text{transport}}$ for each deposition mechanism was calculated. Figure 2.10b shows the relative contribution of four deposition mechanisms for PSL particles. The result indicated that the main deposition mechanisms for particles with $D > 2000$ nm were gravitational setting and inertial deposition in flow constriction. The size-resolved $\eta_{\text{transport}}$ for each deposited place was also calculated. The particles with $D > 2000$ nm were mainly deposited on the wall of the Marin-5, inside 1/4 tube transported from Marin-5 to SP2, and inside the SP2 sampling line.

Next, the F_{aerosol} was experimentally determined by using the ammonium sulfate solutions with known mass concentrations. The detail experiment is described in section 2.1.5. The experiment results showed that the F_{aerosol} was about 0.5. Using the equation (2.6), the ε_{cal} for PSL and BC particles were calculated in Figure 2.11(b).

(a)



(b)

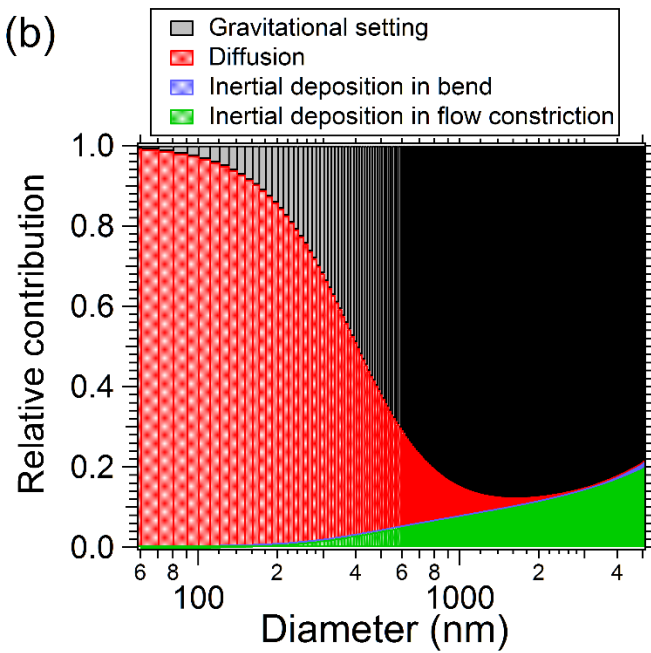


Figure 2.10 (a) Theoretically-estimated transport efficiency in the Marin-5/WR-SP2 sampling line for aerosolized polystyrene latex (PSL) and BC particles. (b) Relative contribution of four deposition mechanisms of PSL particles.

2.1.3.2 Extraction Efficiency

2.1.3.2.1 Number Concentration of Polystyrene Latex Spheres in Water

To experimentally determine the extraction efficiency of the Marin-5 nebulizer, PSL suspensions of known number concentration were prepared. The mean diameters of the PSL spheres (D_{PSL}) were 202 ± 5.0 , 254 ± 8.0 , 309 ± 9.0 , 402 ± 6.0 , 603 ± 14 , and 814 ± 19 nm (JSR Inc., Kamitu, Ibaraki, Japan); 1025 ± 30 and 1537 ± 77 nm (Polyscience Inc., Warrington, PA, USA); and 2.0 ± 0.02 , 3.0 ± 0.03 , 4.0 ± 0.03 , and 5.0 ± 0.04 μm (Duke Scientific Corp., Palo Alto, CA, USA). The size-resolved number concentrations of the PSL suspensions ($N(D_{\text{PSL}})$) were determined by measuring the attenuation of a solid-state 532 nm laser (GSHG-3020F; KTG Co. Ltd., Kochi, Japan) [Ohata et al., 2013]. The values of $N(D_{\text{PSL}})$ ranged from 7.04×10^4 to 2.53×10^9 particles cm^{-3} . The PSL suspensions were diluted further to determine the extraction efficiency of the Marin-5 nebulizer.

2.1.3.2.2 Extraction Efficiency with PSL Spheres and AquaBlack 162

The ε_{exp} of the Marin-5 were experimentally determined by measuring the number concentrations of PSL suspensions with the 12 diameters. Here, the ε_{exp} values of PSL and BC were assumed to be identical [Ohata et al., 2013]. Figure 2.11a shows the ε_{exp} values in the $200 < D_{\text{BC}} < 5000$ nm range. The ε_{exp} values of the U5000AT in the $100 < D_{\text{BC}} < 1025$ nm range [Ohata et al., 2013] are also plotted for comparison. The ε_{exp} values of the Marin-5 were $50.0 \pm 4.4\%$ on average in the $200 < D_{\text{BC}} < 2000$ nm, and they linearly decreased at larger sizes, as fitted with linear equations (2.8) and (2.9):

$$\varepsilon_{\text{exp}}(200 \text{ nm} < D_{\text{PSL}} \leq 2000 \text{ nm}) = 50.0 (\%) \quad (2.8)$$

$$\varepsilon_{\text{exp}}(2000 \text{ nm} < D_{\text{PSL}} \leq 5000 \text{ nm}) = -0.017D_{\text{PSL}} + 82.2 (\%) \quad (2.9)$$

These values may depend on the liquid and air flow rates. The ε_{exp} values of the Marin-5 were much higher than those of the U5000AT. The size-independent and high ε_{exp} values greatly improved the measurement accuracy of the size distributions of BC in water in the $200 < D_{\text{BC}} < 2000$ nm range using a water sample of only a few milliliters. For $D_{\text{BC}} > 2000$ nm, the ε_{exp} values linearly decreased, owing to particle losses by impaction and gravitational setting on the walls of various parts of the system (Figure 2.10b).

To determine the ε_{exp} value of the Marin-5 for $D_{\text{BC}} < 200$ nm, a known mass concentration ($35 \mu\text{g L}^{-1}$) of AquaBlack 162 (AB-162; Tokai Carbon Co. Ltd., Tokyo, Japan) was prepared, which is a laboratory standard of BC particles suspended in water [Ohata et al. 2011, 2013]. The measured mass median diameter of the mass size distribution was 90 nm, and the geometric standard deviation was 1.33. The mass fraction of BC particles with $D_{\text{BC}} < 70$ nm undetectable by the SP2 was estimated to be 7.1%. The ε_{exp} value for AB-162 was estimated to be $42 \pm 7.9\%$, indicating that the estimated ε_{exp} value agreed to within 20% of the ε_{exp} value (50%) within the $200 < D_{\text{BC}} < 2000$ nm range determined with the PSL suspension (Figure 2.11a).

Figure 2.11(b) showed the comparison between the size dependence of ε_{exp} and that of ε_{cal} , indicating that ε_{exp} values were consistent with the ε_{cal} values within the systematic errors. Therefore, the equation (2.8) and (2.9) were used for calculating the size-resolved number concentrations of BC in rainwater.

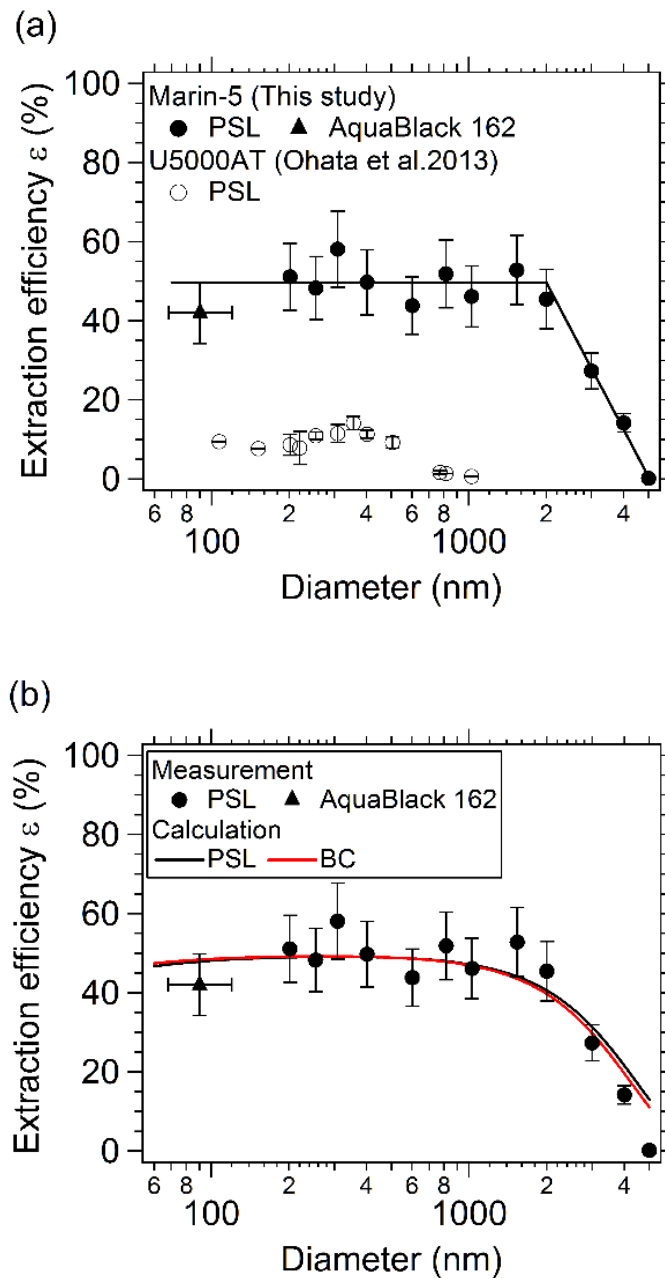


Figure 2.11(a) Extraction efficiency of the Marin-5, measured by using polystyrene latex (PSL) spheres and AquaBlack 162 in water. Error bars show the systematic errors. For comparison, the extraction efficiency of an ultrasonic nebulizer (U5000AT) is also shown [Ohata et al., 2013]. (b) Comparison between the measured and calculated extraction efficiency of the Marin-5.

2.1.4 Reproducibility

The reproducibility of the measured BC size distributions in two rainwater samples collected at Cape Hedo, Okinawa Island, Japan was assessed. The BC mass concentrations in these samples were 50 and 106 $\mu\text{g L}^{-1}$, respectively. The size distributions of BC in the two rainwater samples were measured on two different days, 22 days apart (Day 1 and Day 23). Figure 2.12 shows the number and mass size distributions of BC for one of the samples on Day 1 and Day 23, together with the Day 23:Day 1 ratios of the respective distributions up to 300 nm. For $D_{\text{BC}} > 300$ nm, the ratios are not shown, because the BC particle concentrations were very low. These BC number and mass size distributions agreed to within 12%. The count median diameter (CMD) and geometric standard deviation (σ_{gc}) of the number size distributions of the two samples were reproducible to within 1.0%. This result showed that the BC size distribution in liquid water changed little during about 3 weeks, consistent with the previous study [Ohata et al., 2013].

The overall uncertainty of the measurements of BC in water by the Marin-5/WR-SP2 system was estimated to be about 16%. This value comprises the uncertainties of ϵ ($\pm 4.4\%$), the size-resolved BC mass concentration in air measured by the WR-SP2 ($\pm 15\%$), F_{neb} ($\pm 5\%$), and V_{pump} ($\pm 5\%$). The deviation of the Day 23/Day 1 ratio from 1 is within this estimated uncertainty of the BC size distribution measurement.

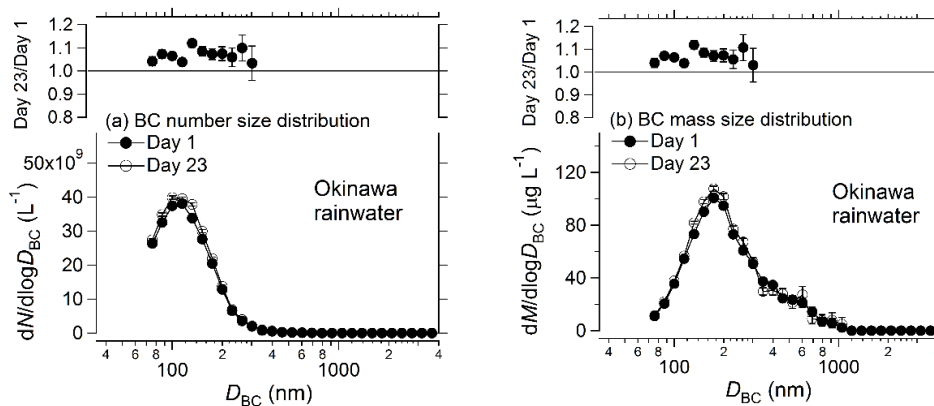


Figure 2.12. (a) Number and (b) mass size distributions of BC in Cape Hedo rainwater samples (bottom panels). The ratios of the number and mass concentrations of BC in rainwater on two different days are also shown (top). Bars indicate 1σ values.

2.1.5 Estimates of Aerosolized Volume Fraction in the Marin-5 and the Droplet Distribution

Ammonium sulfate (AS) solutions of known mass concentration were used to estimate the F_{aerosol} of the Marin-5. In addition, the size distribution of the droplets generated by the concentric pneumatic nebulizer was estimated. The data was used to estimate possible changes in the size of BC particles during the extraction process by the Marin-5 (section 2.1.3).

2.1.5.1 Aerosolized Volume Fraction in the Marin-5

To estimate the F_{aerosol} of the Marin-5 and the droplet size distribution, AS solutions of six different mass concentrations were first prepared (Table 2.1). These AS solutions were fed to the Marin-5 by a peristaltic pump to generate droplets of AS solution, and then the AS particles were extracted (Figure 2.13).

The generated AS particles were further dried to a relative humidity (RH) of about 12% by passing them through a Nafion tube to minimize the effect of hygroscopic growth of the particles. The dried AS number size distributions (15–900 nm) were measured with an accuracy of about 10% by a scanning mobility particle sizer spectrometer (SMPS 3936; TSI Inc., Shoreview, MN, USA) consisting of a differential mobility analyzer (Model 3081, TSI Inc.) and a condensation particle counter (Model 3010, TSI Inc.). The contribution of non-AS particles to the total volume of the extracted particles was negligibly small.

The F_{aerosol} was determined as the ratio of the volume of AS particles extracted per second ($V_{\text{air}}(\text{cm}^3)$) to the volume of AS in the solution supplied per second ($V_{\text{sol}}(\text{cm}^3)$). Figure 2.14 shows the correlation between V_{air} and V_{sol} . The F_{aerosol} value, derived as the slope of the correlation line, was $48 \pm 6.3\%$ (1σ) within the range of 15–900 nm, which is used to calculate the ε_{cal} .

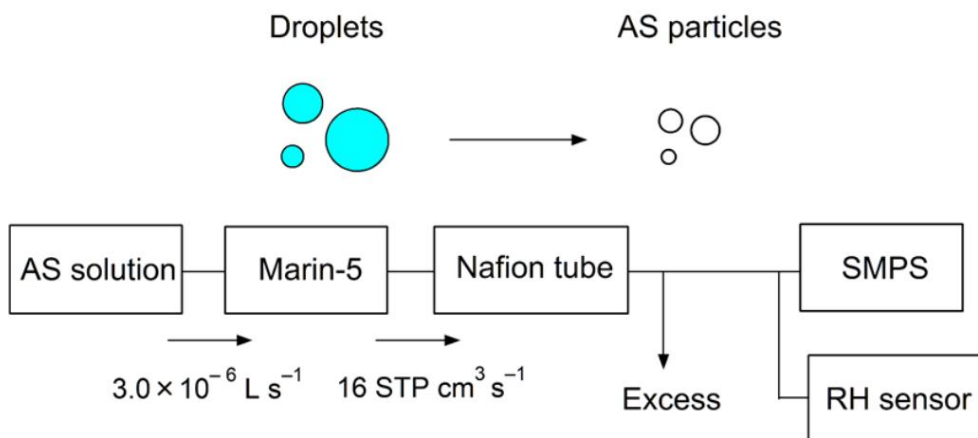


Figure 2.13. Experimental setup for estimating the extraction efficiency of the pneumatic nebulizer (Marin-5) and the size distribution of the generated droplets of ammonium sulfate (AS) solution. SMPS, scanning mobility particle sizer spectrometer; RH, relative humidity.

Table 2.1. Mass concentrations of ammonium sulfate (AS) solutions used to estimate the extraction efficiency of the Marin-5 nebulizer and corresponding count median diameter (CMD) and geometric standard deviation (σ_{gc}) values of the AS particles and droplets generated by the nebulizer.

Solution	Mass concentration of AS in water (mg L^{-1})	AS CMD (nm)	Estimated droplet CMD (μm)	AS and estimated droplet σ_{gc}
1	1.34	30	3.3	1.78
2	2.69	34	2.9	1.82
3	2.73	35	3.0	1.76
4	5.38	41	2.8	1.84
5	13.4	49	2.5	1.84
6	26.9	58	2.3	1.86

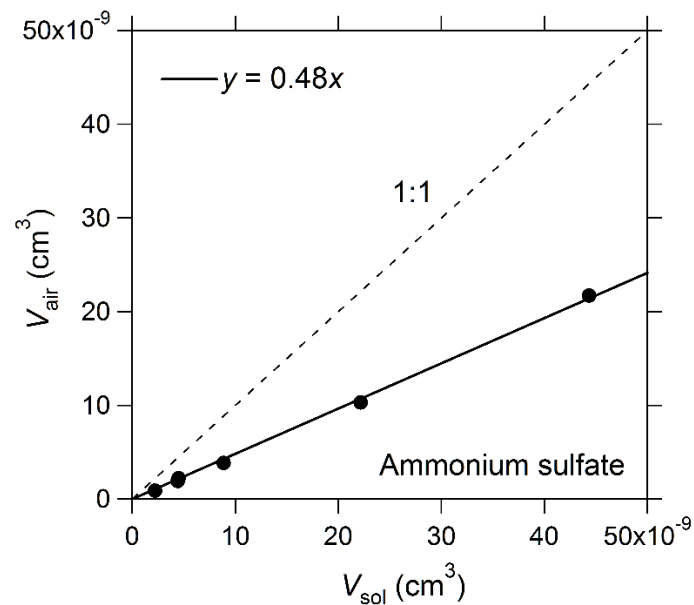


Figure 2.14. Correlation between the volume of ammonium sulfate (AS) particles extracted by the Marin-5 per second (V_{air}) and the volume of AS solution fed to the concentric pneumatic nebulizer per second (V_{sol}). The solid line is the least-squares fitted line.

2.1.5.2 Droplet Size Distribution

The size distribution of droplets generated from the nebulizer was also estimated, so that possible changes in the size of BC particles occurring during evaporation of droplets could be estimated (section 2.1.6). The known mass concentration of AS in solution (X) is expressed as the ratio of the mass of solute (AS) to that of the solution (deionized water + AS):

$$X = \frac{\frac{\pi}{6}\rho_a D_a^3}{\frac{\pi}{6}\rho_d D_d^3} \quad (2.10)$$

D_a and D_d are the diameters of AS particles and droplets, respectively, and ρ_a and ρ_d are the densities of the AS particles (1.77 g cm^{-3}) and droplets, respectively. ρ_d is approximately regarded as water density ($\rho_1: 1.00 \text{ g cm}^{-3}$), because the mass mixing ratios of AS were less than 30 parts per million (ppm). Therefore, using ρ_1 , D_d is derived by equation (2.11):

$$D_d = D_a \times \sqrt[3]{\frac{\rho_a}{\rho_1} \times \frac{1}{X}} \quad (2.11)$$

Figure 2.15 shows the measured size distribution of AS particles generated using solution 4 (Table 2.1). The AS mass concentration of 5.38 mg L^{-1} is similar to the typical value for rainwater in East Asia [Fujita et al., 2000]. Figure 2.15 also shows the droplet size distribution estimated from the AS size distribution (equation (2.11)). The CMD and σ_{gc} values of the AS and droplet number size distributions of each sample are summarized in Table 2.1. The average CMD of the droplet number size distribution was $2.8 \pm 0.4 \text{ }\mu\text{m}$,

and the average σ_{gc} was 1.82 ± 0.04 .

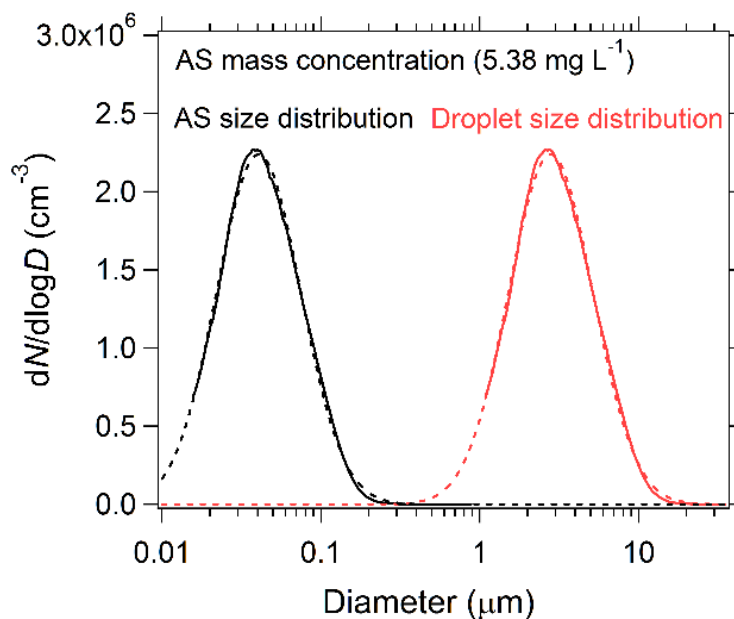


Figure 2.15. Size distribution of ammonium sulfate (AS) particles for an AS mass concentration of 5.38 mg L^{-1} . The droplet size distribution estimated from the AS size distribution is also shown. The dashed lines show the lognormal fitted size distributions.

2.1.6 Changes in BC Size in the Nebulizer

2.1.6.1 Experimental Evaluation

BC particle size can change because of coagulation of BC particles during the extraction process. First, to evaluate this effect by laboratory experiments, two kinds of BC samples with known mass concentrations were prepared: AB-162 and FS. The mass median diameter and average geometric standard deviation of FS were 174 nm and 1.54, respectively. The number concentrations of AB-162 particles were about 10 times higher than those of FS particles with the same mass concentrations because of the smaller diameters of AB-162.

The mass concentrations of BC particles in the AB-162 and FS samples were 70 and 137 $\mu\text{g L}^{-1}$, respectively. The samples were diluted with deionized water and prepared six different BC mass concentrations in water. The ranges of the mass concentrations of BC in the AB-162 and FS samples were 7.3–70 and 6.9–137 $\mu\text{g L}^{-1}$, respectively. These BC mass concentrations are typical for rainwater collected in Tokyo and at Cape Hedo [Ohata et al., 2011; Mori et al., 2014].

The number size distributions of BC particles in the AB-162 and FS samples with the Marin-5/WR-SP2 system were measured. The measured number concentrations of BC particles in the AB-162 and FS samples ranged from 20×10^9 to 166×10^9 particles L^{-1} and from 1.2×10^9 to 19×10^9 particles L^{-1} , respectively, indicating that the number concentrations of BC particles in the AB-162 samples were about 10 times those in the FS samples. Figure 2.16 shows the normalized number size distributions of BC particles in the AB-162 and FS samples for different BC mass concentrations. This figure shows only the data for BC concentrations sufficiently high for reliable statistical analysis. To evaluate the effect of coagulation of BC particles during the extraction process, AB-162 and FS samples with BC mass concentrations of 8.0 and 18 $\mu\text{g L}^{-1}$ were used as reference samples. Figure 2.16 also shows ratios of the normalized number concentrations of BC particles in the AB-162 and FS samples (dN_{samp}) to those of the references (dN_{ref}) at different sizes. The AB-162 and FS ratios were normalized by $D_{\text{BC}}=76$ nm and $D_{\text{BC}}=115$ nm, respectively. These results show that the effect of coagulation of BC particles during the extraction process was negligibly small for BC mass concentrations of less than about 70 $\mu\text{g L}^{-1}$ for the FS samples and less than about 30 $\mu\text{g L}^{-1}$ for the AB-162 samples.

The BC number size distributions shifted to larger sizes for BC mass

concentrations substantially higher than these threshold mass concentrations (Figure 2.16b and d). The shift is attributed to the coagulation of BC particles during the extraction process. The threshold mass concentration of AB-162 was lower than that of FS, reflecting the higher number concentration for a given mass concentration, as discussed above.

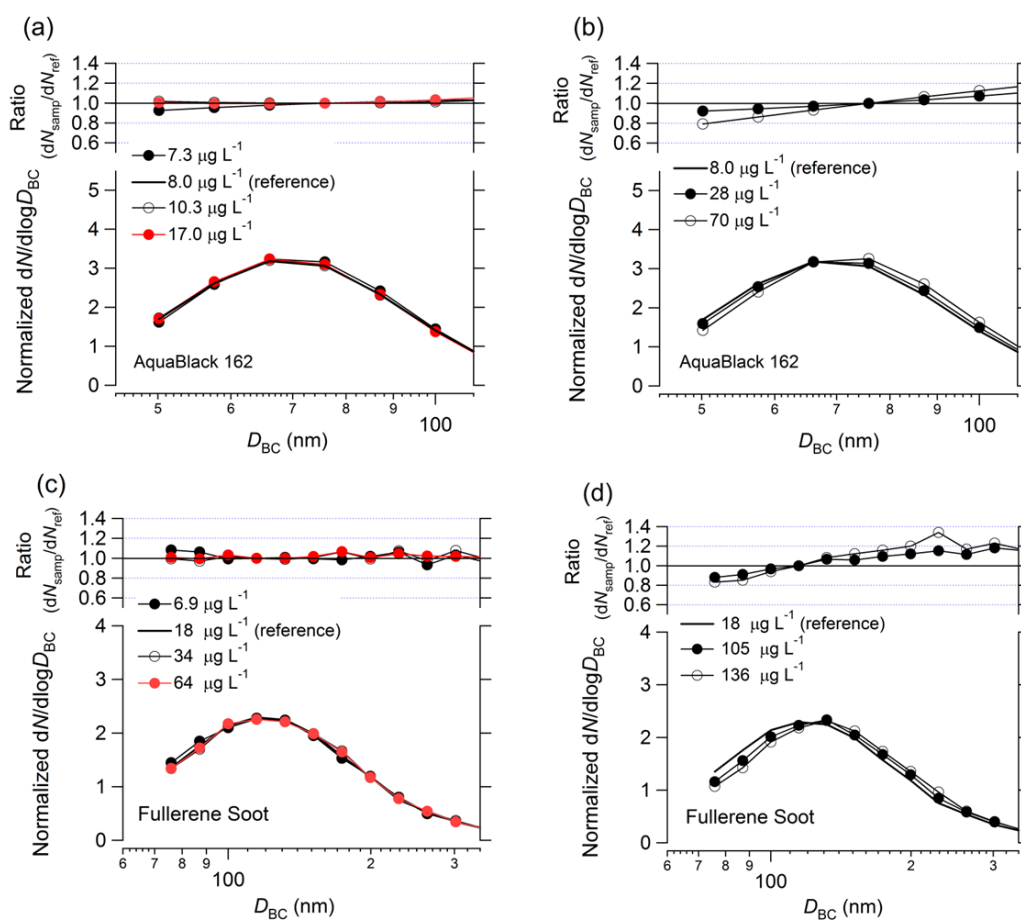


Figure 2.16. (a, b) Normalized number size distributions of BC particles in AquaBlack 162 (AB-162) samples. (c, d) Same as (a) and (b) but for fullerene soot (FS) samples. Ratios of normalized number concentrations of BC particles in AB-162 and FS samples to reference concentrations at different sizes are also shown, which were normalized by 76 and 115 nm for AB-162 and FS, respectively. The mass concentrations of the reference samples of AB-162 and FS were 8.0 and 18 $\mu\text{g L}^{-1}$.

2.1.6.2 Theoretical Evaluation

The effect of coagulation of BC particles during the extraction process was theoretically calculated and the result was compared with the experimental results. By using the theoretical model developed by Moteki and Mori [2015], the number size distribution of BC particles extracted by the nebulizer can be predicted from the droplet number size distribution and the BC number size distribution in the water sample. The calculated probability of the number of BC particles in an individual droplet is a measure of the effect of coagulation of BC particles. This probability is described by a Poisson distribution because the number of BC particles and droplets produced by a nebulizer is a discrete random variable. More details of the model are given by Moteki and Mori [2015].

The effect of coagulation is represented by the change of the calculated size distribution relative to the BC mass concentration in water. The calculated CMD of the extracted FS size distribution changed from 118 to 120 nm when the mass concentration in water changed from 6.9 to 64 $\mu\text{g L}^{-1}$. The predicted change in the standard deviation was about 1%. Similar changes in these parameters were predicted for AB-162. These small changes in the predicted size distributions provide a mathematical basis for the interpretation of the results of the laboratory experiments.

2.1.7 Changes in BC Particle Size in Cloud Droplets

The BC particle size might change during the condensation, coalescence, and precipitation processes shown in Figure 2.1. To investigate possible changes of the BC size distribution through these processes, an experiment that included all of these processes was carried out, although the conditions were different from those in the natural

atmosphere. In this experiment, the size distributions of BC particles in ambient Tokyo air by the standard SP2 were measured to compare them with those of BC particles collected in water by a particle-into-liquid sampler (PILS) (Figure 2.17). The PILS consists of a particle growth chamber and an impactor component [Weber et al. 2001; Orsini et al. 2003; Miyazaki et al. 2006]. Orsini et al. [2003] showed that almost all olive oil particles in the diameter range 0.03–6.0 μm were captured in the growth chamber under a high supersaturation of water vapor.

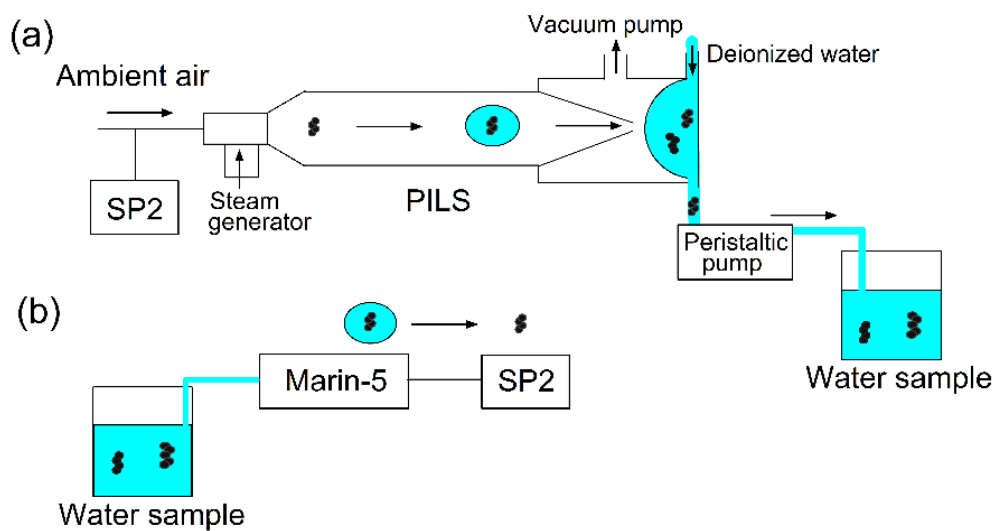


Figure 2.17. Experimental setup for measuring changes in the size distribution of BC particles during their collection by a particle-into-liquid sampler (PILS).

Table 2.2 Mass concentration, count median diameter (CMD) and geometric standard deviation (σ_{gc}) values of BC particles in Tokyo ambient air and the collected water samples on the first and second days.

	Ambient air			Collected water samples		
	Average BC mass concentration ($\mu\text{g m}^{-3}$)	CMD (nm)	σ_{gc}	BC mass concentration ($\mu\text{g L}^{-1}$)	CMD (nm)	σ_{gc}
First day	0.21 ± 0.04	113	1.59	0.76	121	1.49
Second day	0.55 ± 0.02	118	1.52	2.27	124	1.45

In this particle growth chamber, ambient particles containing BC are mixed with supersaturated water vapor to produce droplets through condensational growth. The droplets formed are collected by a polycarbonate impaction plate. The collected liquid sample is continually transported with a stream of ultrapure deionized water to a glass bottle by a peristaltic pump (IPC/IPC-N; ISMATEC, Wertheim, Germany) at a constant flow rate of $3.0 \times 10^{-6} \text{ L s}^{-1}$ (Figure 2.17a). The air sample flow rate for the PILS was maintained at $266 \text{ cm}^3 \text{ s}^{-1}$. The water sample was transferred to the Marin-5 and converted into aerosols (Figure 2.17b), and the BC particle size distributions were measured by the standard SP2.

Measurements were made on 25 December 2014 and 26 January 2015, and BC particles were collected for half an hour; Table 2.2 summarizes relevant values for the BC particles in air and the collected water samples. Average mass concentrations of BC in air on the first and second days were 0.21 ± 0.04 and $0.55 \pm 0.02 \mu\text{g m}^{-3}$, respectively. Mass

concentrations of BC in the collected water samples on the first and second days were 0.76 and 2.27 $\mu\text{g L}^{-1}$, respectively. The effect of coagulation of BC particles during the extraction process was negligibly small (section 2.1.6). Figure 2.18 shows the normalized number size distributions of BC in air and the collected water samples for the $100 < D_{\text{BC}} < 400$ nm range on the second day. This figure also shows the ratios of the normalized number concentration of BC in the collected water sample (N_{PILS}) to that in air (N_{air}) for the same D_{BC} range. The average $N_{\text{PILS}}/N_{\text{air}}$ ratio was 0.95 ± 0.09 (1σ), and the CMD and σ_{gc} values for air and the collected water sample agreed within 5.1% and 4.7%, respectively. The ratio was 1.0 ± 0.2 (1σ) for the $100 < D_{\text{BC}} < 350$ nm range. The large errors of the ratios (Figure 2.18) were caused by low BC particle counts. For lower BC mass concentrations on the first day, the average $N_{\text{PILS}}/N_{\text{air}}$ ratio was very similar (0.94 ± 0.18 (1σ)). The CMD value for air and the collected water sample agreed within 7.1%, and the σ_{gc} value for air and the collected water sample also agreed within 6.3%, respectively.

In this experiment, all ambient BC particles detectable by the SP2 should be captured in the particle growth chamber under high supersaturation, considering the results of Orsini et al. [2003]. The experimental results showed that the size distribution of BC particles activated as CCN was the same as the size distribution of BC in water condensed from water vapor. More specifically, the result indicates that the sizes of BC particles do not change during condensational growth.

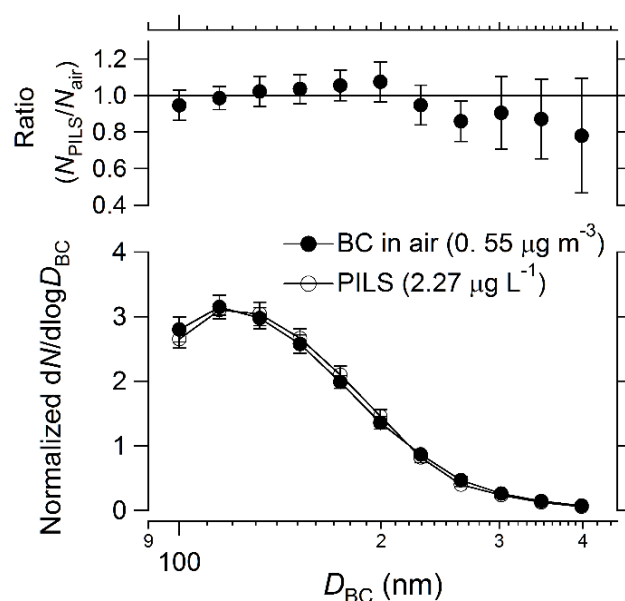


Figure 2.18. Normalized number size distributions of BC particles in ambient air and those collected by a particle-into-liquid sampler (PILS) in the $100 < D_{BC} < 400$ nm range (bottom). The ratio of the normalized number concentration in water (N_{PILS}) to that in air (N_{air}) at different sizes is also shown (top). Bars indicate 1σ values.

2.1.8 Size Distribution of BC Particles in Rainwater

The overall tests of the Marin-5/WR-SP2 system were conducted by measuring the size distributions of BC in air and rainwater simultaneously in Tokyo during summer of 2014. An automated rain sampling system was developed, which enabled the rain samples to be analyzed within about 3 min after the start of rainfall. First, the rainwater was collected with a plastic funnel (30 cm maximum diameter) and transferred to a glass bottle through a Tygon tube. Then, the rainwater was directly introduced into the Marin-5/WR-SP2 system by a peristaltic pump (Figure 2.2). To estimate the losses of BC particles due to adhesion to the plastic funnel and the Tygon tube, the size-resolved mass concentration

of BC in rain samples collected at Cape Hedo with and without transferring them through the plastic funnel and Tygon tube was compared. The BC mass losses during the transfer were less than 7%, with negligible changes in the shape of the size distribution. In addition, the effect of dry deposition of BC particles on the funnel was estimated. The BC mass concentration deposited on the funnel was measured by pouring deionized water into the funnel. The effect of dry deposition of BC particles on the funnel was estimated to be negligibly small for measurement of BC in rainwater in Tokyo.

Figure 2.19 shows the normalized mass and number size distributions of BC in air 1 h before a precipitation event, which lasted for about 2 h, on 10 August 2014. Rainwater was collected about 50 min after the initiation of the precipitation. The average mass concentration of BC in air was $0.07 \pm 0.02 \mu\text{g m}^{-3}$, and the average mass concentration of BC in rainwater was $5.5 \pm 1.3 \mu\text{g L}^{-1}$. Figure 2.19b also shows the ratio of the normalized number concentration in rainwater (N_{rain}) to that in air (N_{air}) for different particle sizes. The ratios (i.e. wet removal efficiency $RE(D_{\text{BC}}) = N_{\text{rain}}(D_{\text{BC}})/N_{\text{air}}(D_{\text{BC}})$) are normalized to $D_{\text{BC}} = 130 \text{ nm}$. The size of BC in rainwater was larger than that in air, indicating that large BC particles were more efficiently removed by precipitation. The difference between the size distribution in air and that in rainwater was much larger than that caused through processes I–IV (Figure 2.1). Because of the thin coating thickness of BC particles in Tokyo air [Kondo et al., 2011b], larger BC particles are possibly more active as CCN. The detail understandings of scavenging mechanisms controlling the D_{BC} -dependence of $RE(D_{\text{BC}})$ are described in Chapter 3.

Figure 2.19 also show the existence of BC particles with $D_{\text{BC}} > 1 \mu\text{m}$, indicating that further studies of wet deposition of BC will require the use of the WR-SP2.

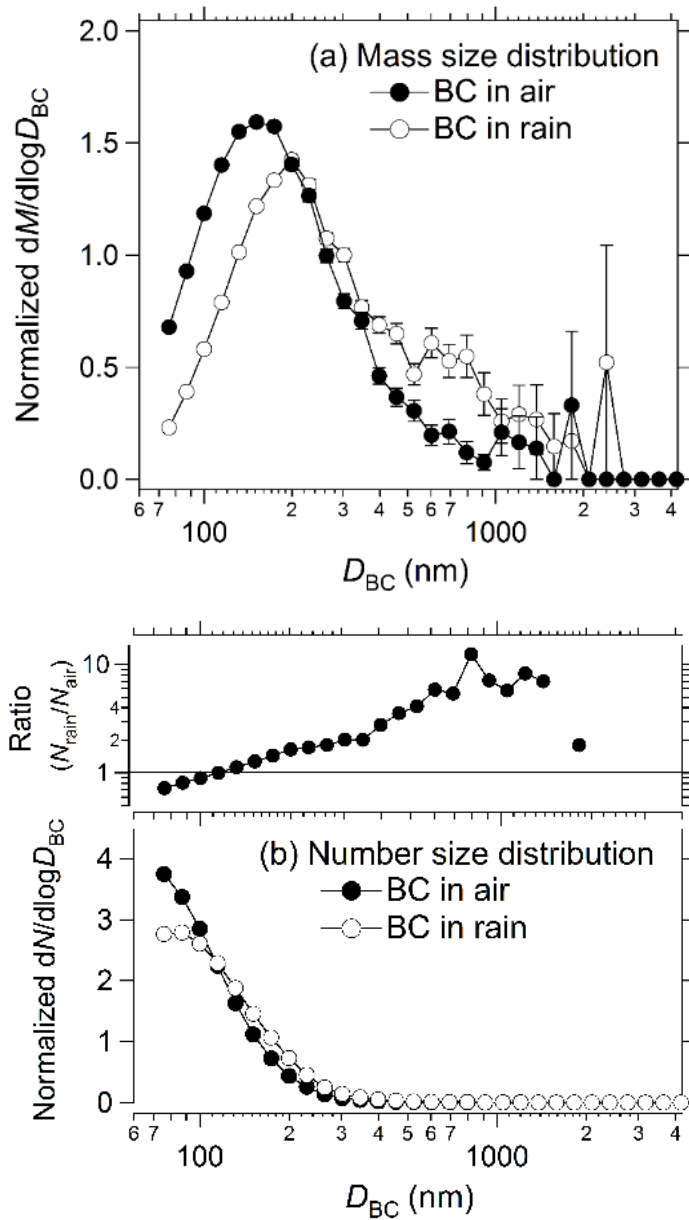


Figure 2.19. (a) Normalized mass size distributions of BC in air and rainwater collected in Tokyo on 10 August, 2014. (b) Same as (a) but for normalized number size distributions. Ratios of the normalized size distribution in rainwater to that in air are also shown. The ratios are normalized by $D_{BC} = 130$ nm. Bars indicate 1σ of a Poisson distribution

2.1.9 Experimental Setup for Observation

This section describes the experiment setup for measuring the wet removal efficiency of BC during BC-CARE field observation campaign in Tokyo and in Okinawa (Black Carbon/Carbonaceous Aerosol Removal Experiment in Tokyo and Okinawa). The instruments and measurement parameters are summarized in Table 2.3. The standard SP2 measured the $N_{\text{air}}(D_{\text{BC}})$ and SCr. The humidified-SP2 (hSP2) measured the BC mass and the optical diameter of individual aerosol particles under a controlled RH. Selecting the dry BC-containing particles with a specific mass ($D_{\text{BC-shell}} \sim 200$ nm), the hygroscopicity parameter ($\kappa_{\text{BC-coat}}$) of non-BC aerosol compounds coating on a BC particle was measured [Ohata et al., 2016a]. The quadrupole aerosol mass spectrometer (AMS) analyzed the chemical composition of $\text{PM}_{1.0}$ (i.e., about 50% transmittance at 1 μm particle), using a quadrupole mass spectrometer [Jayne et al., 2000]. The size-resolved aerosol number concentrations are measured by the scanning mobility particle sizer (SMPS) within the 15.7–900 nm range or the wide-range particle spectrometer (WPS) within the 10.4–10000 nm range.

During precipitation, the $N_{\text{rain}}(D_{\text{BC}})$ was measured by an automated rain sampling system in Tokyo, described in section 2.1.8 [Mori et al., 2016]. In Okinawa, rainwater samples were collected on a daily basis, using a glass funnel inserted into the lid of glass bottle (150mL), and analyzed at the laboratory of University of Tokyo. The number size distribution of precipitation particles was measured by a laser precipitation monitor.

Table 2.3. Principle instruments employed to the simultaneous measurements of BC particles in air and rainwater in Tokyo and Okinawa.

	Instrument	Measurement parameters
Atmospheric measurement	Standard SP2	Size-resolved number concentration of BC $(70 < D_{BC} < 920 \text{ nm})$ Shell/core ratio $(200 < D_{BC} < 400 \text{ nm})$
	Humidified-SP2 (APM-hSP2)	Growth factor at 85% RH and hygroscopicity parameter κ of BC-free and BC-containing particles
	AMS	Chemical composition (excluding BC) of PM1 aerosols
Precipitation measurement	Automated rain sampling system	Precipitation rate, System that enabled the rain samples to be analyzed within about 3 min after the start of rainfall
	Laser precipitation monitor	Size-resolved number concentration of a precipitation particle
	Wide-range SP2	Size-resolved number and mass concentration of BC $(70 < D_{BC} < 4170 \text{ nm})$

2.1.10 Experimental Summary

Chapter 2.1 described the improved technique for measuring the size distribution of BC in rainwater by combining a pneumatic nebulizer (Marin-5) with a modified SP2 (WR-SP2). First, the upper limit of the size of BC detectable by the SP2 from 0.9 μm to about 4.0 μm was expanded by modifying the photo-detector for measuring the laser-induced

incandescence signal. Second, using PSL suspensions and AB-162 samples, the extraction efficiency of the Marin-5 was experimentally determined about 50.0 % and was size independent in the $70 < D_{BC} < 2000$ nm range, consistent with theoretically-estimated extraction efficiency. These results indicate that the combined Marin-5/WR-SP2 system enabled accurate measurement of the size distribution of BC particles in liquid water up to $D_{BC} = 4170$ nm. The reproducibility of the measured mass size distribution of BC in rainwater was about 12% in the $70 < D_{BC} < 300$ nm range.

In the laboratory, the possible changes in the size distribution of BC particles were investigated during the extraction process by the nebulizer and condensational growth of BC. First, the effect of coagulation of BC particles during the extraction process by the Marin-5 was negligibly small for BC mass concentrations in liquid water of less than $70 \mu\text{g L}^{-1}$, consistent with theoretical calculations. Second, BC diameter did not change during condensational growth in the particle growth chamber of a PILS.

To evaluate the overall performance of the Marin-5/WR-SP2 system, the size distribution of BC in air and rainwater was made simultaneously in Tokyo during summer 2014. The size distribution of BC in rainwater was larger than that in air, indicating that larger BC particles were removed more efficiently by precipitation.

These results, based on laboratory experiments, theoretical calculations, and field observations, strongly support the application of the Marin-5/WR-SP2 system to quantitative studies of wet deposition of BC.

2.2 Data Analysis Method

In precipitating clouds, BC-containing particles are mainly incorporated into a water droplet by impaction (below-cloud and in-cloud) and nucleation scavenging mechanisms. Former mechanism is that BC-containing particles are captured with falling droplets (raindrops and cloud droplets) and latter is that they are active as CCN. To explore the key mechanism and parameters controlling the wet removal efficiency of BC, I developed a new data analysis method using a parcel model, based on the measured D_{BC} dependence of wet removal efficiency and other observation data. Chapter 2.2 describes how to calculate the number fraction of BC particles scavenged by three scavenging mechanisms and the relative contribution of three scavenging mechanisms. The physical parameters used in the data analysis method are summarized in Table 2.4. The detail data-processing procedure for each scavenging mechanism is described in Appendix A1.

2.2.1 Methods

Data analysis method focuses on an air parcel ascending from the atmospheric planetary boundary layer (PBL) to the free troposphere (FT) via the moist convective process in Figure 2.20. Some number fractions of BC particles are scavenged by below-cloud impaction ($F_{bc-imp}(D_{BC})$), nucleation ($F_{ccn}(D_{BC})$), and in-cloud impaction ($F_{ic-imp}(D_{BC})$) mechanisms before the ascending air parcel reaches to cloud top. Three-distinct scavenged number fractions are calculated by assuming the updraft velocity (w , units of $m\ s^{-1}$) of the air parcel and the residence time (t , units of s) within the precipitating cloud. To investigate the relative contributions of three scavenging mechanisms, the best fitted w and t are explored by comparing the calculated D_{BC} dependence of total number fraction of BC particles ($F_{total}(D_{BC})$) and the measured D_{BC} dependence of $RE(D_{BC})$. Using the

estimates of w and t , the relative contributions of three scavenging mechanisms are determined.

Due to the estimate of w , the best estimated maximum supersaturation in air (SS_{\max}) is determined by an adiabatic parcel model (section 2.2.2.1). It is important to note that w , t , and SS_{\max} are an effective updraft velocity, residence time, and maximum supersaturation: weighted average of w , t , and SS_{\max} experienced by removed BC-containing particles in many different ascending air parcels.

According to an aircraft observation, actual updraft velocity in the atmosphere had a standard deviation [Fountoukis et al., 2007]. The data analysis method considered the distribution of w as Gaussian distribution with the relationship between average w and updraft standard deviation, obtained by the aircraft measurement [Fountoukis et al., 2007]. Selecting the median values of updraft velocity distribution (w_{med}) and residence time distribution (t_{med}), the number fractions of BC particles scavenged by below-cloud impaction ($\tilde{F}_{\text{bc-imp}}(D_{\text{BC}})$), nucleation ($\tilde{F}_{\text{ccn}}(D_{\text{BC}})$), and in-cloud impaction ($\tilde{F}_{\text{ic-imp}}(D_{\text{BC}})$) mechanisms and the total number fraction of BC particles ($\tilde{F}_{\text{total}}(D_{\text{BC}})$) are calculated. Selecting the w_{med} , the best estimated median value of maximum supersaturation distribution (SS_{med}) is determined.

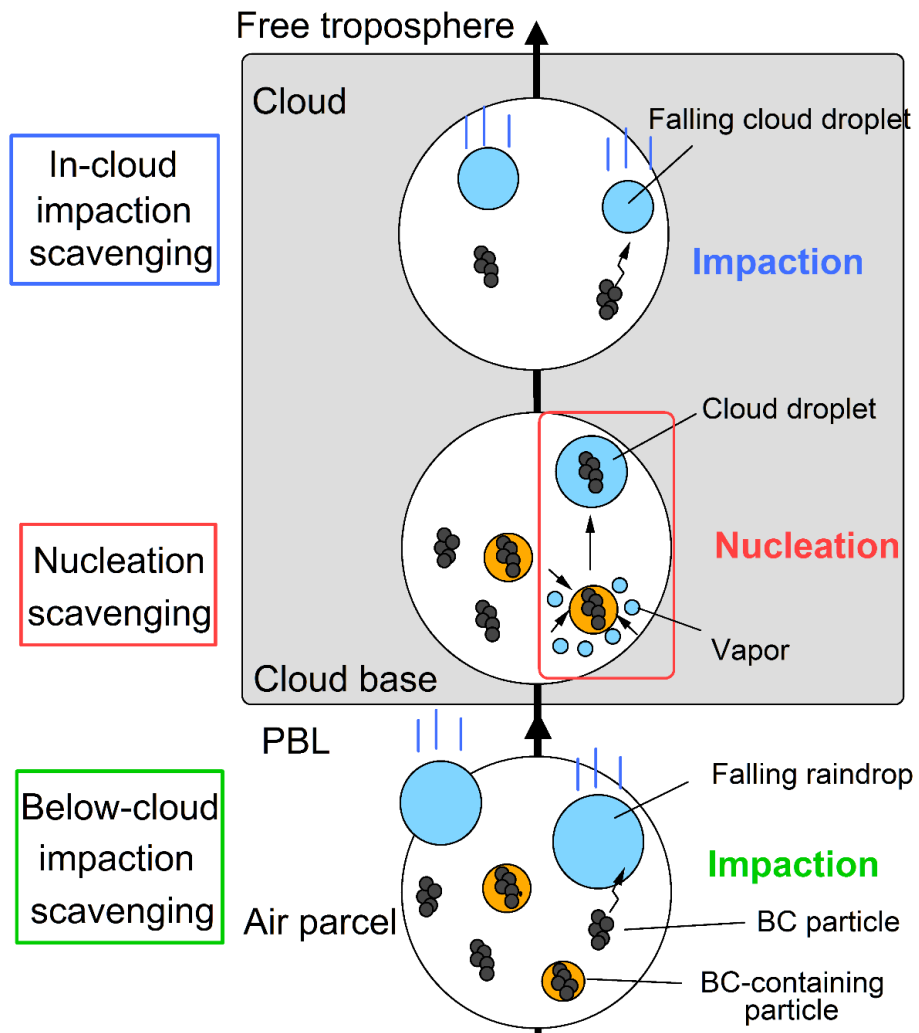


Figure 2.20. Schematic diagram of the parcel model. BC (or BC-containing) particles in the ascending air parcel are scavenged by the below-cloud impaction, nucleation, and in-cloud impaction mechanisms, continuously.

Table 2.4 List of symbols used in the data analysis method. Uncertainties in some parameters are also shown.

(a) Nucleation scavenging mechanism

	Symbols	Descriptions	Uncertainty
Observation	D_{BC}	BC mass equivalent diameter	
	$\kappa_{BC-coat}$	Hygroscopicity parameter for BC-coating materials ($D_{BC-shell} = \sim 200\text{nm}$)	
	SCr	Shell/core ratio ($200 < D_{BC} < 400 \text{ nm}$)	
	N_{air}	BC number concentration in air	
	$N_{aerosol}$	Total number concentration of aerosol particles ($D < 900\text{nm}$)	
		Chemical composition of PM1 aerosols	
Estimate	SCr	Shell/core ratio ($70 < D_{BC} < 200 \text{ nm}$ and $400 < D_{BC} < 2000 \text{ nm}$)	$\sim 4.0 \%$ (Section 3.2.9)
Assumed parameter	w	Updraft velocity	
Known values	σ_w	Surface tension of pure water (= 0.072 J/m^2)	
	M_w	Molecular weight of water (= 18.02 g/mol)	
	R	Universal gas constant (= 8.315 J/mol K)	
	T	Temperature at ground (= 298 K)	2.0%
	ρ_w	Density of water (= 1.0 g/cm^3)	
	RH	Relative humidity at ground (= 80%)	5.0%
	P_{air}	Atmospheric pressure (= 1013 hPa)	
	κ_{BC}	Hygroscopicity parameter for BC core (= 0.0)	
Calculation	a_w	Activity of water in solution	
	κ	Hygroscopicity parameter for BC-containing particles	
	N_{CCN}	Activated BC number concentration in air	
	Sc	Critical supersaturation for BC-containing particles	
	SS_{max}	Maximum supersaturation in air	
	F_{CCN}	Number fraction of BC-containing particles scavenged by nucleation mechanism	$\sim 9.0 \%$ (Section 3.2.9)

(b) Impaction scavenging mechanism

	Symbols	Descriptions	Uncertainty
Observation	N_{air}	Size-resolved BC number concentration in air	
	$N_{\text{d_rain}}$	Size-resolved raindrop number concentration	
Assumed parameter	t_{rain}	Time when an air parcel ascends from the ground to cloud base	
	t_{cloud}	Time when an air parcel ascends from cloud base to cloud top in a precipitating cloud	
Calculation	K	Collection kernel for various attachment processes between a BC particle and a water droplet	4.2 % (Appendix A1)
	A	Scavenging ratio	4.2 %
	$N_{\text{d_cloud}}$	Size-resolved cloud droplet number concentration, calculated by using parcel model	
	$F_{\text{bc-imp}}$	Number fraction of BC particles scavenged by below-cloud impaction mechanism	4.2 % (Section 3.2.9)
	$F_{\text{ic-imp}}$	Number fraction of BC particles scavenged by in-cloud impaction mechanism	

2.2.2 Nucleation Scavenging of BC Particles

This section derives how to calculate $F_{\text{CCN}}(D_{\text{BC}})$. Figure 2.21 shows the diagram of data-processing procedure for calculating the $F_{\text{CCN}}(D_{\text{BC}})$, which depends on the critical supersaturation (Sc) of BC-containing particle and the SS_{max} in air. To investigate the Sc of dry particle, Petters and Kreidenweis [2009] derived the relationship between dry particle diameter (D_{dry}) and CCN activity using a hygroscopicity parameter κ , which was called as “ κ -Kohler theory”. For a BC-containing particle, the equation is represented as

$$S(D_w) = a_w * \exp\left(\frac{4\sigma_w M_w}{RT\rho_w D_{\text{wet}}}\right), \quad (2.11)$$

$$a_w = \frac{D_{\text{wet}}^3 - D_{\text{dry}}^3}{D_{\text{wet}}^3 - D_{\text{dry}}^3(1 - \kappa)}, \quad (2.12)$$

$$\kappa = \sum_i \varepsilon_i \kappa_i \quad (2.13)$$

where a_w is the activity of water in solution, S is the saturation vapor pressure over the surface of droplet of diameter D_{wet} , D_{dry} is the dry diameter ($D_{\text{BC-shell}} = D_{\text{BC}} \times \text{SCR}$) of a BC-containing particle with a hygroscopicity parameter κ , σ_w is the surface tension of pure water, M_w is the molecular weight of water, R is the universal gas constant, T is the temperature, and ρ_w is the density of water. The κ for a BC-containing particle is given by the single mixing rule, which is represented by the individual component volume fraction ε_i and the individual component hygroscopicity parameter κ_i in equation (2.13). Thus, the κ for BC-containing particles is calculated by using hygroscopicity parameter ($\kappa_{\text{BC-coat}}$) for non-BC aerosol compounds coating on a BC particle and the hygroscopicity parameter ($\kappa_{\text{BC}} = 0$) of BC core. These parameters are summarized in Table 2.4 (a).

The a_w of a droplet depends on the solute in equation (2.12) and decreases the equilibrium vapor pressure (Solute effect). On the other hand, the exponential term of equation (2.11) increases the equilibrium vapor pressure as the D_{wet} decreases (Kelvin effect). Due to comparison of both equilibrium vapor pressures, S has a maximum value for a BC-containing particle with D_{dry} and κ . The maximum value is called as critical supersaturation S_c , which is a key parameter to determine the CCN activation of the dry particles. The SS_{max} is calculated by using an adiabatic cloud parcel model in section 2.2.2.1, depending on the observed total number concentrations of aerosol particles

(N_{aerosol}), chemical compositions of PM1 aerosols, and estimated w in Figure 2.21 [Feingold and Heymsfield, 1992; Feingold et al., 2003]. If the SS_{max} exceeds Sc , a BC-containing particle starts growing and becomes a cloud droplet. Comparing the SS_{max} and Sc , the activated number fraction of BC-containing particles ($F_{\text{ccn}}(D_{\text{BC}})$) is calculated as the ratio of activated BC number concentration ($N_{\text{CCN}}(D_{\text{BC}})$) to $N_{\text{air}}(D_{\text{BC}})$.

2.2.2.1 Determination of Maximum Supersaturation in Air

SS_{max} in an ascending air parcel is determined by using an adiabatic cloud parcel model [Feingold and Heymsfield, 1992; Feingold et al., 2003], which assumes 1) no collision-coalescence process, 2) no entrainment, 3) no horizontal advection of liquid water into an air parcel, 4) a constant cloud water content, and 5) a constant droplet mixing ratio after SS_{max} reaches.

The supersaturation changes by the vapor budget in ascending air parcel, depending on the supply of vapor by saturated air that is cooled in ascent and the loss of vapor by condensation. In other words, the rate of change of the supersaturation depends on the w and the condensation rate of vapor. By comparing the increase of supersaturation due to supply of vapor and the decrease of supersaturation due to the condensation of vapor on droplets, maximum supersaturation (SS_{max}) is calculated in the model.

The condensation rate depends on the N_{aerosol} and the chemical compositions of ambient non-refractory submicron aerosol. This study determined the SS_{max} for a constant w by using the observation data (N_{aerosol} and chemical compositions of ambient non-refractory submicron aerosols within 1-h period before the onset of precipitation) and meteorological data (T , RH , and atmospheric pressure). To calculate the $F_{\text{ic-imp}}(D_{\text{BC}})$, the number size distribution of cloud droplets ($N_{\text{d_cloud}}(D_{\text{d}})$) was also calculated in the model.

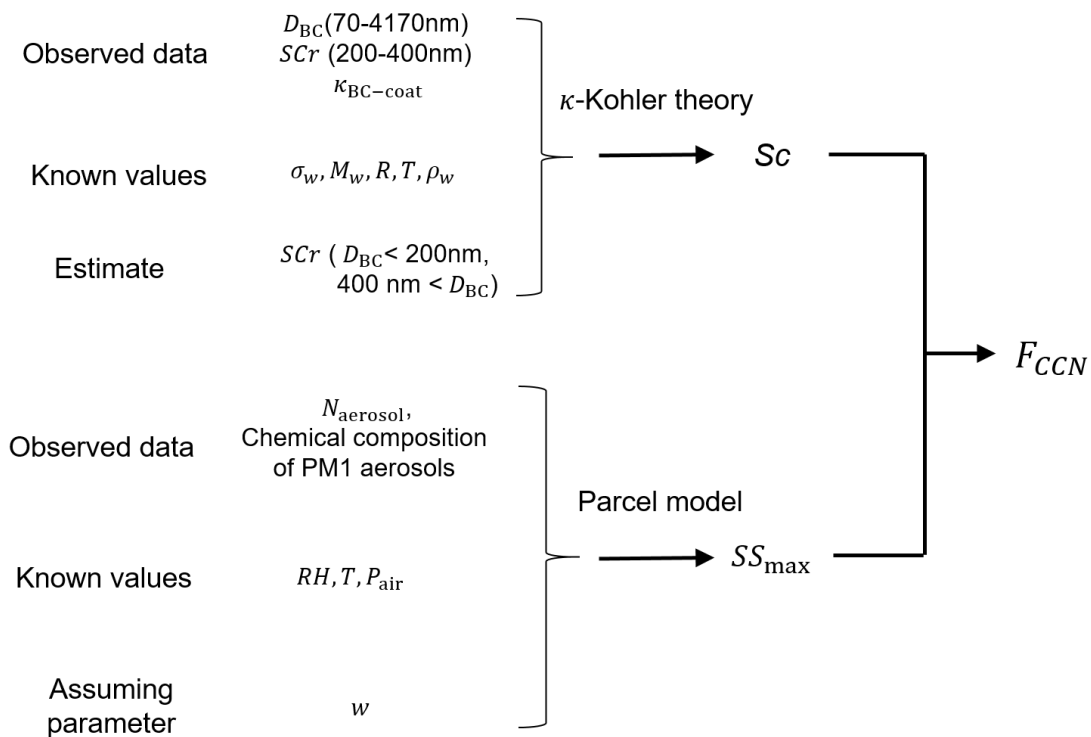


Figure 2.21. Diagram of data-processing procedure for calculating the number fraction of BC-containing particles scavenged by nucleation mechanism.

2.2.2.2. Theoretically-Estimated Dry Shell/Core Ratio

Due to the detection limit of SP2, the SCr was measured within $200 < D_{BC} < 400\text{nm}$ range. To calculate the $F_{ccn}(D_{BC})$ within $70 < D_{BC} < 2000\text{ nm}$ range, this section theoretically estimates the SCr within $70 < D_{BC} < 200\text{ nm}$ and $400 < D_{BC} < 2000\text{ nm}$ range on the basis of the observed SCr. This calculation assumes that the sufficient sulfate in the air uniformly and continuously condenses on a BC particle. The physical parameters and the uncertainties used in estimate of SCr are summarized in Table 2.5. The uncertainties are discussed in section 3.2.9.

According to the condensation theory [Seinfeld and Pandis, 2006], the condensation growth rate of a BC-containing particle with $D_{\text{BC-shell}}$ is represented as the rate of volume change of the particle. The rate of diameter change of the particle is represented as

$$\frac{dD_{\text{BC-shell}}}{dt} = \frac{4D_i M_i}{RT \rho_{\text{BC}}} [p_i - p_{\text{eq},i}(D_{\text{BC-shell}})] \times \frac{1}{D_{\text{BC-shell}}}, \quad (2.14)$$

$$p_{\text{eq},i}(D_{\text{BC-shell}}) = p_{\text{flat},i} \times \exp\left[\frac{4\sigma_i M_i}{RT \rho_i D_{\text{BC-shell}}}\right], \quad (2.15)$$

where D_i is the diffusion coefficient for sulfate in air, M_i is its molecular weight, σ_i is the surface tension at certain temperature, ρ_i is the density of sulfate [Seinfeld and Pandis, 2006], and ρ_{BC} is a true density of BC particle. p_i is the vapor pressure of sulfate surrounding the BC particle, $p_{\text{eq},i}$ is the equivalent vapor pressure of a BC-containing particle, and $p_{\text{flat},i}$ is vapor pressure of sulfate over a flat surface [Seinfeld and Pandis, 2006]. The SCr is estimated by condensation theory considering the Kelvin effect in equation 2.14 because the sulfate on BC particles easily evaporates for $D_{\text{BC-shell}} < 100$ nm in equation 2.15.

To estimate the SCr for $D_{\text{BC}} < 200$ nm, the time (t_{grow}) growing from the volume of a BC particle with $D_{\text{BC}} = 200$ nm to that of a BC-containing particle with $D_{\text{BC-shell}}$ by condensation is calculated in equation. 2.14. Assuming that the volume of a BC particle with $D_{\text{BC}} < 200$ nm grows to that of a BC-containing particle with $D_{\text{BC-shell}}$ at t_{grow} , the SCr for $D_{\text{BC}} < 200$ nm is estimated. The SCr for $D_{\text{BC}} > 400$ nm is also estimated on the basis of the observed $D_{\text{BC-shell}}$ for $D_{\text{BC}} = 400$ nm.

Table 2.5 List of symbols used in estimates of SCr. The uncertainties are also shown.

	Symbols	Description	Uncertainty	Reference	
Given parameter	D_i	Diffusion coefficient of SO ₂ (=0.123 [cm ² /s])	14%	Tang et al. [2014]	
	M_i	Molecular weight of H ₂ SO ₄ (= 98.1 [g/mol])			
	σ_i	Surface tension of H ₂ SO ₄ (l) at RH = 80% (= 0.074 [kg/s ²])	1.0%	Seinfeld and Pandis [2006]	
	ρ_i	Density of H ₂ SO ₄ (l) at RH = 80% (= 1.11 [g/cc])	5.0%		
	p_i	Vapor pressure of sulfate surrounding over BC particle (= 1.0×10^{-7} [Pa])	5.0%		
	$p_{\text{flat},i}$	Vapor pressure of sulfate over a flat surface (= 1.33×10^{-8} [Pa])	5.0%		
		ρ_{BC}	Density of BC (=1.80 g/cc)	5.0%	Moteki et al.[2010]
		R	Universal gas constant (= 8.32 J/mol K)		
		T	Temperature (= 298 K)	2.0 %	
Calculation	$\frac{dD_{\text{BC-shell}}}{dt}$	Condensation growth rate for a BC-containing particle with $D_{\text{BC-shell}}$	~ 16%		

2.2.3 Impaction Scavenging of BC Particles

This section describes how to calculate the $F_{\text{bc-imp}}(D_{\text{BC}})$ and $F_{\text{ic-imp}}(D_{\text{BC}})$. The diagram of data-processing procedure is shown in Figure 2.22. $F_{\text{bc(ic)-imp}}(D_{\text{BC}})$ are derived from the following equations [Flossmann et al., 1985; Seinfeld and Pandis, 2006],

$$-\frac{\partial N_{\text{air}}(D_{\text{BC}}, t)}{\partial t} = N_{\text{air}}(D_{\text{BC}}, t) \int_0^{\infty} K(D_{\text{BC}}, D_d) N_d(D_d, t) dD_d, \quad (2.16)$$

where $N_{\text{air}}(D_{\text{BC}}, t)$ is the time-dependent BC number concentrations in air during precipitation at time t , D_{d} is an droplet (raindrop or cloud droplet) diameter, and $N_{\text{d}}(D_{\text{d}}, t)$ is the size-resolved number concentration of droplets at time t . $N_{\text{d}}(D_{\text{d}}, t)$ for raindrop and cloud droplet is written as $N_{\text{d_rain}}(D_{\text{d}}, t_{\text{rain}})$ and $N_{\text{d_cloud}}(D_{\text{d}}, t_{\text{cloud}})$, respectively. $K(D_{\text{BC}}, D_{\text{d}})$ is the collection kernel for various attachment processes between a BC particle and a water droplet. The calculation of $K(D_{\text{BC}}, D_{\text{d}})$ is described in Appendix A1. In the calculation, the most important collection mechanisms for impaction are considered, which are Brownian diffusion, interception, and inertial impaction [Wang et al. 2010]. If the $N_{\text{d}}(D_{\text{d}}, t)$ does not vary with time, the $N_{\text{air}}(D_{\text{BC}}, t)$ is simply described as

$$N_{\text{air}}(D_{\text{BC}}, t) = N_{\text{air}}(D_{\text{BC}}, 0) \times \exp[-\Lambda(D_{\text{BC}})t], \quad (2.17)$$

$$\Lambda(D_{\text{BC}}) = \int_0^{\infty} K(D_{\text{BC}}, D_{\text{d}})N_{\text{d}}(D_{\text{d}})dD_{\text{d}}, \quad (2.18)$$

where $\Lambda(D_{\text{BC}})$ is a deposition rate of the BC number concentration by scavenging, called as *scavenging ratio*. Using the equation (2.17), $F_{\text{bc(ic)-imp}}(D_{\text{BC}})$ at time t is represented as:

$$F_{\text{bc(ic)-imp}}(D_{\text{BC}}) = \frac{N_{\text{air}}(D_{\text{BC}}, 0) - N_{\text{air}}(D_{\text{BC}}, t)}{N_{\text{air}}(D_{\text{BC}}, 0)}. \quad (2.19)$$

Using the equation (2.17), (2.18), and (2.19), $F_{\text{bc(ic)-imp}}(D_{\text{BC}})$ is determined by

$$F_{bc(ic)-imp}(D_{BC}) = 1 - \exp \left[-t \int_0^{\infty} K(D_{BC}, D_d) N_d(D_d) dD_d \right]. \quad (2.20)$$

The t means the time (t_{rain}) during which BC particles has collided with raindrops below cloud for the calculation of $F_{bc-imp}(D_{BC})$ and the time (t_{cloud}) during which BC particles has collided with cloud droplets within precipitating cloud for the calculation of $F_{ic-imp}(D_{BC})$. Thus, the t_{rain} and t_{cloud} mean the time during which the air parcel ascends from the ground to cloud base and from cloud base to cloud top, respectively. By using t and observational data, $F_{bc(ic)-imp}(D_{BC})$ is calculated in the equation (2.20).

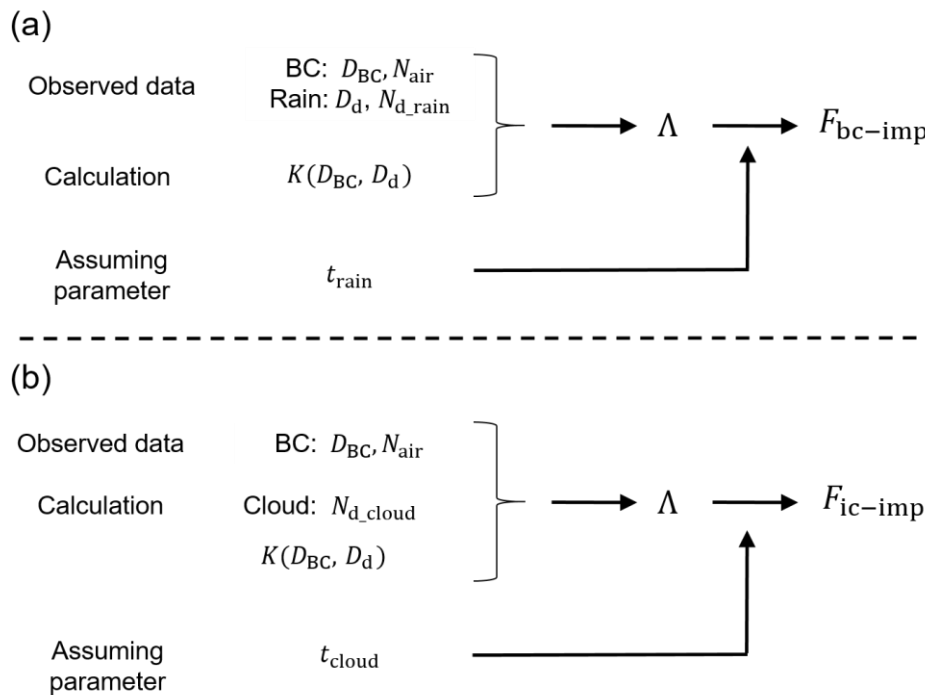


Figure 2.22. Diagram of data-processing procedure for calculating the number fraction of BC particles scavenged by (a) below-cloud impaction and (b) in-cloud impaction mechanisms.

2.2.4 Summary

A new data analysis method for exploring the relative contribution of the three-distinct (below-cloud impaction, nucleation, and in-cloud impaction) scavenging mechanisms of BC in a precipitating cloud was developed in Chapter 2.2, based on the D_{BC} -dependence of wet removal efficiency and other observation data (e.g., Hygroscopic parameter for BC-coated materials, BC-mixing state, size-distribution of raindrop). Assuming the updraft velocity (w) and time residence (t) in the precipitating cloud, these scavenged number fractions of BC are theoretically calculated. The best estimated w and t are explored by comparing the measured D_{BC} dependence of $RE(D_{BC})$ with the calculated D_{BC} dependence of $F_{total}(D_{BC})$ to determine the relative contribution of three-distinct scavenging mechanisms of BC.

In the data analysis method, the original calculation method was incorporated into the calculation of $F_{ccn}(D_{BC})$ and $F_{ic(bc)-imp}(D_{BC})$. First, to calculate the $F_{ccn}(D_{BC})$ in the $70 < D_{BC} < 2000$ nm range, the SCr for $D_{BC} < 200$ nm and $400 \text{ nm} < D_{BC}$ was estimated by using the condensation theory. Second, to calculate the $F_{ic(bc)-imp}$ for non-spherical BC particle, this dissertation calculates $K(D_{BC}, D_d)$ depending on the shape and size of BC (Appendix A1). This method enables the accurate calculation of the number fractions of BC particles scavenged by below-cloud impaction, nucleation, and in-cloud impaction mechanisms.

3. Field Observation on Wet Removal Mechanism of Black Carbon in Tokyo and Okinawa

3.1 Observation Site

Ground-based observations in Tokyo were conducted from 27 July through 15 August 2014 and from 2 July through 15 July 2015 at Hongo campus of the University of Tokyo (35.71°N, 139.76°E). BC particles emitted from Tokyo were thinly coated [Kondo et al., 2011b] and became internally mixed on a time scale of ~12 hours in urban plumes [Moteki et al., 2007].

Ground-based observations in Okinawa were also conducted from 9 March through 26 March 2016 at the Cape Hedo Aerosol and Atmosphere Monitoring Station (26.87°N, 128.26°E). During every spring, Cape Hedo is often strongly influenced by East Asian pollutions mainly emitted from China [Verma et al., 2011]. BC particles observed in Cape Hedo are thickly-coated with sulfate and organic by several days aging during the transport from China to the observation site. In addition, the column BC mass concentrations were rather uniform near Hedo in Figure A3.1, suggesting that the measurement of BC at Cape Hedo was representative of that region [Mori et al., 2014].

3.2 Results and Discussions

3.2.1 Meteorological Conditions

Typical meteorological conditions during observation periods in Tokyo and Okinawa were described in this section. Figure 3.1 shows surface weather maps at 0900JST(0000UTC) for 3 days in Tokyo and 1 day in Okinawa, which are the typical

weather conditions. 31 rainfall events were observed in Tokyo and 11 rainfall events were observed in Okinawa, respectively.

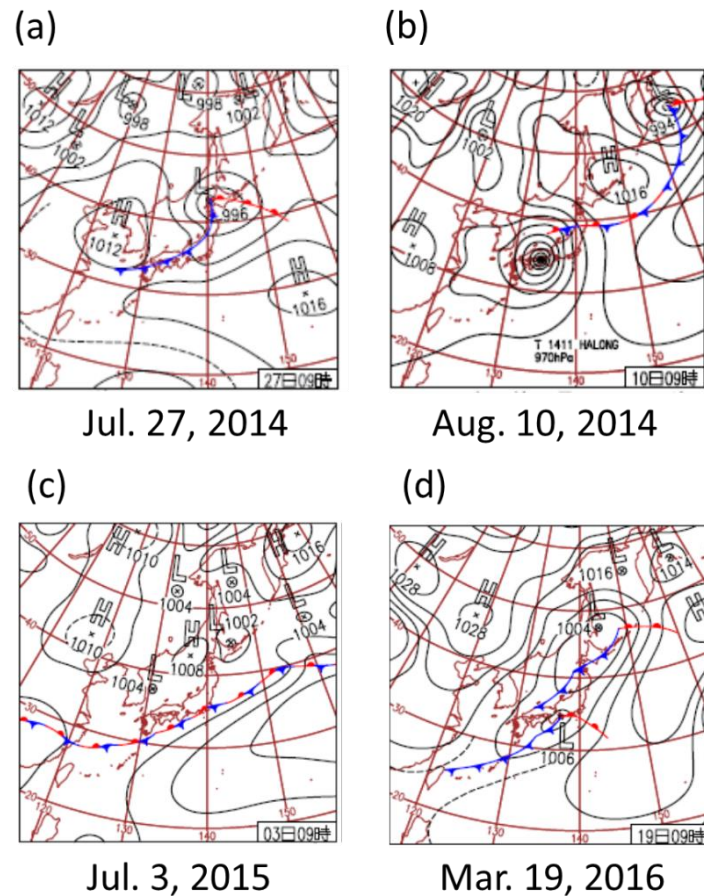


Figure 3.1. Surface weather maps of East Asia on (a) 27 July 2014, (b) 10 August 2014, (c) 3 July 2015, and (d) 19 March 2016 at 0900 local time.

In Tokyo, approximately 30% of precipitation during the observation period occurred when migratory cyclones and a cold front associated with migratory cyclones passed through the observation site (Figure 3.1a). Approximately 62% of the precipitation during the observation period occurred when a stationary front passed through the

observation site (Figure 3.1c). Precipitation due to typhoon also occurred in several rain events (Figure 3.1b). The precipitation intensity during observation period was 7.41 ± 5.91 mm/h on average.

In Okinawa, approximately 64% of precipitation during the observation period occurred when migratory cyclones and a cold front associated with a cyclone passed through the observation site (Figure 3.1d). Precipitation due to a stationary front also occurred in a few rain events. The precipitation intensity during observation period was 4.48 ± 4.21 mm/h on average.

3.2.2 Vertical and Horizontal Aerosol Distributions

The vertical and horizontal aerosol distributions during observation period were investigated. The monitoring extinction coefficient of vertical aerosol distribution by a light detection and ranging (LIDAR) near both observation sites revealed that aerosols were uniformly concentrated below the cloud base altitude ($< \sim 1$ km).

The horizontal BC distribution was investigated by measuring the variation of time-dependent number size distribution of BC ($N_{\text{air}}(D_{\text{BC}})$). The normalized $N_{\text{air}}(D_{\text{BC}})$ in air within 3-h period before precipitation began and within 1-h period before precipitation began were compared to be largely invariable within 10% in the $70 < D_{\text{BC}} < 400$ nm range, indicating that distribution of BC particles transported to observation site was time-independent within the range of 3-h before the onset of precipitation. Thus, the average BC distribution was horizontally uniform during the 3-h period before the onset of precipitation. For these reasons, this study assumes that the BC-containing particles observed within 1-h period before the onset of precipitation represent the initial condition of BC particles suspended in rainwater.

3.2.3 Dry Shell/Core Ratio and Chemical Compositions

Figure 3.2 shows average size-resolved median shell/core ratio (SCr) for all rain events in Tokyo and Okinawa within the $70 < D_{BC} < 2000$ nm range (Observed D_{BC} range: $200 < D_{BC} < 400$ nm, Estimated D_{BC} range: $70 < D_{BC} < 200$ nm and $400 \text{ nm} < D_{BC} < 2000$ nm). The average SCr with $D_{BC} = 200$ nm in Tokyo and Okinawa were 1.06 ± 0.05 and 1.25 ± 0.07 , respectively. The result in Tokyo was consistent with the previous study in Tokyo during Aug–Sep 2009 (SCr = 1.1 with $D_{BC} = 200$ nm) [Kondo et al., 2011]. The median SCr with smaller D_{BC} increased because the condensation growth rate of BC-containing particles with smaller D_{BC} was much faster than that of particles with larger D_{BC} .

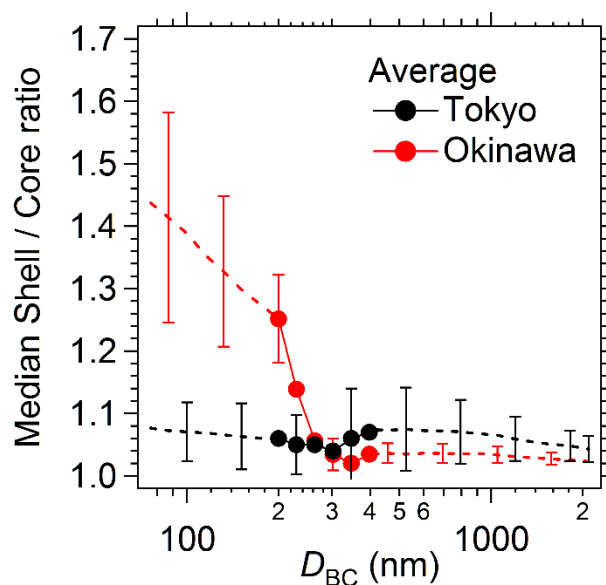


Figure 3.2. The average size dependence of median shell/core ratio for all rain events in Tokyo and Okinawa. The observed SCr range is $200 < D_{BC} < 400$ nm (line) and the estimated SCr range is $70 < D_{BC} < 200$ nm and $400 < D_{BC} < 2000$ nm (dotted line). Bars indicate the standard deviations for all rain events.

The chemical composition of ambient non-refractory submicron aerosol during observation periods was observed. Organics were dominant component in Tokyo, consistent with a previous study [Takegawa et al., 2006] and the volume fraction of organics was approximately 65%. In Okinawa, sulfate was dominant component, consistent with a previous study [Takami et al., 2007], and the volume fraction of sulfate was approximately 54%. The volume fraction of BC particles was less than 4%.

3.2.4 Observed Wet Removal Efficiency

Figure 3.3 shows the normalized $N_{\text{air}}(D_{\text{BC}})$ within the last 1-h period before the onset of precipitation, the normalized number size distribution in rainwater ($N_{\text{rain}}(D_{\text{BC}})$), and relative wet removal efficiency ($RE(D_{\text{BC}}) = N_{\text{rain}}(D_{\text{BC}}) / N_{\text{air}}(D_{\text{BC}})$) for 31 rain events in Tokyo and for 11 rain events in Okinawa (thin lines). Each $RE(D_{\text{BC}})$ is scaled to 1.0 at $D_{\text{BC}} = 200$ nm for illustrative convenience. Bold lines show the average result for all rain events. In Tokyo, the size of BC in rainwater was larger than that of BC in air and $RE(D_{\text{BC}})$ strongly depended on the size for each rain event, indicating that large BC particles were more efficiently removed by precipitation. On average, $RE(100\text{nm})$ and $RE(794\text{nm})$ were 0.47 and 3.70, respectively. The D_{BC} dependence of $RE(D_{\text{BC}})$ during summer 2014 was similar to that of $RE(D_{\text{BC}})$ during summer 2015 on average. In Okinawa, on the other hands, the size of BC in rainwater was similar to that of BC in air and $RE(D_{\text{BC}})$ was largely independent of the size in the $70 < D_{\text{BC}} < 457$ nm range, indicating the BC particles were uniformly removed by precipitation in the $70 < D_{\text{BC}} < 457$ nm range. On average, $RE(100\text{nm})$ and $RE(457\text{nm})$ were 1.07 and 1.08, respectively.

Based on the observed D_{BC} dependence of $RE(D_{\text{BC}})$ and other observation data, the key process and parameter controlling the D_{BC} dependence of wet removal efficiency

were explored in the section 3.2.5 and section 3.2.6.

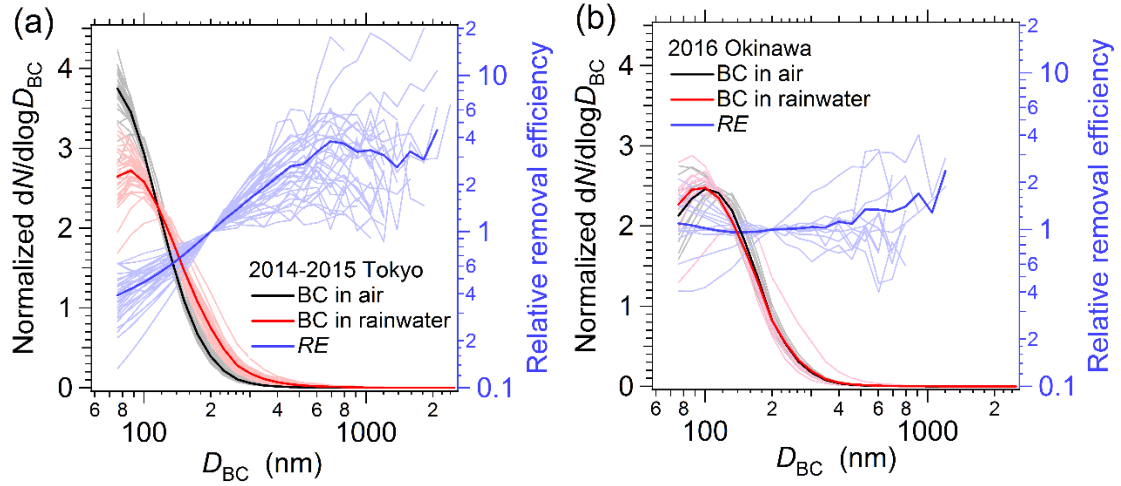


Figure 3.3. (a) Normalized number size distributions of BC in air and rainwater for 31 rain events in Tokyo, and (b) normalized number size distributions of BC in air and rainwater for 11 rain events in Okinawa (thin lines). Ratios of the normalized number size distributions in rainwater to that in air are also shown (thin lines). The ratios are scaled to 1.0 at $D_{BC} = 200\text{nm}$. Bold lines show the average results for all rain events in Tokyo and Okinawa.

3.2.5 Relative Contribution of Scavenging Mechanisms of BC

This section explores the relative contribution of three-distinct (below-cloud impaction, nucleation, in-cloud impaction) scavenging mechanisms by using the data analysis method, based on the observation data and measured D_{BC} dependence of $RE(D_{BC})$. For the typical size distributions of BC in air and rainwater, the examples of the observed relative $RE(D_{BC})$ and the calculated $\tilde{F}_{bc-imp}(D_{BC})$, $\tilde{F}_{ccln}(D_{BC})$, and $\tilde{F}_{ic-imp}(D_{BC})$ are

shown in Figure 3.4. The parameters and values related with the derivation of w_{med} and SS_{med} were summarized in Table 3.1. The rain events in Figure 3.4(a1), (a2), (b1), and (b2) are called as the Event a1, Event a2, Event b1, and Event b2, respectively.

In Tokyo, the w_{med} values in Event a1 and Event a2 were estimated to be 0.10 m/s and 0.15 m/s, respectively. Both SS_{med} values were estimated to be 0.09 % and 0.17 %, respectively. The estimate of SS_{med} in Event a2 was higher than that of SS_{med} in Event a1 because of the lower aerosol number concentrations and the faster updraft velocity in Event a2. $\tilde{F}_{\text{bc-imp}}(D_{\text{BC}})$ in both events were nearly 0, indicating that the majority of BC particles were not scavenged by below-cloud impaction mechanism. For smaller D_{BC} , $\tilde{F}_{\text{ic-imp}}(D_{\text{BC}})$ increased because BC particles were captured with falling cloud droplets by Brownian diffusion (Appendix A1). $\tilde{F}_{\text{ic-imp}}(D_{\text{BC}})$ in Event a2 was larger than that in Event a1 because the t_{med} in precipitating cloud in Event a2 was longer than that in Event a1.

In Okinawa, it was very difficult to estimate w_{med} because measured D_{BC} -independence of $RE(D_{\text{BC}})$ can consist of the multiple combinations of the D_{BC} -dependence of $\tilde{F}_{\text{bc-imp}}(D_{\text{BC}})$, $\tilde{F}_{\text{ccn}}(D_{\text{BC}})$, and $\tilde{F}_{\text{ic-imp}}(D_{\text{BC}})$. To investigate the relative contribution of three-distinct scavenging mechanism of BC, this dissertation assumed that the range of w_{med} in Tokyo was the same as that of w_{med} in Okinawa (i.e. $0.05 < w_{\text{med}} < 0.5$ m/s). Figure 3.4 (b) shows the average and standard deviations of $\tilde{F}_{\text{bc-imp}}(D_{\text{BC}})$, $\tilde{F}_{\text{ccn}}(D_{\text{BC}})$, and $\tilde{F}_{\text{ic-imp}}(D_{\text{BC}})$ within the $0.05 < w_{\text{med}} < 0.5$ m/s range. The SS_{med} range in Event b1 and Event b2 were estimated to be 0.09–0.25 % and 0.10–0.25%, respectively.

Table 3.1. Precipitation type, the observed precipitation intensity (P), aerosol number concentrations (N_a), shell/core ratio (SCr) with $D_{BC} = 200\text{nm}$, hygroscopicity parameter of BC-containing particles ($\kappa_{BC\text{-coat}}$), and the estimated w_{med} and SS_{med} for each rain event in Tokyo and Okinawa in Figure 3.4.

	Tokyo		Okinawa	
Event	Event a1	Event a2	Event b1	Event b2
Day	Aug 12, 2014	Jul 6, 2015	Mar 9, 2016	Mar 10, 2016
Cloud type	a cold front	a stationary front	a cold front	a cold front
Observed P [mm/h]	2.8	2.4	5.8	0.6
Observed N_a [#/cc]	5833	3700	613	1238
Observed SCr	1.06	1.05	1.28	1.24
Observed $\kappa_{BC\text{-coat}}$	0.21	0.26	0.37	0.39
w_{med} [m/s]	0.10	0.15	0.05–0.5	0.05–0.5
SS_{med} [%]	0.09	0.17	0.09–0.25	0.10–0.25

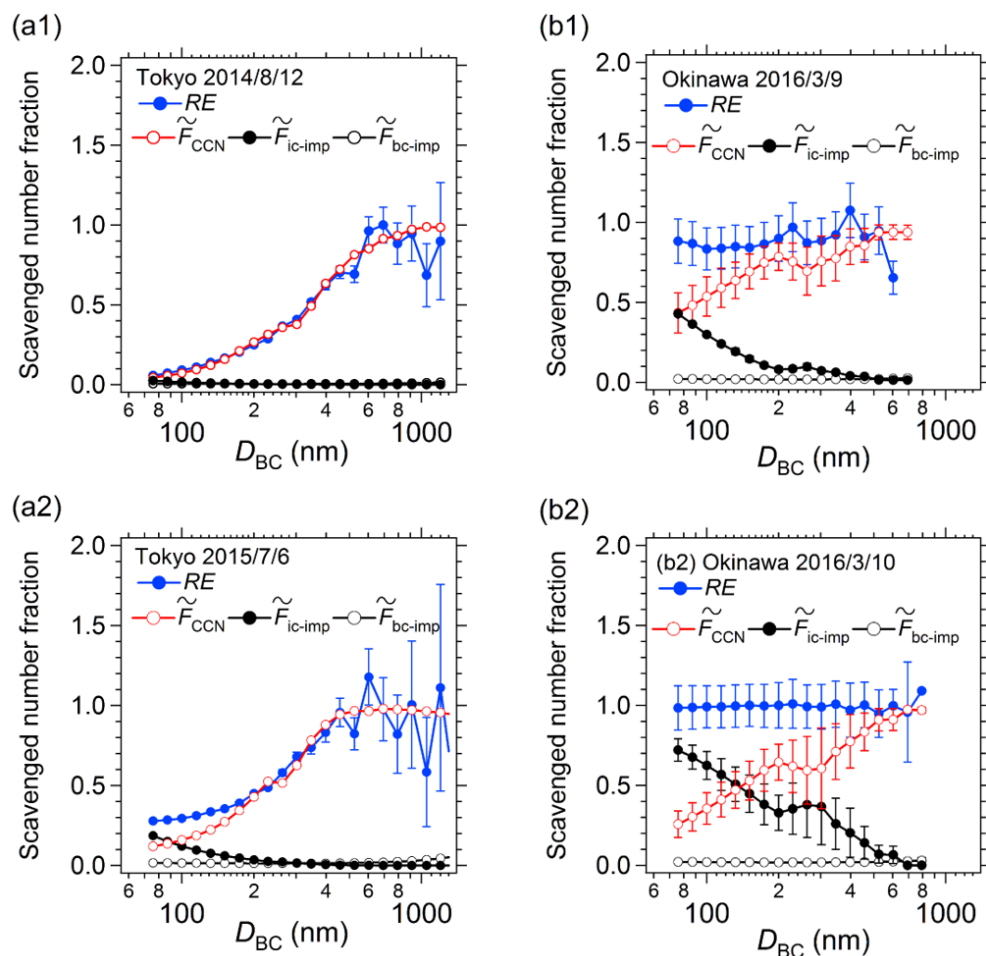


Figure 3.4. (a) The size-resolved wet removal efficiency ($RE(D_{BC})$) and the number fractions of BC particles scavenged by nucleation ($\tilde{F}_{CCN}(D_{BC})$), below-cloud impaction ($\tilde{F}_{bc-imp}(D_{BC})$), and in-cloud impaction ($\tilde{F}_{ic-imp}(D_{BC})$) mechanism in Tokyo, which is observed on Aug 12, 2014 and on Jul 6, 2015, respectively. Bars of $RE(D_{BC})$ indicate 1σ of a Poisson distribution. (b) The average $RE(D_{BC})$, $\tilde{F}_{CCN}(D_{BC})$, $\tilde{F}_{bc-imp}(D_{BC})$, and $\tilde{F}_{ic-imp}(D_{BC})$ within the $0.05 < w_{med} < 0.5$ m/s range in Okinawa, which is observed on Mar 9, 2016 and on Mar 10, 2016. Bars indicate the standard deviations of the scavenged number fraction of BC within the $0.05 < w_{med} < 0.5$ m/s range.

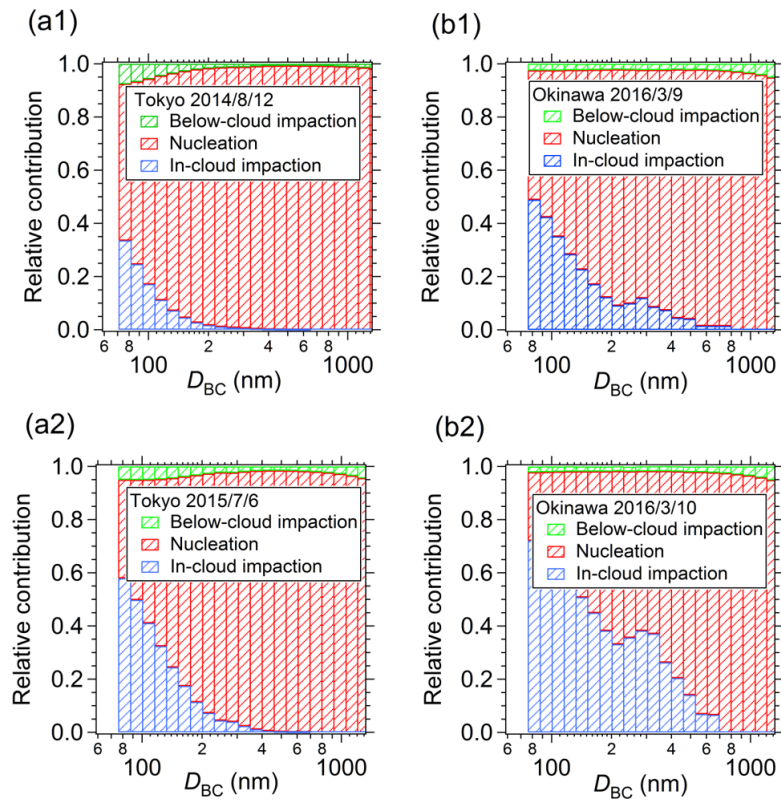


Figure 3.5. (a) Relative contribution of three-distinct scavenging mechanisms of BC in Tokyo in Figure 3.4. (b) Average relative contribution of three scavenging mechanisms within the $0.05 < w_{med} < 0.5$ m/s range in Okinawa.

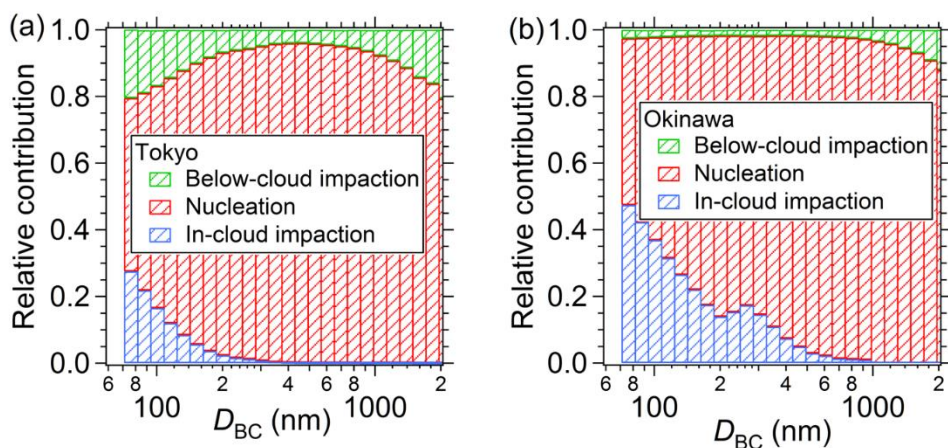


Figure 3.6. Average relative contribution of three-distinct scavenging mechanisms of BC (a) for 31 rain events in Tokyo and (b) for 11 rain events in Okinawa

For observed 31 rain events in Tokyo, the median value (25th percentile, 75th percentile) of w_{med} was estimated to be 0.10 (0.05, 0.23) m/s, which was reasonable value, compared with the value of average updraft velocity (0.12 ± 0.13 m/s) at cloud base by aircraft observation in the vicinity of Cleveland and Detroit [Fountoukis et al., 2007]. To make the accurate evaluation of the w_{med} , it is necessary to compare the w_{med} with the observed updraft velocity in Tokyo.

The median value of SS_{med} for 31 rain events in Tokyo was estimated to be 0.11 (0.07, 0.18) %, which was also reasonable value because the typical maximum supersaturation in convective updrafts is the order of 1-2 %. The average SS_{med} values for each precipitation type of cold front ($0.14 \pm 0.05\%$), stationary front ($0.13 \pm 0.09\%$), and typhoon ($0.11 \pm 0.02\%$) were similar. Moreover, the SS_{med} was poorly correlated with precipitation intensity ($r^2=0.1$). The poor correlation was possibly attributed to the small variation of SS_{med} within the range 0.05–0.20%. For observed 11 rain events in Okinawa, the median value of SS_{med} for all rain events was ranged from 0.09 % to 0.22% within the $0.05 < w_{\text{med}} < 0.5$ m/s range. The other observed and estimated parameter's values are summarized in Appendix 2A.

The relative contribution of three scavenging mechanisms of BC for each rain event in Figure 3.5(a). Figure 3.5(b) shows the average relative contribution of three scavenging mechanisms of BC within the $0.05 < w_{\text{med}} < 0.5$ m/s range. Figure 3.6 shows the average relative contribution of three scavenging mechanisms of BC (a) in Tokyo for 31 rain events and (b) in Okinawa for 11 rain events. The nucleation scavenging mechanism was dominant for BC-containing particles with $D_{\text{BC}} > 100$ nm, consistent with the result of Ohata et al. [2016b]. For $D_{\text{BC}} < 100$ nm, the relative contribution of impaction scavenging mechanisms increased because Brownian diffusion mechanism was dominant

in the cloud (Appendix A1). $\tilde{F}_{bc-imp}(D_{BC})$ for all rain events were negligibly small.

3.2.6 Key Parameter Controlling Nucleation Scavenging of BC

To specify the key parameter controlling the BC nucleation scavenging mechanism, this section focuses on the variation of the slope of $RE(D_{BC})$ within the $200 < D_{BC} < 400$ nm range in Figure 3.3 and Figure 3.4. The slope of $RE(D_{BC})$ within the range is represented as an indicator of the degree of wet removal efficiency of BC-containing particles scavenged by the nucleation mechanism. Figure 3.7 shows the relationship between the slope and the median SCr with $D_{BC} = 200$ nm. The slopes for $SCr > 1.2$ were nearly 0 in Tokyo and Okinawa, indicating that such thickly-coated BC particles were uniformly scavenged by nucleation mechanism. On the other hands, the slopes for $SCr < 1.1$ were largely variable within 1.22×10^{-3} - 12.1×10^{-3} range, independent of observation site.

To understand the variation of slope for SCr, the relationship between the slope and SCr with $D_{BC} = 200$ nm was theoretically estimated by using data analysis method, assuming SCr distribution, $\kappa_{BC-coat}$, and SS_{max} . The SCr distribution was assumed to be Gaussian distribution, which was similar to the observed size-resolved SCr distribution in Tokyo. The black shade in Figure 3.7 means the change of slope for $SS_{max} = 0.1\%$ when $\kappa_{BC-coat}$ is changed from 0.2 to 0.4. The red shade means the same but for $SS_{max} = 0.2\%$. For $SCr > 1.2$, theoretically-estimated slopes were scarcely variable and independent of $\kappa_{BC-coat}$ and SS_{max} , indicating that SCr was found to be the key parameter controlling the wet removal efficiency of BC. For $SCr < 1.1$, the variation of theoretically-estimated slopes was greatly large because the changes of CCN number fraction depending on SCr, $\kappa_{BC-coat}$, and SS_{max} caused the large variation of the wet removal efficiency of BC.

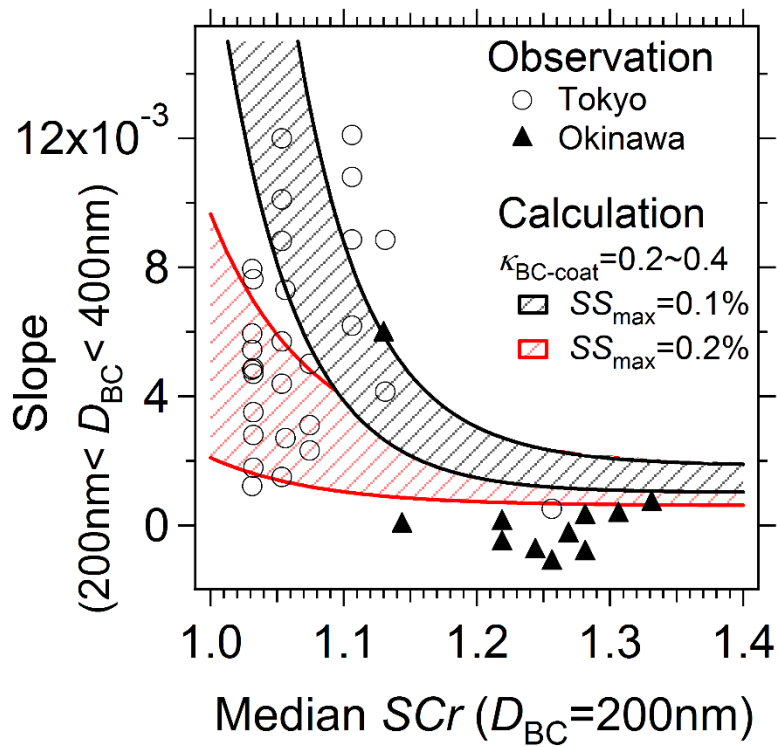


Figure 3.7. Relationship between the observed slope of removal efficiency in $200 < D_{BC} < 400$ nm range and the median shell/core ratio (SCr) with $D_{BC} = 200$ nm (marker). The relationship between the theoretically-estimated slopes and the median SCr with $D_{BC} = 200$ nm was also plotted (shade).

3.2.7 Estimated Transport Efficiency of BC

BC particles not scavenged by precipitation are transported to free troposphere (FT). To estimate how much BC particles are transported to the FT, the transport efficiency (TE_{cal} : the fraction of BC particles not scavenged by three-distinct mechanisms) within the $70 < D_{BC} < 2000$ nm range at Tokyo and Okinawa were calculated by using a parcel model in a precipitating cloud, based on the observation data. TE_{cal} for BC number concentration

is represented as the ratio of size-resolved number concentration of BC particles transported to FT ($N_{FT}(D_{BC})$) to $N_{air}(D_{BC})$. The $N_{FT}(D_{BC})$ was calculated by the product of the $N_{air}(D_{BC})$ and $\tilde{F}_{total}(D_{BC})$. Figure 3.8 shows (a) the SCr dependence of TE_{cal} for BC number concentration and (b) that of TE_{cal} for BC mass concentration. The estimate of TE_{cal} for median SCr < 1.1 was about 3-4 times higher than that of TE_{cal} for median SCr > 1.2 on average, indicating that the median SCr controls not only BC wet removal efficiency but also TE_{cal} .

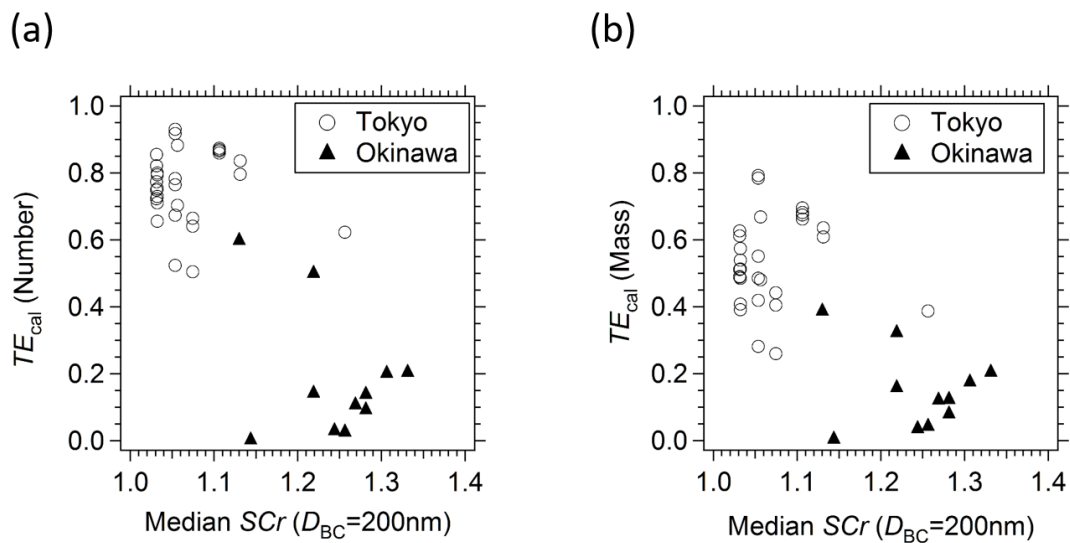


Figure 3.8. (a) Correlation between the transport efficiency (TE_{cal}) for BC number concentrations and median shell/core ratio (SCr) with $D_{BC} = 200\text{nm}$ in Tokyo and Okinawa, and (b) the same but for TE_{cal} for BC mass concentrations

Table 3.2. Average ($\pm 1\sigma$) transport efficiency (TE_{cal}) for BC number and mass concentrations in Tokyo and Okinawa.

TE_{cal}	Tokyo	Okinawa
BC number concentration	0.76 \pm 0.11	0.19 \pm 0.07
BC mass concentration	0.54 \pm 0.13	0.15 \pm 0.12

Figure 3.9 shows the average D_{BC} dependence of TE_{cal} for all rain events in Tokyo, and the average D_{BC} dependence of TE_{cal} within the $0.05 < w_{\text{med}} < 0.50$ m/s range in Okinawa. Smaller BC particles tended to be efficiently transported to FT in both sites. For $D_{\text{BC}} < 400$ nm in Okinawa, there was size-independent TE_{cal} and the TE_{cal} value was about 4 times smaller than in Tokyo (Table 3.2), indicating that thickly coated BC particles with $D_{\text{BC}} < 400$ nm were efficiently scavenged by precipitation. On the other hand, BC particles in Tokyo were efficiently transported to FT because the coating thickness of BC particles was very thin.

To verify the estimated D_{BC} dependence of TE_{cal} , it was compared with D_{BC} dependence of transport efficiency (TE_{obs}) obtained by direct measurement of an aircraft over East Asia [Moteki et al., 2012], which was the horizontally-averaged transport efficiency. The D_{BC} dependence of the TE_{obs} was similar to that of the TE_{cal} in Tokyo, indicating that D_{BC} dependence of the TE_{obs} arose from that of the F_{CCN} of BC.

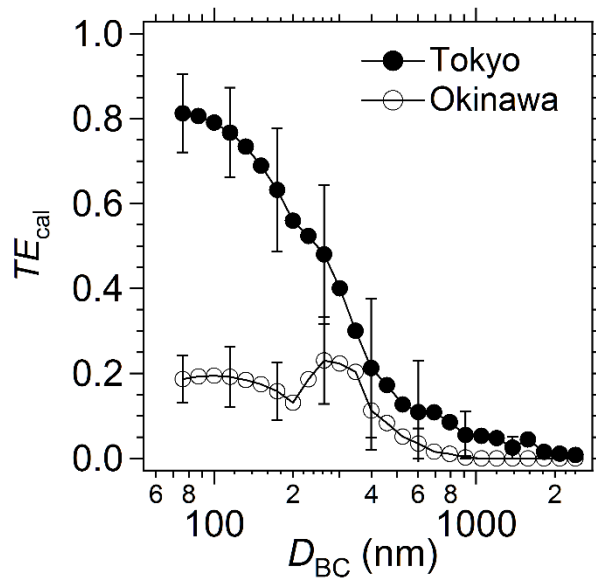


Figure 3.9. Size-dependent transport efficiency (TE_{cal}) in Tokyo and Okinawa (open and closed circle), calculated by the parcel model.

3.2.8 Understandings of BC Vertical Transport Using Aircraft Observation Data

To investigate that the relationship between directly observed mass median diameter of BC particle (MMD) at FT and transport efficiency (TE) is interpreted by the vertical transport of BC particles not scavenged by nucleation mechanism, the relationship between MMD and transport efficiency (TE_{ccn}) of BC particles not scavenged by nucleation mechanism is theoretically estimated by a parcel model. Figure 3.10 shows the observed correlation between the MMD and TE_{obs} over East Asia [Moteki et al., 2012]. The PBL-outflow air means the polluted outflow from China close to sea surface without wet deposition process, and the FT-clean air means the clean free tropospheric air. The median values for MMD in PBL-outflow and in FT-clean are also plotted with dotted lines in Figure 3.10. This observational result indicates that BC size shifted to lower size

by wet removal process. Figure 3.10 also shows the theoretically-estimated correlation between MMD and TE_{ccn} , assuming the initial BC number size distribution (CMD = 117.4nm, $\sigma_{gn} = 1.54$), the size-resolved SCr distribution, $\kappa_{BC-coat}$, and the distribution with SS_{med} . Red plot means the relationship for the thickly-coated BC particles and the blue plot means for thinly-coated BC particles. The SCr distribution was assumed to be Gaussian distributions with the median SCr = 1.30 and SCr = 1.06 for $D_{BC} = 200$ nm, respectively, which were close to the observation results in Okinawa and Tokyo. Theoretically, as the BC particles within the ascending air parcel experiences the moist convective process and high SS_{med} , the BC size at FT shifted to lower size because large BC particles are scavenged by nucleation mechanism. This trend is similar to the observational result, indicating that the observed relationship between MMD and TE is possibly interpreted by the vertical transport of BC particles not scavenged by nucleation mechanism. This results are very crucial to understand the mass concentration of BC particles transported to FT via moist convection process.

The transport efficiency (TE_{cal}) of BC particles not scavenged by three-distinct mechanisms was also estimated. Even if an ascending air parcel passed through a precipitating cloud during 2 hours, TE_{cal} was similar to TE_{ccn} , indicating that the TE was controlled by the nucleation scavenging mechanism.

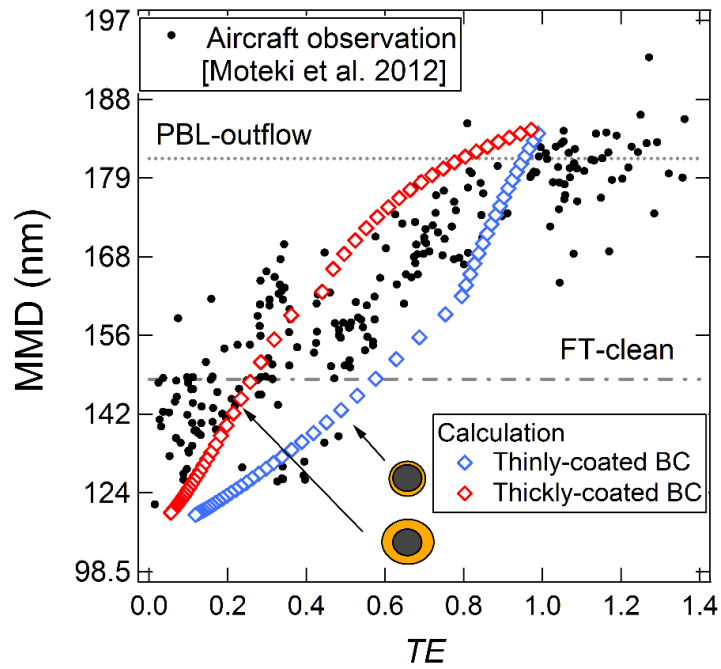


Figure 3.10. The correlation between MMD and TE_{obs} for 227 FT-outflow air parcels [Moteki et al., 2012] and the theoretically-estimated correlation between MMD and TE_{ccn} for thinly-coated (red marker) and thickly-coated (blue marker) BC particles.

3.2.9 Uncertainty in Estimates Using the Data Analysis Method

3.2.9.1 Uncertainty in Estimate of F_{CCN} , $F_{\text{bc(ic)-imp}}$, and TE_{cal}

This section describes the uncertainty in F_{CCN} , $F_{\text{bc(ic)-imp}}$, and TE_{cal} calculated by some physical parameters with uncertainty. Table 2.5 showed the uncertainties in physical parameters used in estimate of SCr. Due to these uncertainties, the changing rate of the volume of a BC-containing particle with $D_{\text{BC-shell}}$ was within uncertainty of $\pm 16\%$, corresponding to within the uncertainty of 4.0% for the SCr for $D_{\text{BC}}=100\text{nm}$. For $D_{\text{BC}}>400\text{nm}$, the uncertainty in the estimate of SCr was also negligibly small. Due to the

uncertainties in physical parameters used in calculation of F_{CCN} in Table 2.4(a), the uncertainty of F_{CCN} was estimated to be $\sim 9.0\%$ within $100 < D_{BC} < 2000$ nm range.

Table 2.4 (b) showed the uncertainties in some physical parameters for calculating $F_{bc(ic)-imp}$. Due to the uncertainty in BC density and the variation of temperature in air, the $K(D_{BC}, D_d)$ was within uncertainty of 4.2% in Table A1.1. $F_{bc(ic)-imp}(D_{BC})$ was also estimated to be within the uncertainty of 4.2% , indicating that the uncertainty in estimate of $F_{bc(ic)-imp}(D_{BC})$ for the same w and t was negligibly small.

Due to the above factors, the uncertainty in estimate of TE_{cal} was $\sim 10\%$ within $70 < D_{BC} < 2000$ nm range. The uncertainty in relative contribution of three-distinct scavenging mechanisms was also estimated to be $\sim 10\%$.

3.2.9.2 Uncertainty in Estimate of TE_{cal} due to Distribution of Updraft Velocity

The dissertation assumed that the distribution width of updraft velocity was the width of Gaussian distribution with the relationship between average w and standard deviation by the aircraft observation [Fountoukis et al., 2007]. To investigate if the distribution width is insensitive to the estimate of TE_{cal} , this section estimates the uncertainty in TE_{cal} due to the distribution of updraft velocity. During observation period, the width of Gaussian distribution with w_{med} was estimated to be within $0.1\text{--}0.3$ m/s range. When the width of Gaussian distribution with typical w_{med} ($=0.1\text{m/s}$) was variable within the $0.1\text{--}0.3$ m/s range, the uncertainties in estimate of TE_{cal} were $\sim 10\%$, indicating that assumption of the width of the distribution had little effect on our results.

3.2.9.3 Uncertainty in Estimate of F_{CCN} for BC-containing Particles with Organic Compounds

This dissertation estimated the SCr for $70 < D_{BC} < 200 \text{ nm}$ and $400 < D_{BC} < 2000 \text{ nm}$ range, assuming that the sulfate in the atmosphere condensed on a BC particle. However, the dominant chemical composition in Tokyo was not sulfate but organic, so that it is necessary to evaluate the uncertainty in the estimate of SCr in Tokyo when the volatile organic compounds (VOC) condense on a BC particle. The SCr was estimated by using toluene, which was the one of the highest concentrations in VOCs in Tokyo during 2003-2004 [Hoshi et al., 2007]. Compared with the SCr estimated by using the sulfate in Figure 3.2, the estimates of SCr for BC-containing particles with the organic compounds changed little. The uncertainty in F_{CCN} for BC-containing particles with organic compounds was estimated to be $\sim 9.0\%$.

3.3 Summary

For exploring the detailed physical mechanisms by which the efficiency of BC wet removal is actually controlled in precipitating clouds, a novel ground-based observation was conducted at different observation sites; the University of Tokyo and Cape Hedo in Okinawa. For each rain event, the relative contribution of three-district (below-cloud impaction, nucleation, and in-cloud impaction) scavenging mechanism was investigated by using the cloud parcel model, based on the observation data and the measured D_{BC} dependence of wet removal efficiency.

D_{BC} dependences of $RE(D_{BC})$ was observed in Tokyo and Okinawa, where fresh and aged pollutions are dominant. The majority of BC-containing particles in Tokyo were thinly coated ($SCr < \sim 1.1$ for $D_{BC} = 200 \text{ nm}$), while those of BC-containing particles in Okinawa were thickly coated ($SCr > \sim 1.2$ for $D_{BC} = 200 \text{ nm}$). The observed D_{BC} dependences of $RE(D_{BC})$ were clearly different in Tokyo and Okinawa. The large BC

particles were more efficiently removed by precipitation in Tokyo, while BC particles were uniformly removed by precipitation in the $70 < D_{BC} < 457$ nm range.

The relative contribution of three-district scavenging mechanisms was investigated by using the data analysis method. The dissertation revealed that for $D_{BC} > 100$ nm, nucleation scavenging mechanism was the key mechanism by which the efficiency of BC wet removal was actually controlled in precipitating clouds. For $D_{BC} < 100$ nm, the contribution of impaction scavenging mechanism (mainly due to Brownian diffusion) was similar to that of nucleation scavenging mechanism. These results were independent of the observation site. The data analysis method also provides the estimates of updraft velocity and maximum supersaturation. The median values (25th percentile, 75th percentile) of updraft velocity and maximum supersaturation in Tokyo were estimated to be 0.10 (0.05, 0.23) m/s and 0.11 (0.07, 0.18) %, which were reasonable values. In Okinawa, the median value of maximum supersaturation was ranged from 0.09 % to 0.22 % within the updraft velocity 0.05-0.5 m/s range.

This dissertation also revealed that the SCr was a key parameter controlling the nucleation scavenging mechanism and transport efficiency of BC by using the data analysis method. For the $SCr > 1.2$, the wet removal efficiency of BC was nearly unity, independent of hygroscopicity and maximum supersaturation, while for the $SCr < 1.1$, the wet removal efficiency of BC strongly depended on the SCr , hygroscopicity, and maximum supersaturation. Thus, BC-containing particles with $SCr > 1.2$ were efficiently scavenged by nucleation mechanism, while BC-containing particles with $SCr < 1.1$ were efficiently transported to free troposphere. Moreover, SCr also controlled D_{BC} dependence of transport efficiency because the D_{BC} dependence of wet removal efficiency (: slope) strongly depended on SCr . By comparing the aircraft observation data, this

dissertation revealed that the vertical transport of BC particles not scavenged by nucleation mechanism was very crucial to understand the BC mass concentration in free troposphere.

4. General Conclusions

In this dissertation, a novel ground-based observational approach was used to explore the detailed physical mechanisms by which the efficiency of BC wet removal is controlled in precipitating clouds. In each precipitation event, the relative contributions of three distinct BC scavenging mechanisms were inferred, on the basis of the measured particle-size dependence of wet removal efficiency.

The observational approach was realized on the basis of several newly developed methodologies. First, an accurate experimental method was developed for measuring the size-resolved number concentration of BC suspended in water for a particle-size range of 70–2000 nm (Chapter 2.1). This method enabled the determination of the size-dependent wet removal efficiency of BC-containing aerosols by comparing the measured size distributions of BC in rainwater (after removal) and in ambient air (before removal). Second, this work provides experimental evidences that the size distribution of BC particles suspended in water is invariant during cloud-precipitation processes and during storage of rainwater samples (Chapter 2.1). Third, a new data-analysis method was developed to infer the relative contributions of three distinct BC scavenging mechanisms in a precipitating cloud, under constraints from the measured size-dependent BC wet removal efficiency and other observational data (e.g., BC mixing state, size-distribution of rain droplets and so on) (Chapter 2.2).

The developed observational approach was applied to two ground-observation campaigns conducted one in Tokyo and the other in Okinawa, where fresh and aged pollutants, respectively, are dominant. Reflecting the difference in aging, the majority of BC-containing particles in Tokyo were found to have only a small amount of coating (SCr

$< \sim 1.1$ for $D_{BC} = 200$ nm), whereas those in Okinawa had much larger amount (SCr $> \sim 1.2$ for $D_{BC} = 200$ nm).

The measured size-dependent BC wet removal efficiency $RE(D_{BC})$ varied remarkably among precipitation events. The $RE(D_{BC})$ often increased steeply with D_{BC} in Tokyo, but it seldom showed such D_{BC} dependence in Okinawa (see Figure 3.3). From data of 42 rain events (31 events in Tokyo and 11 events in Okinawa), we found that the remarkable size-dependence of $RE(D_{BC})$ (e.g., slope $> 2e^{-3}$) appeared only in rain events when BC-containing particles in air had a small amount of coating materials (see Figure 3.7).

In each rain event, the relative contributions of three distinct BC-scavenging mechanisms (nucleation, cloud-droplet impaction, and rain-droplet impaction) were inferred using the data analysis method described in Chapter 2.2. From the results, I concluded that nucleation scavenging is almost always dominant for BC-containing particles with $D_{BC} > 100$ nm, whereas the contribution of cloud-droplet impaction (mainly due to Brownian coagulation) can be dominant for particles with $D_{BC} < 100$ nm. The data analysis method also provides an estimate of the updraft velocity and maximum supersaturation experienced by the removed BC-containing particles. The median (25th percentile, 75th percentile) values of updraft velocity and maximum supersaturation in Tokyo were estimated to be 0.10 (0.05, 0.23) m/s and 0.11 (0.07, 0.18) %, respectively. In Okinawa, the median values of maximum supersaturation in air ranged from 0.09% to 0.22% within the updraft velocity range of 0.05–0.5m/s. These estimates are reasonably similar to reported values for cumulus clouds.

The results confirm that nucleation scavenging is almost always the dominant scavenging mechanism responsible for removal of BC mass concentrations in air because

BC mass concentration in ambient air is mainly in $100 \text{ nm} < D_{\text{BC}} < 1000 \text{ nm}$, wherein the relative contribution of nucleation scavenging is substantially greater than that of other scavenging mechanisms (Figures 3.5, 3.6). This finding is qualitatively consistent with assumptions adopted in current 3D atmospheric aerosol models.

The results have detailed implications that are useful for further model improvements as follows. The slope of $RE(D_{\text{BC}})$ (Figure 3.7) and the estimated transport efficiency (Figure 3.8) abruptly decreased when the amount of coating materials on BC exceeded a threshold value. Results showed that the threshold coating amount corresponded to a median $\text{SCr} = \sim 1.2$ ($D_{\text{BC}} = 200 \text{ nm}$). For rain events with a median $\text{SCr} < 1.1$, the slope of $RE(D_{\text{BC}})$ showed a larger variation, which was explained by the change in the CCN number fraction, depending on the maximum supersaturation and the hygroscopicity of the coating materials. For all rain events with a median $\text{SCr} > 1.2$, the slope of $RE(D_{\text{BC}})$ was almost always zero, which implies that BC-containing particles are efficiently removed for any D_{BC} , and are therefore almost insensitive to the maximum supersaturation and the hygroscopicity of coating materials.

Thus, for moderately aged plumes wherein the median $\text{SCr} > 1.2$ (for $D_{\text{BC}} = 200 \text{ nm}$), even if all BC-containing particles in an air parcel are assumed to be unconditionally removed when the parcel experiences precipitating moist convection, the approximation will be good. By contrast, for relatively fresh plumes wherein the median $\text{SCr} < 1.1$ (for $D_{\text{BC}} = 200 \text{ nm}$), the wet removal efficiency of BC-containing particles in an air parcel changes by depending on the coating amount, hygroscopicity of coating, and maximum supersaturation.

For future numerical simulations of BC wet removal by 3D atmospheric aerosol models, our results suggest that higher computational resolutions of chemical

composition and amount of coating materials are important for fresh plumes that correspond to a median $SCr < 1.1$ (for $D_{BC} = 200\text{nm}$). For example, it may be a good idea to concentrate computational efforts for aerosol microphysics only within several hundred km of urban areas.

For future numerical simulation of wet removal of aerosol particles by 3D atmospheric aerosol models, the wet removal parameterization scheme considering a critical supersaturation (Sc) of aerosol particles is very useful to make the accurate estimate of spatial and temporal distributions of aerosol particles. The Sc of BC-containing particles with $SCr = 1.2$ (for $D_{BC} = 200\text{nm}$) and average hygroscopicity of coating materials ($= 0.3$) was about 0.1 in this dissertation. The result indicates that BC-containing particles with $Sc < 0.1\%$ are unconditionally removed, whereas the wet removal of BC-containing particles with $Sc > 0.1\%$ depends on the chemical composition of coating materials, amount of coating materials, and maximum supersaturation in air. To make the accurate estimate of spatial and temporal distributions of aerosol mass concentrations, our results suggest that it is important to improve the resolution of $Sc > 0.1\%$ and the maximum supersaturation $> 0.1\%$ in 3D atmospheric aerosol models. By improving the treatment of the aerosol wet removal in the 3D models, uncertainties in estimate of radiative forcing of aerosols will decrease.

Finally, the observational future work arising from this study is discussed. The results presented in this dissertation reveal that, in precipitating clouds at mid-latitudes, BC-containing particles with $D_{BC} > 100\text{ nm}$ were scavenged by nucleation mechanism and the wet removal efficiency of BC was strongly sensitive to the amount of coating material. To investigate whether the results are representative of precipitating clouds in general, the simultaneous measurements of BC size-resolved number concentrations in

air and rainwater at low and high latitudes, such as tropical and polar regions, are crucial. Expanding the findings will improve our quantitative understanding of wet removal of BC in precipitating clouds. Quantitative understanding of wet removal of BC in snow clouds was poor in this dissertation. To understand the wet removal of BC in the clouds, it is necessary to make a simultaneous measurement of BC size-resolved number concentrations in air and snow in a snowfall region. The new observational approach presented here should also improve the quantitative understanding of the key mechanism and parameter controlling the wet removal efficiency of BC in the snow clouds. These observational approaches enable the accurate estimate of BC spatial and temporal distributions and the decrease of uncertainties in the estimate of BC radiative forcing.

The measurement method consisting of Marin-5 nebulizer and SP2 is available for not only BC particles suspended in rain and snow but also BC particles in ice-core and sedimentation. The analysis of BC in ice-core and sedimentation samples improves the quantitative understanding of the variation of BC mass concentration over a few hundred years and that of the effect on the climate change. Measurements of BC wet deposition fluxes are also important to evaluate the global model's performance.

Smaller BC particles were estimated to be efficiently transported to the free troposphere by a parcel model in this study. To verify the D_{BC} -dependence of transport efficiency, direct measurement of transport efficiency of BC is important. For example, the measurement of size-resolved number concentrations of BC in air at the top (: free troposphere) and foot (: ground) of a high mountain, such as Mt. Fuji in Japan, would be very useful. The direct measurement of transport efficiency of BC particles would improve our quantitative understanding of the spatial and temporal distributions of BC in local moist convection.

Appendix

Appendix A1. Data-Processing Procedure for Calculating the Scavenged Number Fractions of BC

Appendix A1 describes the detail data-processing procedure for calculating the number fractions of BC particles scavenged by below-cloud impaction ($F_{bc-imp}(D_{BC})$), nucleation ($F_{cnn}(D_{BC})$), and in-cloud impaction ($F_{ic-imp}(D_{BC})$) mechanisms. These data-processing procedures are shown in Figure A1.1.

A1.1. Detailed calculation method of F_{bc-imp} and F_{ic-imp}

Before an air parcel ascends to cloud base, a number fraction of BC particles is mainly scavenged by Brownian diffusion, interception, and inertial impaction mechanisms [Wang et al., 2010]. To calculate the $F_{bc(ic)-imp}(D_{BC})$, it is important to calculate a size-dependent collection efficiency for each attachment process. In the calculation, a BC size is defined as an aerodynamic diameter (D_a), which is the diameter of a spherical particle with a density of 1.0 g/cc, because BC particle moves along an air streamline.

The collection efficiency ($CEF(D_a, D_d)$) depends on the BC size and droplet size (D_d), which was proportional to collection kernel ($K(D_a, D_d)$);

$$CEF(D_a, D_d) = \frac{4}{ReSc} [1 + 0.4Re^{1/2} + Sc^{1/3} + 0.16Re^{1/2} + Sc^{1/2}] + 4 \frac{D_a}{D_d} \left[\frac{\mu_{air}}{\mu_w} + (1 + 2Re^{1/2}) \frac{D_a}{D_d} \right] + \left(\frac{St - St^*}{St - St^* + 2/3} \right)^{3/2} \left(\frac{\rho_{BC}}{\rho_w} \right)^{1/2}, \quad (A1)$$

where

$$Re = \frac{D_d V(D_d) \rho_{\text{air}}}{2\mu_{\text{air}}}, \quad Sc = \frac{\mu_{\text{air}}}{\rho_{\text{air}} D_{\text{diff}}}, \quad D_{\text{diff}} = \frac{k_b T_{\text{air}} C_c}{3\pi\mu_{\text{air}} D_a}$$

$$St = \frac{2\tau(V(D_d) - v(D_a))}{D_d}, \quad \tau = \frac{(\rho_{\text{BC}} - \rho_{\text{air}}) D_a^2 C_c}{18\mu_{\text{air}}}$$

$$St^* = \frac{1.2 + \frac{1}{12} \ln(1 + Re)}{1 + \ln(1 + Re)}, \quad C_c = 1 + \frac{2\lambda}{D_a} \left(1.257 + 0.4 \exp\left(-0.55 \frac{D_a}{\lambda}\right) \right).$$

All symbols and uncertainties are shown in Table A1.1. The first term of equation (A1) represents Brownian diffusion, the second term represents interception, and the third term represents inertial impaction. Interception mechanism is similar to inertial impaction mechanism, but the interception strongly depends on the size and shape [Seinfeld and Pandis, 2006]. Therefore, the $K(D_a, D_d)$ for interception mechanism was calculated by using D_a derived from the relationship between the maximum length of BC particles measured with transmission electron microscopy (TEM) and the mobility diameter of BC particles [Park et al., 2004]. On the other hand, inertial impaction mechanism depends on the mass. The $K(D_a, D_d)$ for Brownian diffusion and inertial impaction mechanism was calculated by using the relationship between D_a and D_{BC} , defined by DeCarol et al [2004].

Figure A1.2 shows the CEF of a spherical and non-spherical (BC) particle for a raindrop with $D_d = 1.0$ mm. The D_{BC} dependences of CEF for a spherical particle and a non-spherical particle were largely different, and CEF for a non-spherical particle at $D_{\text{BC}} = 1.0$ μm was about 10 times larger than that for a spherical particle, indicating that the shape of the BC particle strongly controlled the CEF . Using the D_{BC} -dependence of CEF

for the non-spherical particle and droplet (rain drop or cloud droplet) number concentration $N_d(D_d)$, scavenging ratio $\Lambda(D_a)$ was calculated in equation (2.18). Thereafter, $F_{bc-imp}(D_a)$ is calculated by using the $\Lambda(D_a)$ and the time (t) at which the air parcel reaches to cloud base in equation (2.20). Finally, $F_{bc-imp}(D_{BC})$ is obtained by changing from D_a to D_{BC} .

For in-cloud impaction scavenging mechanism, the *CEF* of the Brownian diffusion mechanism is dominant and the contribution of other mechanisms is negligibly small. Thereafter, $F_{ic-imp}(D_a)$ is calculated by using $\Lambda(D_a)$ and the residence time (t) in the precipitating cloud. Finally, $F_{ic-imp}(D_{BC})$ for each t is calculated by changing from D_a to D_{BC} .

Due to the uncertainty in BC density and the variation of temperature, the uncertainty in CEF of BC particles was within 4.2%

Table A1.1. All symbols used in calculation of collection efficiency. Uncertainties and references are also shown.

	Symbols	Descriptions	Uncertainty and Reference
Known values	μ_{air}	Air viscosity (= $1.81 \times 10^{-5} \text{ kg m}^{-1} \text{ s}^{-1}$)	[Seingeld and Pandis. 2006]
	μ_{w}	Water viscosity (= $0.90 \times 10^{-3} \text{ kg m}^{-1} \text{ s}^{-1}$)	[Seingeld and Pandis. 2006]
	ρ_{BC}	BC density (= 1.8 g cm^{-3})	5.0 % [Moteki et al.2010]
	ρ_{air}	Air density (= 1.21 kg/m^3)	
	ρ_{w}	Water density (= 1.0 g/cc)	
	k_{b}	Boltzmann constant (= $1.38 \times 10^{-23} \text{ J K}^{-1}$)	
	T_{air}	Air temperature (= 298K)	2.0%
	λ	Mean free path of air molecule at 298 K (= $65.1 \times 10^{-9} \text{ m}$)	[Seingeld and Pandis. 2006]
Calculation	Re	Raindrop Reynolds number	
	Sc	Particle Schmidt number	
	D_{diff}	Particle Brownian diffusivity coefficient	
	St	Particle Stokes number	
	St^*	Critical Stokes number of particle	
	τ	Relaxation time of particle	
	Cc	Cunningham correction factor	
	V	Raindrop terminal velocity	
	v	Particle terminal velocity	
	CEF	Droplet-particle collection efficiency	4.2%

A1.2. Detailed calculation method of F_{ccn}

Critical supersaturation (Sc) is calculated by using a SCr and a hygroscopicity of BC-containing particles (κ) within 1h before precipitation began for each rain event. Figure A1.3(a) shows the boxplot of the SCr distributions for the $70 < D_{\text{BC}} < 2000\text{nm}$ range (Observed SCr range; 200-400nm, Estimated SCr range; 70-200 nm and 400-2000 nm) in Tokyo on Aug 12, 2014 and in Okinawa on Mar 9, 2016. Figure A1.3(b) also shows the boxplot of Sc distributions calculated by using the SCr distribution and κ for BC-containing particle. These boxplots show the 10th, 25th, 50th, 75th, and 90th. The median value of Sc distribution in Okinawa was smaller than that of Sc distribution in Tokyo, indicating that BC-containing particles in Okinawa are more active as CCN even if SS_{max} is relatively small. By comparing the Sc distribution and SS_{max} distribution, the activated number concentrations of BC particles ($N_{\text{ccn}}(D_{\text{BC}})$) were calculated by using the κ -Kohler theory. $F_{\text{ccn}}(D_{\text{BC}})$ is represented as the ratio of $N_{\text{ccn}}(D_{\text{BC}})$ to the total number concentration of BC ($N_{\text{cn}}(D_{\text{BC}})$). N_{cn} means the number concentrations of BC particles not scavenged by below-cloud impaction mechanism. This calculation assumes that the observed $\kappa_{\text{BC-coat}}$ is independent of D_{BC} because the hygroscopic growth factor, which is a function of κ , is largely independent of the dry mobility diameter larger than 100nm [Mochida et al., 2010].

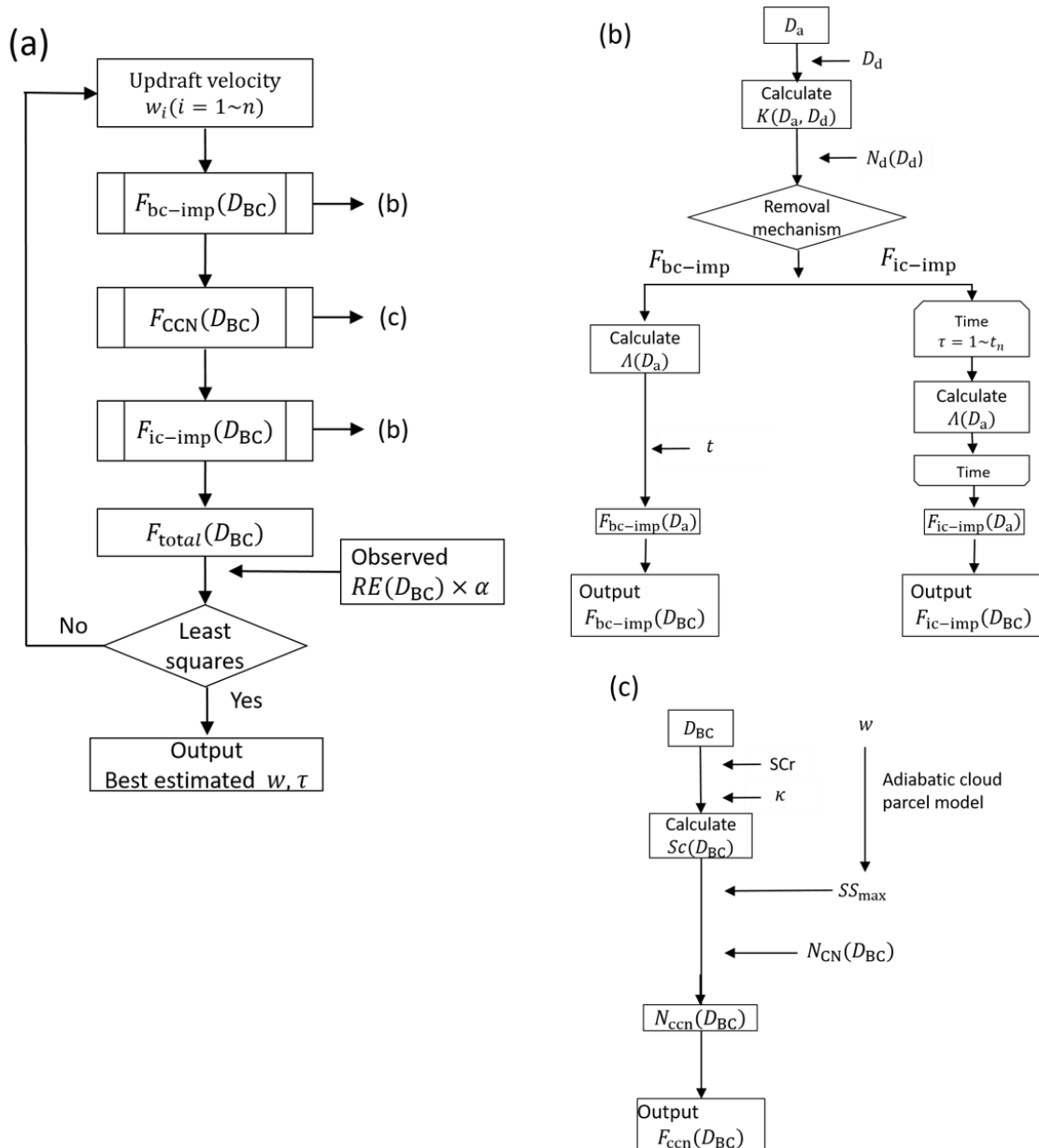


Figure A1.1 (a) Data-processing procedure for determining the updraft velocity (w) and residence time (t). (b), (c) Data-processing procedure for calculating the number fractions of BC-containing particles scavenged by below-cloud impaction ($F_{bc-imp}(D_{BC})$), nucleation ($F_{CCN}(D_{BC})$), and in-cloud impaction ($F_{ic-imp}(D_{BC})$) mechanisms. It notes that w and t are assuming parameters. Parameter α is a constant value to fit the observed D_{BC} of $RE(D_{BC})$ to the calculated size dependence of $F_{total}(D_{BC})$.

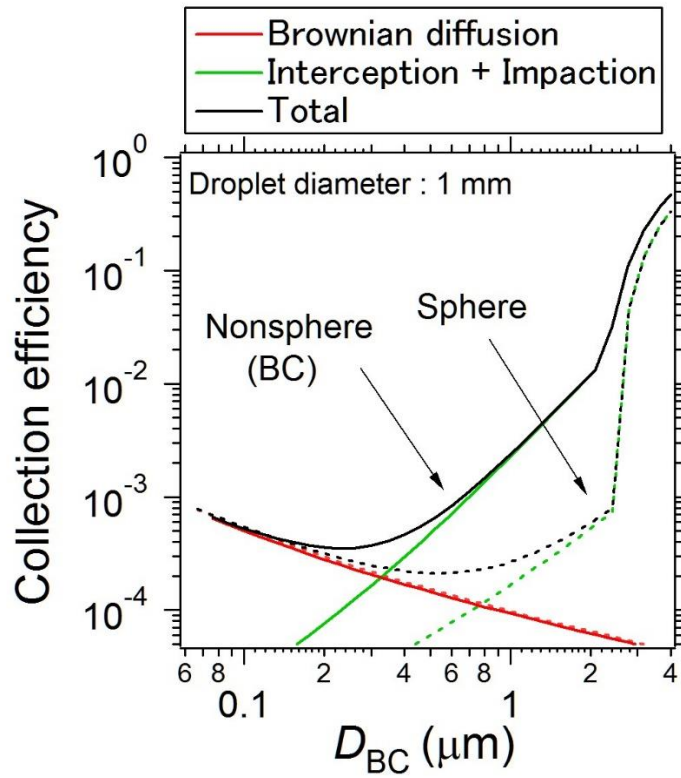


Figure A1.2. Size-resolved collection efficiency of a spherical and non-spherical (BC) particle for each attachment mechanism for droplet diameter $D_d = 1\text{ mm}$, which are represented as the dotted and bold line, respectively.

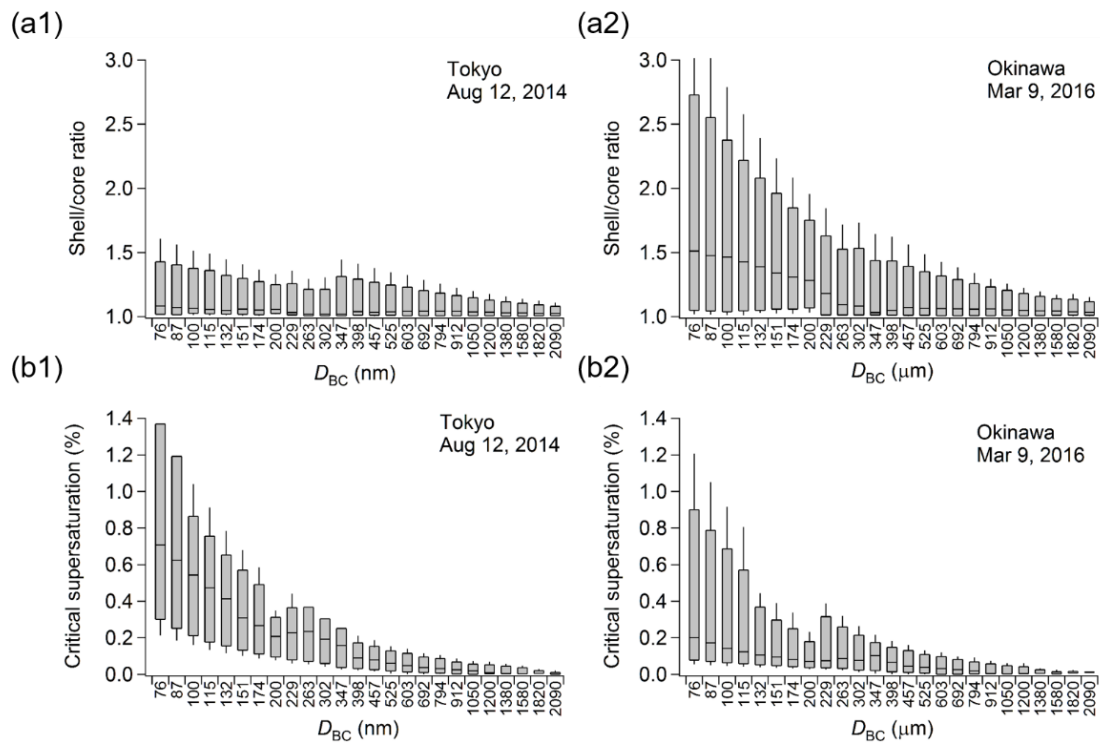


Figure A1.3. (a) Size-resolved shell/core ratio (SCr) distribution and (b) size-resolved critical supersaturation distribution on Aug 12, 2014 in Tokyo and on Mar 9, 2016 in Okinawa within the $70 < D_{BC} < 2090$ nm range (observed range: $200 < D_{BC} < 400$ nm range, estimated range: $70 < D_{BC} < 200$ nm and $400 < D_{BC} < 2090$ nm). The boxplot shows the 10th, 25th, 50th, 75th, and 90th.

Appendix A2. Observed and Estimated values in Tokyo and Okinawa

Table A2. The median values (25th percentile, 75th percentile) of observed average precipitation intensity (P), aerosol number concentrations (N_a), raindrop number concentrations (N_{d_rain}), median shell/core ratio (SCr) with $D_{BC} = 200$ nm, and hygroscopicity of BC-containing particles in Tokyo and Okinawa. The median values of w_{med} , SS_{med} , cloud droplet number concentrations (N_{d_cloud}), the residence time in PBL (T_{med}), and residence time in a precipitating cloud (t_{med}) are also shown in Tokyo. In Okinawa, these average values within $0.05 < w_{med} < 0.5$ m/s range are shown.

	Parameter	Tokyo	Okinawa
Observation	P [mm/h]	5.62 (2.81, 8.76)	3.07 (1.1, 6.27)
	N_a [#/cc]	3203 (2423, 5638)	1213 (1029, 1354)
	N_{d_rain} [10^{-3} #/cc]	4.34 (2.93, 7.41)	2.82 (2.04, 4.40)
	SCr ($D_{BC}=200$ nm)	1.05 (1.03, 1.07)	1.26 (1.22, 1.28)
	$\kappa_{BC-coat}$	0.26 (0.22, 0.26)	0.38 (0.36, 0.43)
Estimates	w_{med} [m/s]	0.10 (0.05, 0.23)	0.05–0.5
	SS_{med} [%]	0.11 (0.07, 0.18)	0.09–0.22
	N_{d_cloud} [#/cc]	382 (274, 446)	240–438
	T_{med} (Rain) [s]	10000 (4583, 20000)	2000–20000
	t_{med} (Cloud) [s]	4000 (2000, 4000)	12000–50000

Appendix A3. Wet Deposition of Black Carbon at a Remote Site in the East China Sea

This section is the content of Mori et al. [2014]. This purpose is to understand the temporal and spatial variations of BC mass concentrations at a remote site downstream from China by measuring BC mass concentrations in air and rainwater, and wet deposition fluxes of BC for 3 years at Cape Hedo on Okinawa Island.

A3.1 Introduction

BC mass concentrations in air (M_{BC}) and in rainwater (C_{BC}), and BC wet deposition flux (F_{BC}) have often been obtained at several locations in the United States and Europe, using the TOT technique [Ogren et al., 1984; Dasch and Cadle, 1989; Ducret and Cachier, 1992; Armalis, 1999; Chýlek et al., 1999; Hadley et al., 2008; Cerqueira et al., 2010]. Ogren et al. [1984] measured M_{BC} , C_{BC} , and F_{BC} for 7 weeks in Seattle and for 5 months in Sweden. Ducret and Cachier [1992] measured M_{BC} and C_{BC} in Paris for 2 years and at a rural site in Ireland for about 2 months. They found that BC was removed more efficiently in Ireland than in Paris by comparing the C_{BC}/M_{BC} ratios measured at both sites. It was speculated that the difference in the C_{BC}/M_{BC} ratios might have been caused by the possible difference in hygroscopicity of BC at the two sites. Armailis et al. [1999] measured F_{BC} at eight sites in rural Lithuania for 1–3 years. They found a maximum F_{BC} in winter in association with maxima in M_{BC} and C_{BC} . Cerqueira et al. [2010] obtained F_{BC} at five sampling sites in western and eastern Europe for a few years. However, these C_{BC} and F_{BC} observations were not analyzed with consideration of transport of BC from major sources (e.g., East Asia).

To improve understanding of the temporal and spatial variations of C_{BC} and F_{BC} , the measurements of BC in rainwater at a remote site downstream from China were made. For this purpose, a single-particle soot photometer (SP2) was used, which is a recently established technique for accurate C_{BC} measurement that requires much smaller amounts of rainwater than the TOT technique. Simultaneous observations of M_{BC} , C_{BC} , and F_{BC} for 3 years were conducted at Cape Hedo on Okinawa Island, Japan, in the East China Sea, an optimal site for estimating deposition flux of BC transported from the Asian continent. This Appendix A3 provides technical descriptions of the measurements followed by the observational results and their interpretation. Finally, causal relationships between C_{BC} , M_{BC} , and meteorological parameters from the results of a thermodynamic model were also reported.

A3.2 Measurements

A3.2.1 Characteristic of Observation Site

The measurements of M_{BC} and collections of rainwater were conducted from April 2010 to March 2013 at Cape Hedo on Okinawa Island (26.87°N, 128.26°E) in the East China Sea. A part of this site was described in Chapter 3. Figure A3.1 shows the maps of BC emission rate, column BC mass concentration, precipitation rate, and BC wet deposition flux in East Asia averaged from March to May 2010, as calculated by the Community Multiscale Air Quality (CMAQ) model with the Process, Age, and Source Region Chasing Algorithm (PASCAL) regional scale model [Matsui and Koike, 2012; Matsui et al., 2013]. During this period, BC emissions were highest in North China (33–50°N, 100–130°E) and were reflected in the high BC column mass concentrations in that region (Figure A3.1b). However, wet deposition flux of BC over the Asian continent was highest in South China (20–33°N, 100–123°E) (Figure A3.1d) due to the much higher precipitation there (Figure A3.1c). As discussed in section A3.3.4 in detail, the majority of BC emitted in North China was removed downstream rather than locally. The figure also shows that column BC mass concentrations and wet deposition fluxes were rather uniform near Hedo, suggesting that the measurements of BC wet deposition at Hedo are representative of that region.

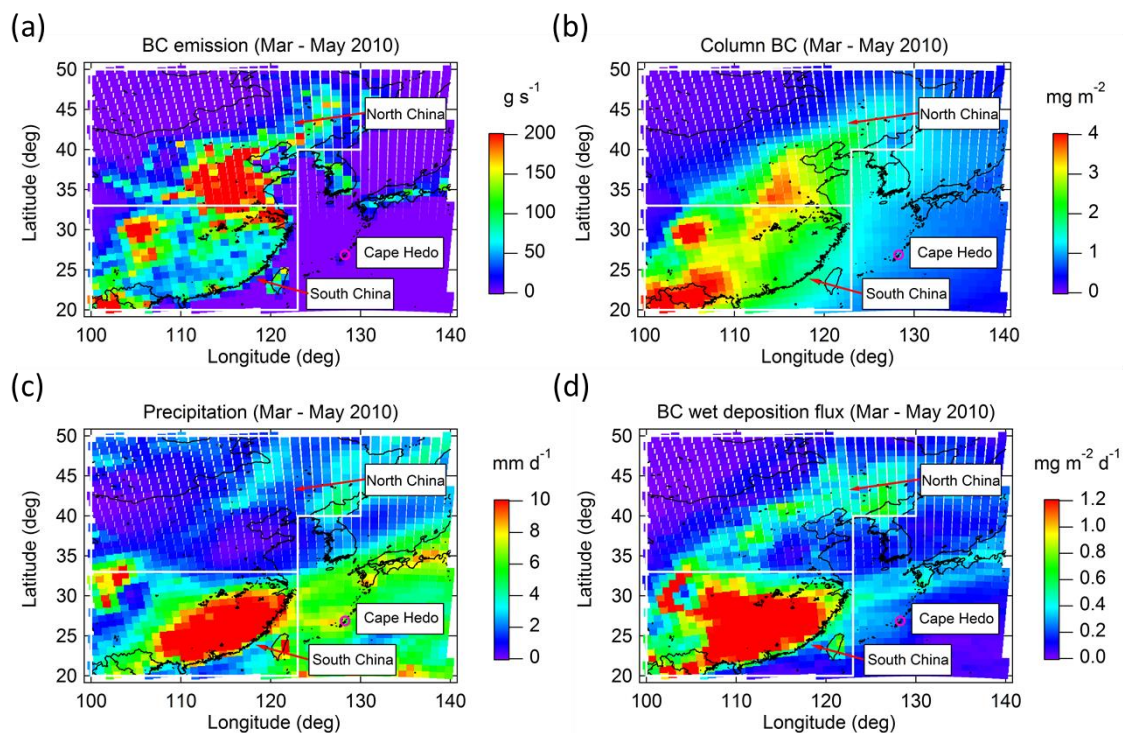


Figure A3.1. Maps of (a) anthropogenic BC emissions, (b) column BC in the air, (c) precipitation, and (d) BC wet deposition flux over East Asia for March–May 2010, as calculated with the CMAQ-PASCAL model [Matsui et al., 2013].

A3.2.2. BC in Air

BC mass concentrations in the fine mode (particles with aerodynamic diameters smaller than $1 \mu\text{m}$) were measured with an integration time of 1 min using a filter-based absorption photometer, the continuous soot monitoring system (COSMOS), with an inlet heated to $400 \text{ }^\circ\text{C}$ [Miyazaki et al., 2008; Kondo et al., 2009, 2011b]. The instrument monitor changes in transmittance across an automatically advancing quartz fiber filter

tape at a wavelength of 565 nm. The changes in transmittance are converted to BC mass concentrations using the mass absorption cross section determined by comparison with measurements by the SP2 instrument and TOT technique [Kondo et al., 2009, 2011b]. The BC mass concentrations are given in the units of mass and volume per unit volume of air at standard temperature and pressure (273.15 K and 1013 hPa). The accuracy of the COSMOS has been estimated to be about 10% with a detection limit of $0.015 \mu\text{g m}^{-3}$ for a 10 min integration time [Kondo et al., 2009; 2011b]. The 1 h average BC data for the present analysis was used.

A3.2.3. BC in Rainwater

Rainwater sampling at Hedo was performed with an automated wet-only sampler (US-420, Ogasawara Keiki Seisakusho Co., Ltd.; schematic diagram in Figure A3.2a and detailed descriptions of this sampler are given in Appendix A4.1, which is abbreviated as automated sampler from now. In brief, rainwater collected during A34 h period starting at 0900 Japan Standard Time (JST) was passed through a Teflon tube into a polypropylene bottle (1 L). After collection, each bottle was automatically stored in a refrigerator at 5 °C for up to 2 weeks. A portion of the water in each bottle was transferred into small glass bottles, which were shipped to the University of Tokyo and refrigerated at 5 °C until BC analysis.

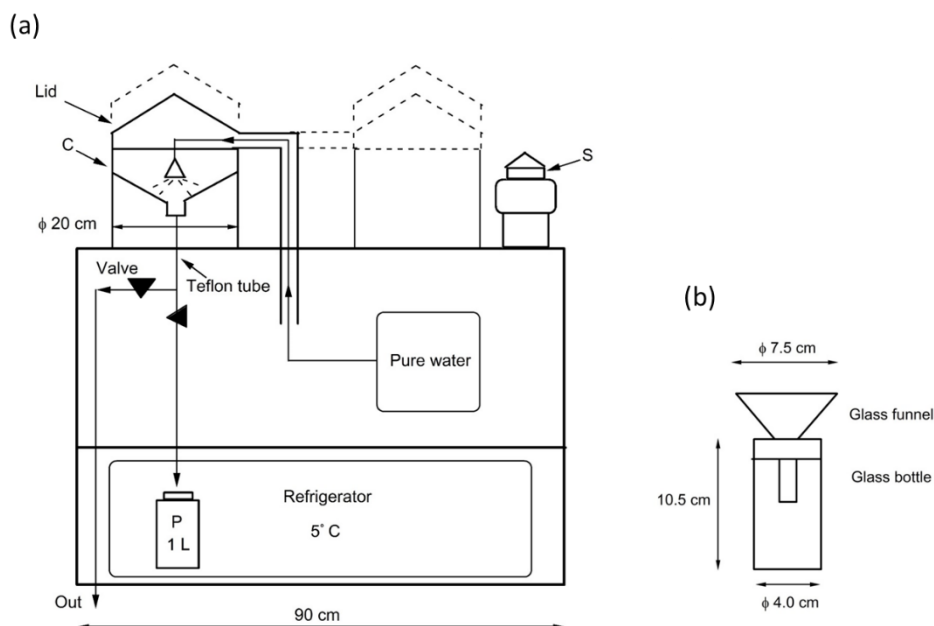


Figure A3.2. Schematic diagram of rainwater samplers. (a) In the automated wet-only sampler, rain from the rainwater collector (*C*) is poured into a 1 L polypropylene bottle (*P*) through a Teflon tube and stored in the refrigerator at 5°C. The collector lid is opened when the rain sensor (*S*) detects precipitation. The funnel is routinely washed to remove dry deposition.

(b) In the manual sampler, a glass funnel is inserted into the lid of a glass bottle.

C_{BC} ($\mu\text{g L}^{-1}$) was measured in each collected rainwater sample with a system based on an ultrasonic nebulizer (U-5000AT, Cetac Technologies Inc., Omaha, Nebraska, USA) and a measurement technique described in detail by Ohata et al. [2011, 2013]. In this technique, the size-resolved number concentration of BC was measured by the SP2 after extraction of BC particles dispersed into the air from rainwater sample by the nebulizer. The size-resolved number concentration of BC in rainwater was estimated on the basis of

a size-dependent extraction efficiency ε , measured by using an aqueous suspension of monodisperse polystyrene latex spheres with known concentrations [Ohata et al., 2013]. The mass equivalent diameter of BC detectable by our SP2 [Moteki and Kondo, 2010] ranged from about 70 to 920 nm. An example of the number and mass size distribution of BC observed for rainwater collected at Hedo is shown in Figure A3.3.

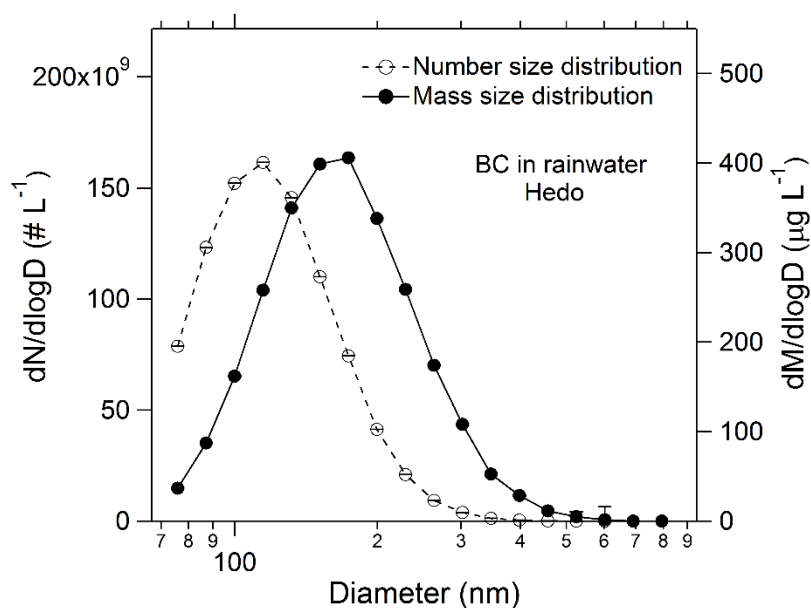


Figure A3.3. Number and mass size distribution of BC in rainwater at Cape Hedo on 7 March 2012. The values and vertical bars represent means and 1σ values of BC, respectively.

To quantify the possible loss of BC due to adhesion on the inner wall of the polystyrene bottle during storage in the refrigerator of the automated sampler (Figure A3.2a), the C_{BC} values and size distribution of BC in rainwater samples stored in the bottle before and after ultrasonic agitation for 15 min were compared. For 25 samples, C_{BC} was found to be 1.31 ± 0.31 times greater after ultrasonic agitation, and the BC number and mass size distribution did not change by agitation: namely, the count median diameter (CMD) and mass median diameter (MMD) differed by only about 1% on average. Rainwater samples collected between April 2010 and July 2012 were not agitated before the transfer from the polypropylene bottles to the glass bottles, and samples collected between August 2012 and March 2013 were agitated before transfer. Therefore, C_{BC} values were multiplied by a factor of 1.31 independent of BC size for the rainwater samples collected before July 2012.

In addition, possible sampling artifacts of the automated sampler were evaluated by comparing samples collected with a manual rain sampler (Figure A3.2b) positioned on the ground 15 m from the automated sampler. The manual rain sampler used a funnel and 100 mL bottle made of glass to minimize possible loss of BC on the inner wall. Rainwater was collected on a daily basis by both samplers on 13 days between August 2012 and March 2013.

Figure A3.4 shows the correlation of C_{BC} for the 13 rainwater samples collected by both the automated (C_{auto}) and manual samplers (C_{manu}). The mass concentrations were strongly correlated ($r^2 = 0.88$), and the slope of the correlation was 0.99. The average C_{auto}/C_{manu} ratio was 1.1 ± 0.3 (1σ), indicating that the C_{BC} for rainwater collected by the two samplers agreed to within 10%. The CMD and MMD for the 13 samples agreed to within 6%. These results indicate that the automated sampler can be used for BC analysis

without substantial artifacts. The overall accuracy of the C_{BC} data was estimated to be about 25% [Ohata et al., 2013].

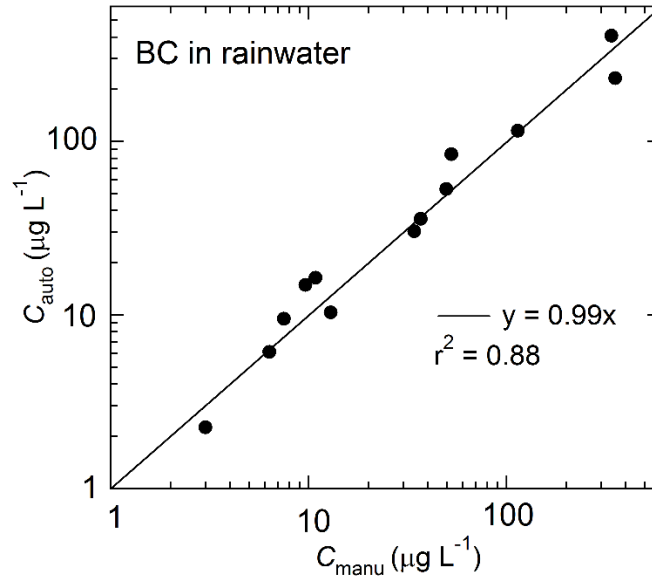


Figure A3.4. Correlation between mass concentrations of BC in rainwater as measured by the automated (C_{auto}) and manual samplers (C_{manu}). The line is the least squares fitted line.

A3.2.4. Calculation of BC Wet deposition

The BC wet deposition flux for the i th sampling event F_{BCi} ($\text{mg m}^{-2} \text{d}^{-1}$) was defined as

$$F_{BCi} = C_{BCi} \times P_i \quad (\text{A3.1})$$

where C_{BCi} is the mass concentration in rainwater and P_i (mm d^{-1}) is the amount of precipitation in this sampling event. To derive monthly BC wet deposition flux, it is necessary to take into account all the precipitation events, including rain events from which rainwater was not sampled. Considering this factor, monthly BC wet deposition flux F_{BC} in the units of $\text{mg m}^{-2} \text{ month}^{-1}$ was defined as

$$F_{BC} = \frac{1}{R} \sum_i F_{BCi} \quad (\text{A3.2})$$

Here the R value is the ratio of precipitation summed over all rain sampling events to total monthly precipitation P_{month} , independently measured at the sampling site:

$$R = \frac{1}{P_{month}} \sum_i P_i \quad (\text{A3.3})$$

The average seasonal value of R was higher than about 0.6 (Table A3.1). The R value was less than 0.4 in April 2010, July 2010, June 2011, September 2011, and January 2012.

A3.3. Results

A3.3.1. Meteorological Conditions

This section shows a review of typical meteorological conditions in East Asia and their relationship to transport of BC and precipitation in this region. Figure A3.5 shows surface weather maps at 0900 JST (0000 UTC) for 4 days that serve as typical examples of the respective seasons from spring to winter. Rainwater samples were collected on

these days. Plate 1 shows the corresponding infrared images obtained by Multifunctional Transport Satellite (<http://weather.is.kochi-u.ac.jp/>).

In spring, frequent occurrence of migratory cyclones and a stationary Bai-u (Meiyu) front cause persistent and occasionally enhanced precipitation over the East China Sea (Figure A3.5a and Plate 1a). The front plays an important role for the meridional transition of airflow between continental air from north and oceanic air from south. Linho and Wang. [2002] and Linho et al. [2008] have discussed the effect of the water vapor transport from the south on the South China Spring Rain in relation to the large-scale meteorological setting. During summer, the dominant subtropical anticyclone over the central North Pacific transports clean oceanic air masses from south (Figure A3.5b and Plate 1b). Previous studies have analyzed the variability in the timing of the onset of the summer monsoon in East Asia [Wang and Linho, 2001; LinHo and Wang, 2002; Yihui and Chan, 2005]. According to back trajectory analysis at Cape Hedo [Verma et al., 2011], maritime air masses constituted about 80% of the air masses sampled at Cape Hedo. Summer precipitation over Okinawa Island is mainly associated with cloud systems developed by thermal convection [Mikami et al., 2011]. In summer and fall, typhoons and tropical cyclones frequently pass over the East China Sea (Figure A3.5c and Plate 1c), causing heavy precipitation [Ueda et al., 1995]. During winter, the Siberian high dominates over the Asian continent, and continental air is frequently transported to the East China Sea in the winter monsoon (Figure A3.5d and Plate 1d). According to back trajectory analysis at Cape Hedo [Verma et al., 2011], about 50% of the air masses are transported from China.

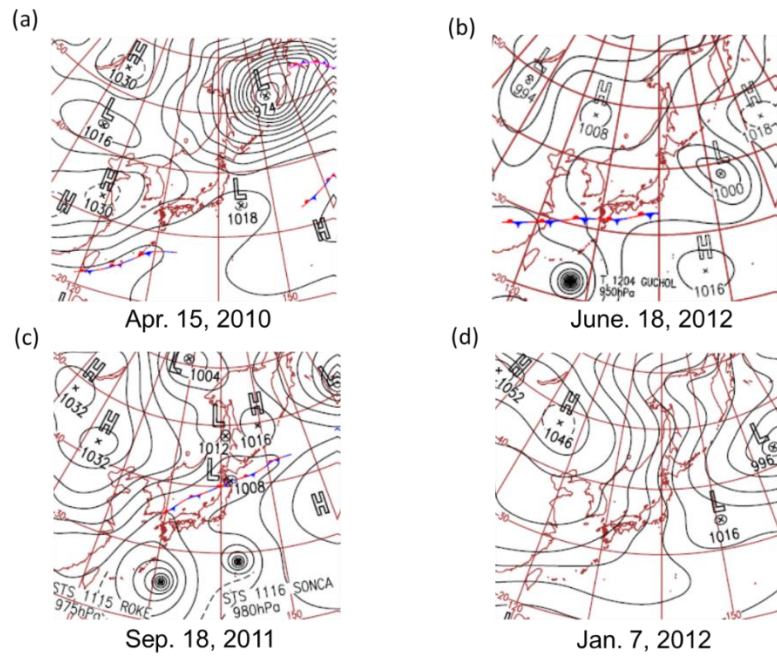


Figure A3.5. Surface weather maps of East Asia on (a) 15 April 2010, (b) 18 June 2012, (c) 18 September 2011, and (d) 7 January 2012 at 0900 local time.

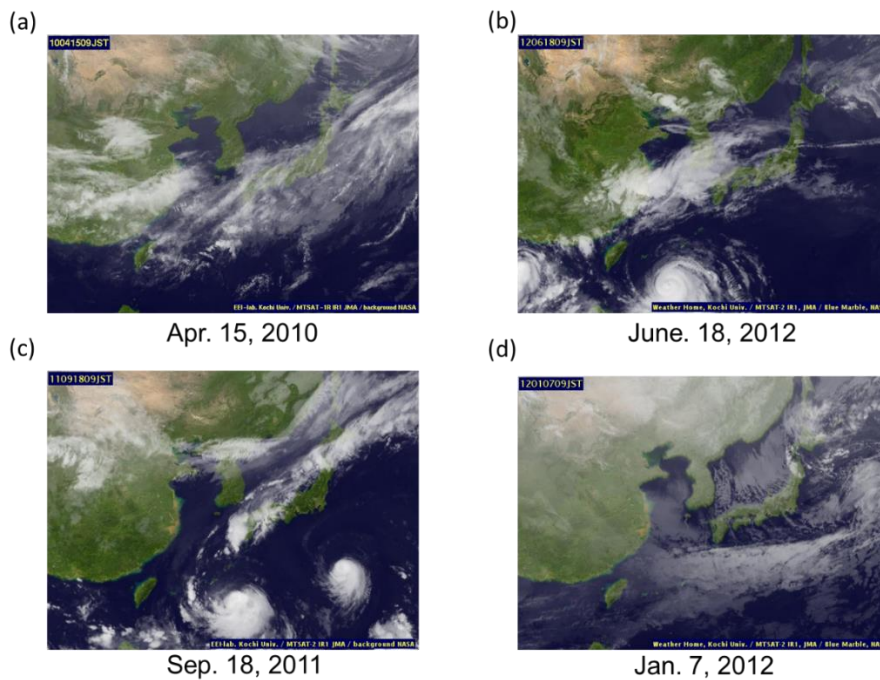


Plate 1. Infrared images from the geo stationary satellite Himawari for (a) 15 April 2010, (b) 18 June 2012, (c) 18 September 2011, and (d) 7 January 2012 around 0900 JST.

A3.3.2. Seasonal Variation of Precipitation

Figure A3.6 (bottom) shows the daily precipitation amount measured by a weather station (Vaisala WXT520) on the days that the rainwater samples were collected at Hedø. Figure A3.7 (bottom) shows the monthly precipitation amounts for 3 years. Precipitation was measured by a sensor that detects the impaction of individual raindrops. Averaged seasonal precipitation (Table A3.1) was largest in spring due to the presence of migratory cyclones and the Bai-u front over East Asia. During summer and fall, precipitation was caused mainly by typhoons and convective activities. During winter, precipitation was smallest because of the winter monsoon, which transported cold dry air masses.

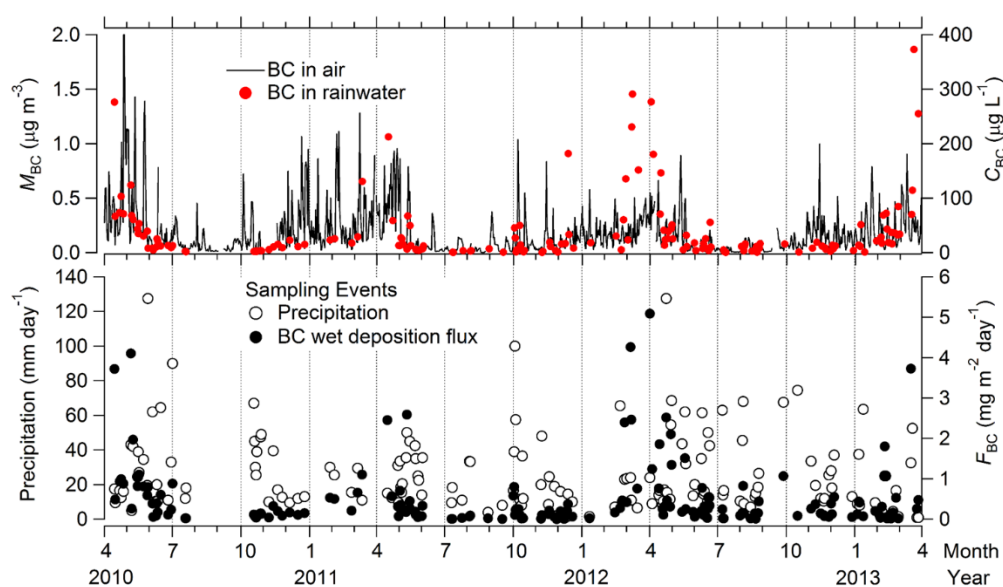


Figure A3.6. (top and bottom) Average daily BC mass concentrations in air (M_{BC}) and BC mass concentration in rainwater (C_{BC}) for each sample, daily precipitation, and daily BC wet deposition flux (F_{BC}) from April 2010 to March 2013. One C_{BC} value of $474 \mu\text{g L}^{-1}$ in March 2013 is not shown.

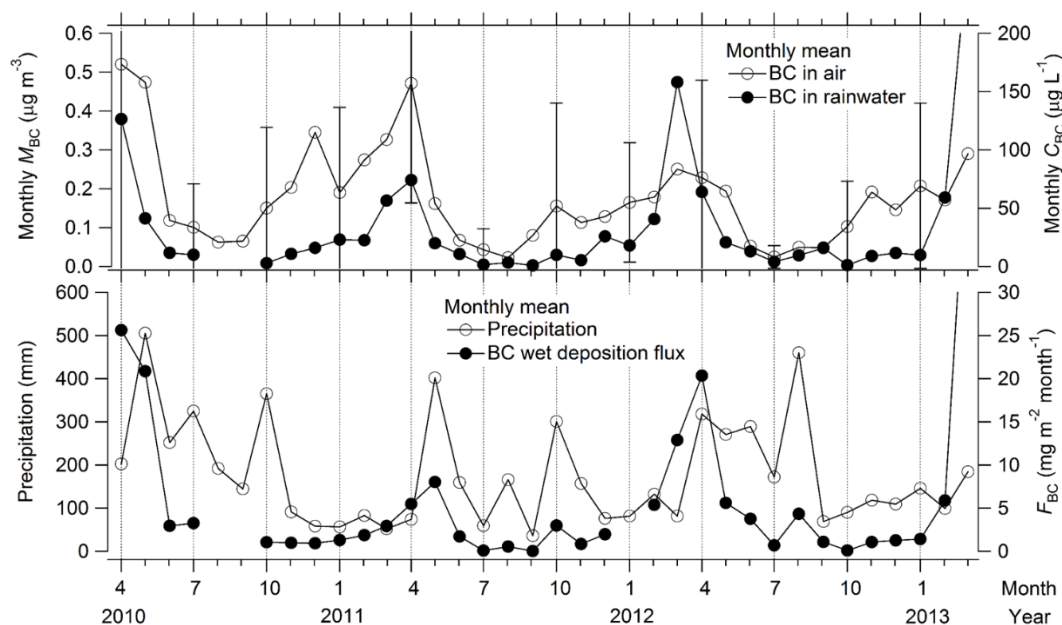


Figure A3.7. (top and bottom) Average monthly BC mass concentration in air (M_{BC}) and rainwater (C_{BC}), monthly precipitation, and monthly BC wet deposition flux (F_{BC}) from April 2010 to March 2013. Uncertainties ($\pm 1\sigma$) are shown for each 3 month season. The F_{BC} was calculated by using equation (A3.2). A C_{BC} value of $270 \mu\text{g L}^{-1}$ and a F_{BC} value of $50 \text{mg m}^{-2} \text{month}^{-1}$ for March 2013 are not shown.

Table A3.1. Average seasonal (± 1 Standard Deviation) values and ranges of M_{BC} and C_{BC} , total precipitation (P), the ratio (R) of all precipitation for sampling events to total monthly precipitation, and BC wet deposition flux (F_{BC}) measured at Cape Hedo from April 2010 to March 2013. Their annual values are also given.

Terms	Spring 2010–2013	Summer 2010–2013	Fall 2010–2013	Winter 2010–2013	Year 2010–2013
M_{BC} ($\mu\text{g m}^{-3}$) (Range)	0.32 ± 0.13 (0.0–4.0)	0.06 ± 0.03 (0.0–2.4)	0.12 ± 0.05 (0.0–1.8)	0.20 ± 0.06 (0.0–2.6)	0.18 ± 0.26 (0.0–4.0)
C_{BC} ($\mu\text{g L}^{-1}$) (Range)	92 ± 76 (4.1–474)	8.0 ± 4.1 (0.55–56)	7.0 ± 5.0 (0.61–50)	24 ± 13 (1.1–182)	33 ± 53 (0.55–474)
P (mm month ⁻¹)	232	231	152	94	177
R (Range)	0.73 ± 0.18 (0.36–0.96)	0.57 ± 0.22 (0.31–0.91)	0.80 ± 0.23 (0.22–0.98)	0.63 ± 0.27 (0.02–0.95)	0.65 ± 0.24 (0.02–0.98)
F_{BC} (mg m^{-2} month ⁻¹)	16.8 ± 6.7	1.9 ± 0.88	0.91 ± 0.27	2.2 ± 0.56	5.5 ± 9.9

A3.3.3. BC Mass Concentrations in Air and Rainwater

Figure A3.6 shows the time series of average daily M_{BC} , C_{BC} , P_i , and F_{BC} , and Figure A3.7 shows the corresponding monthly values. Monthly C_{BC} was derived by averaging daily C_{BC} values that were weighted by the daily P_i values. Monthly average F_{BC} was calculated by using equation (A3.2). Table A3.1 summarizes the monthly average values

of M_{BC} , C_{BC} , P , R , and F_{BC} for each season and their annual averages.

The monthly M_{BC} and C_{BC} values showed distinct seasonal variations, being highest in spring ($0.32 \pm 0.13 \mu\text{g m}^{-3}$ and $92 \pm 76 \mu\text{g L}^{-1}$, respectively) and lowest in summer ($0.06 \pm 0.03 \mu\text{g m}^{-3}$ and $8.0 \pm 4.1 \mu\text{g L}^{-1}$, respectively). The high M_{BC} values in winter and spring reflected frequent transport of Asian air masses with high M_{BC} with winter monsoon [Verma et al., 2011; Kondo et al., 2011a]. In spring, BC emissions from biomass burning contributed to the spring maximum of M_{BC} [Liu et al., 2013; Matsui et al., 2013]. During summer and fall, M_{BC} was lowest because of frequent transport of maritime air.

High C_{BC} values were associated with high M_{BC} in winter and spring. As shown in Figure A3.8, monthly C_{BC} values are well correlated with monthly M_{BC} ($r^2 = 0.58$). The monthly C_{BC} values for March of 2012 and 2013 were exceptionally high ($158 \mu\text{g L}^{-1}$ and $270 \mu\text{g L}^{-1}$, respectively), and these two data were excluded in calculating the slope and r^2 value of the correlation. The reasonably good correlation between C_{BC} and M_{BC} suggests that major sources of BC in rainwater typically were ambient BC in the planetary boundary layer (PBL). Higher M_{BC} would increase the absolute BC mass incorporated in rainwater during cloud precipitation processes, resulting in higher C_{BC} . However, C_{BC} can be influenced by BC distribution in areas beyond the vicinity of the measurement site. In fact, daily C_{BC} values for individual precipitation events were poorly correlated with the hourly M_{BC} values measured at 0 h ($r^2 = 0.15$), 3 h ($r^2 = 0.14$), and 6 h ($r^2 = 0.12$) before the beginning of precipitation. The absence of correlation on a daily time scale implies that the observed C_{BC} for individual rain events is not necessarily influenced by the local M_{BC} in the PBL.

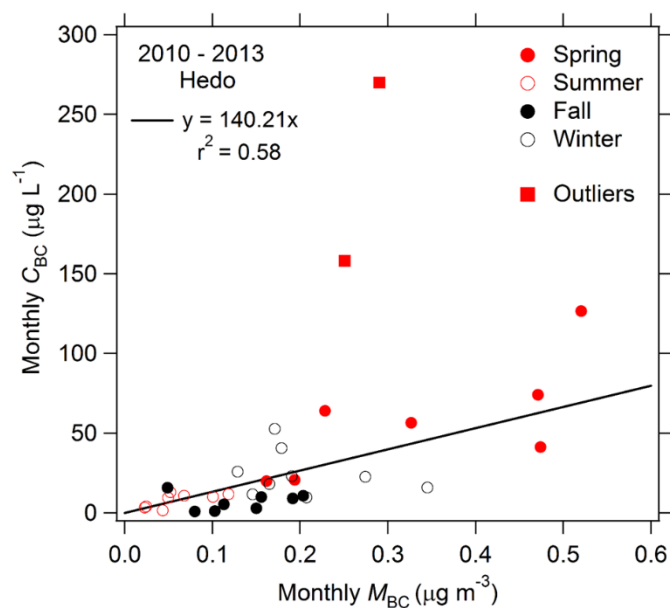


Figure A3.8. Correlation between the average monthly BC mass concentration in rainwater (C_{BC}) and air (M_{BC}) from April 2010 to March 2013. The line is the least squares fitted line. Two outliers for March 2012 and March 2013 (red squares) were not used for least squares fitting.

Table A3.2. Average (± 1 Standard deviation) BC emission flux, wet deposition flux, and net flux over North China (33–50°N, 100–130°E) and South China (20–33°N, 100–123°E) during March–May 2010

Place	Emission Flux ($\text{mg m}^{-2} \text{ month}^{-1}$)	Deposition Flux ($\text{mg m}^{-2} \text{ month}^{-1}$)	Net Flux ($\text{mg m}^{-2} \text{ month}^{-1}$)
North China	23 ± 32	6.6 ± 5.7	16 ± 33
South China	36 ± 32	28 ± 19	7.8 ± 37

A3.3.4. BC Wet Deposition Flux

F_{BC} values also showed marked seasonal variations, as shown in Figure A3.6 (bottom) and Table A3.1. F_{BC} was highest in spring as a result of high C_{BCi} and P_i . The total BC mass deposited per unit area in 1 year, denoted as DEP_{BC} (annual), was 66 mg m^{-2} ($= 5.5 \text{ mg m}^{-2} \text{ month}^{-1} \times 12$) and that for spring (DEP_{BC} (spring)) was 50 mg m^{-2} ($= 16.8 \text{ mg m}^{-2} \text{ month}^{-1} \times 3$) on average. From this,

$$DEP_{BC} \text{ (spring)}/DEP_{BC} \text{ (annual)} = 0.76 \quad (\text{A3.4})$$

meaning that about 76% of the annual BC deposition occurred in spring on average. F_{BC} values in fall were very low because C_{BC} values were much lower than in winter and spring. F_{BC} in winter was comparable to values in summer, although the C_{BC} was higher by a factor of 3, because the P_{month} value was lower by nearly the same factor.

Estimated BC emission fluxes over the Asian continent were compared with those observed at Hedo in spring. Table A3.2 summarizes the average BC emission flux, wet deposition flux, and net flux over North China (33° – 50° N, 100° – 130° E) and South China (20° – 33° N, 100° – 123° E) for March–May 2010, calculated by CMAQ-PASCAL based on the emission data of Zhang et al. [2009]. The estimated monthly average BC emission flux was $23 \pm 32 \text{ mg m}^{-2} \text{ month}^{-1}$ in North China and $36 \pm 32 \text{ mg m}^{-2} \text{ month}^{-1}$ in South China. The wet deposition flux over South China was larger by a factor of 4 than that over North China because of the greater precipitation rate (Figure A3.1c). It is noted that the net flux (emission–deposition) over North China ($16 \pm 33 \text{ mg m}^{-2} \text{ month}^{-1}$) is similar to F_{BC} observed at Hedo ($16.8 \pm 6.7 \text{ mg m}^{-2} \text{ month}^{-1}$) during spring. The BC wet deposition flux in the region surrounding Hedo is estimated to be rather uniform according to the

model calculation (Figure A3.1d). Considering this, the present observation demonstrates the importance of precipitation over the East China Sea as a large sink of BC transported from China during spring.

Considering the dominance of BC wet deposition during spring, a more detailed analysis of the meteorological conditions was made in this season. Our analysis was similar to that of Oshima et al. [2013] for spring of 2009, using the National Centers for Environmental Prediction (NCEP) Final (FNL) Operational Global Analysis data during March–May 2010. Figure A3.9 shows the mean values of sea level pressure and horizontal winds at the 850 hPa level, convective available potential energy (CAPE), equivalent potential temperature and southern moisture transport at the 850 hPa level, and precipitable water. CAPE is well known as an indicator of vertical instability [Chen and Lin, 2005].

The low-level circulation (850 hPa level) over North China was characterized by the monsoonal northwesterly flow or westerly flow, whereas South China was under the influence of persistent southerlies (Figure A3.9a), which advected warm moist air into a frontal zone that extended zonally around 30°N. The frontal zone was marked by sharp meridional gradients in equivalent potential temperature (Figure A3.9c). The distinct latitudinal variations in water vapor content (Figure A3.9d) and CAPE values (Figure A3.9b) around the frontal zone contribute to a large amount of precipitation that extended toward the northeast along Japanese archipelago (Figure A3.1c). Thus, the springtime meteorological regime leads to transport of high-BC air masses from North China to latitudes of about 30°N over the East China Sea, where BC is removed efficiently from the atmosphere by precipitation associated with the frontal activities.

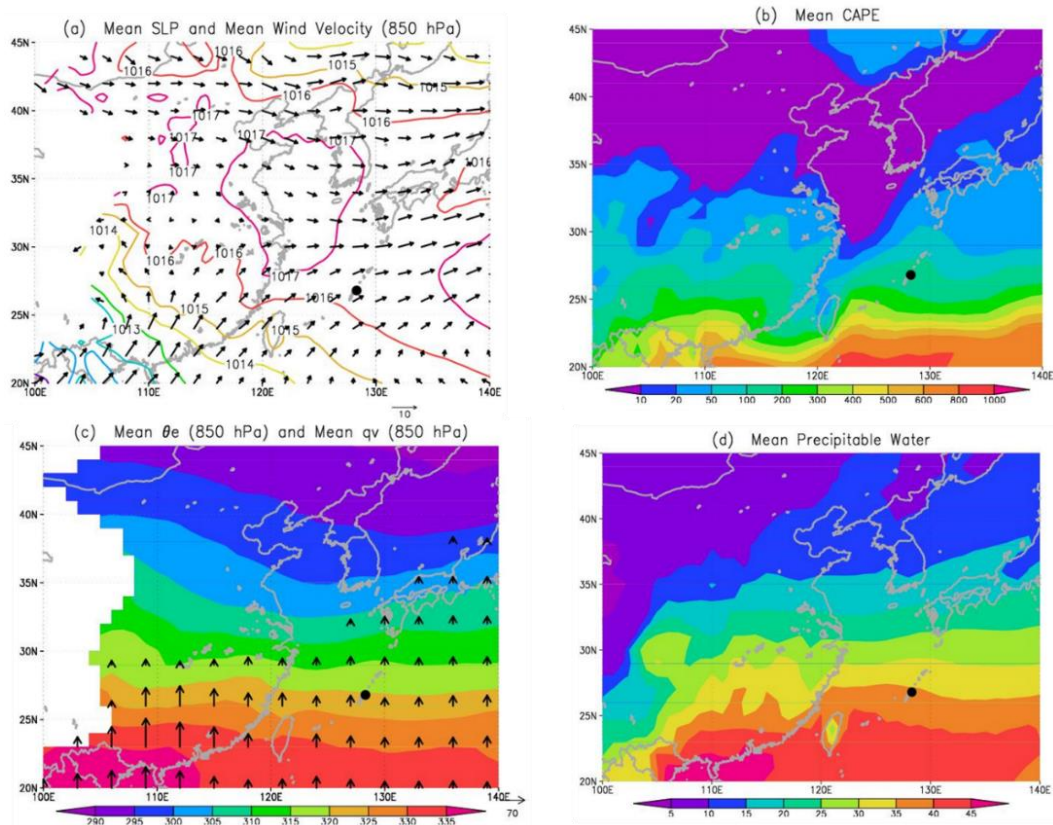


Figure A3.9. Mean meteorological fields over East Asia for March–May 2010 based on NCEP FNL data. (a) Mean sea level pressure (hPa, contours) and mean horizontal winds (m s^{-1} , vectors) at the 850 hPa level. (b) Mean convective available potential energy (CAPE) (J kg^{-1}). (c) Mean equivalent potential temperature θ_e (K) and southern moisture transport at the 850 hPa level (qv values, in $\text{m s}^{-1} \text{g Kg}^{-1}$, shown as vectors with values less than 10 not shown). (d) Mean precipitable water (kg m^{-2}). Regions without data correspond to regions with high altitude mountains.

A3.3.5. Size Distribution of BC in Rainwater

The size distributions of BC in rainwater were measured by using our SP2. Evaporation of water droplets produced in the nebulizer can cause BC particles in the droplet to coagulate, whereby BC size increases as the BC concentrations in water increase [Ohata et al., 2011]. The correction for this effect in determining the BC size distributions was made by using the results of Ohata et al. [2011]. Table A3.3 summarizes the average seasonal CMD, geometric standard deviations for number size distributions (σ_{gn}), MMD, and geometric standard deviations for mass size distributions (σ_{gm}) for rain samples collected at Hedo from April 2010 to March 2013. The average seasonal MMD was lowest in spring (163 ± 11 nm) and highest in winter (179 ± 18 nm). The size distributions of BC in rainwater sampled at Hedo were stable to within about 15 nm. The difference in MMD between spring and winter may result from higher supersaturation in cloud-forming processes during spring or from higher CCN activity of BC during spring; however, there is no observational evidence to support these hypotheses.

The CMD of BC in rainwater observed at Hedo (Table A3.3) was similar to that observed in Tokyo in December 2010 (CMD = 98 nm and $\sigma_{gn} = 1.60$) [Ohata et al., 2011]. The MMD observed at Hedo was lower than that in Tokyo (MMD = 191 nm and $\sigma_{gm} = 1.59$). The thickness of the coating on BC particles over the East China Sea [Shiraiwa et al., 2008] was much greater than that in Tokyo [Kondo et al., 2011b], such that BC at Hedo had a higher CCN activity for a given supersaturation. This may explain the difference in MMD at the two locations.

Table A3.3. Average seasonal (± 1 Standard deviation) values and ranges of CMD, geometric standard deviations (σ_{gn}) for number size distributions, MMD, and geometric standard deviations (σ_{gm}) for mass size distributions for rain samples collected at Cape Hedo from April 2010 to March 2013

Season	CMD (nm)	σ_{gn}	MMD (nm)	σ_{gm}
Spring	101 \pm 10 (78–144)	1.51 \pm 0.10 (1.33–1.71)	163 \pm 11 (132–191)	1.48 \pm 0.04 (1.40–1.62)
Summer	109 \pm 17 (80–147)	1.46 \pm 0.07 (1.34–1.64)	170 \pm 17 (146–224)	1.53 \pm 0.07 (1.44–1.80)
Fall	100 \pm 11 (77–118)	1.50 \pm 0.08 (1.36–1.73)	169 \pm 13 (147–197)	1.53 \pm 0.06 (1.45–1.67)
Winter	106 \pm 14 (85–135)	1.52 \pm 0.07 (1.40–1.67)	179 \pm 18 (132–210)	1.50 \pm 0.04 (1.43–1.57)

A3.4. Processes Controlling BC in Rainwater

A3.4.1. Local Convection

The C_{BC} and M_{BC} values in precipitation were poorly correlated on a day-to-day basis, possibly because C_{BC} was influenced by nonlocalized M_{BC} , as discussed above. This section examines the relationship of these quantities for precipitation associated with local convection using a one-dimensional theoretical model to estimate C_{BC} from the observed M_{BC} , water vapor content (m_v), and the vertical thermodynamic structure of the

atmosphere.

Summertime precipitation often comes from cloud systems developed by thermal convection [Mikami et al, 2011]. Therefore, the data from summer were selected. C_{BC} was poorly correlated with M_{BC} measured 1 h before the start of rain ($r^2 = 0.12$) in the total data set from summer months of 2010–2013. Further, the selection of precipitation events in which CAPE was positive several hours before rain began was conducted.

The vertical structure of the atmosphere over Hedo was analyzed with 6 h resolution by using the NCEP FNL data. For the selected events, the NCEP water vapor mixing ratio (w_v) values were strongly correlated with those observed at the surface site (with a slope of 0.99 and $r^2 = 0.86$). The pressures at equilibrium level (EL) and CAPE (defined as the hatched area on the Skew-T diagram shown in Figure A3.10) were estimated, using the environmental temperature and air mass temperature as a function of water vapor pressure at the surface. Table A3.4 summarizes the pressures at EL and CAPE values for convective events, defined as those with positive CAPE. The average value of CAPE in the summer data set was $1093 \pm 755 \text{ J kg}^{-1}$, satisfying the necessary condition for strong convection.

Figure A3.11 shows the correlation between C_{BC} and M_{BC} in the full summer data set. For the summer data with positive CAPE, the correlation was much stronger ($r^2 = 0.47$) than that for all summer data ($r^2 = 0.12$) and that for all data from all seasons ($r^2 = 0.08$). The improvement in r^2 is qualitatively consistent with our hypothesis that C_{BC} strongly depends on M_{BC} for localized convection in summer.

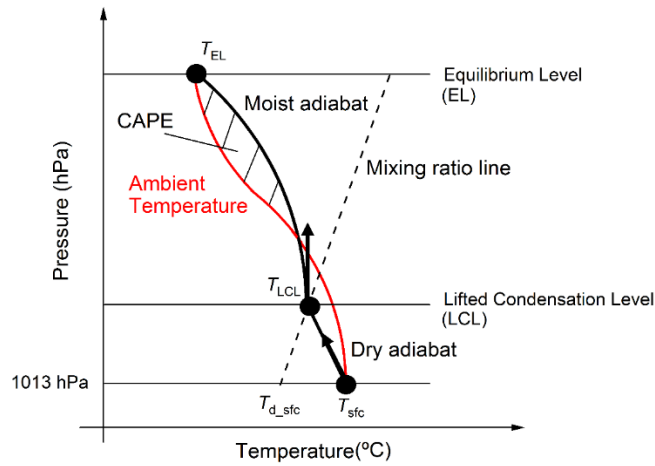


Figure A3.10. Skew-T diagram representing the thermodynamic state of the atmosphere. Red line denotes the ambient temperature, and solid black line denotes the temperature in an air parcel lifted from the surface (sfc) at 1013 hPa to the equilibrium level (EL). Dotted line represents the mixing ratio line. Hatched area represents the convective available potential energy (CAPE).

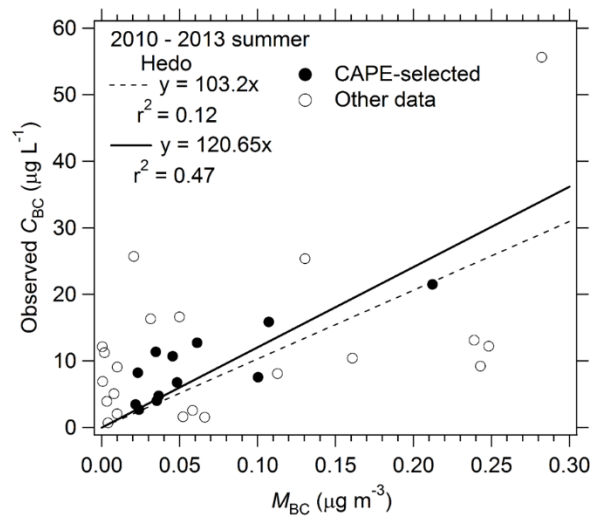


Figure A3.11. Correlation between BC mass concentrations in rainwater (C_{BC}) and in air (M_{BC}) during 2010–2013 summers at Cape Hedo.

Table A3.4 Pressure at equilibrium level (EL) and CAPE during summer months of 2010–2013 during convective events

Date	Pressure at EL (hPa)	CAPE (J kg^{-1})
5/6/2010	326.5	36.8
9/6/2010	728.5	17.2
11/6/2010	231.4	355.0
1/7/2010	149.4	2386.5
10/6/2012	192.7	513.9
18/6/2012	167.6	793.7
19/6/2012	180.7	797.5
1/8/2012	146.2	1881.9
4/8/2012	140.3	1429.6
6/8/2012	145.6	1385.7
15/8/2012	146.6	1522.2
25/8/2012	142.7	2003.3
Average	225 ± 160	1093 ± 755

A3.4.2. Estimates of C_{BC} by Thermodynamic Model

A simplified theoretical model was used to predict C_{BC} (*Estimated C_{BC}*) from values of surface M_{BC} and m_v just before the start of precipitation. This model used four assumptions: (1) the mass mixing ratios of BC and water in an air parcel were conserved during its adiabatic lifting from surface level to the EL (Figure A3.10), (2) all of the BC-containing particles in the air parcel acted as CCN and were incorporated into liquid water above the lifting condensation level (LCL), (3) the mass of rainwater produced in the air parcel was derived by subtracting equilibrium water vapor at the EL from the total water content of the air parcel, and (4) the mass of rainwater determined at the EL was not reduced by evaporation during the falling process before sampling at the surface. Given these assumptions, C_{BC} is estimated in our model as

$$\text{Estimated } C_{BC} = \frac{M_{BC}}{m_v \times WCR} \quad (\text{A3.5})$$

where M_{BC} ($\mu\text{g m}^{-3}$) and m_v (g m^{-3}) are hourly averages just before precipitation and water condensation ratio WCR is the mass fraction of water vapor converted to rainwater in the air parcel (the calculation method is presented in section A4.2). The product of m_v and WCR equals the rainwater mass concentration m_l in the air parcel.

$$m_l = m_v \times WCR \quad (\text{A3.6})$$

To test our model for estimating C_{BC} by equation (A3.5), the estimated C_{BC} was compared with the observed C_{BC} (Figure A3.12). The correlation between the estimated and observed C_{BC} is stronger ($r^2 = 0.68$) than the observed C_{BC} - M_{BC} correlation ($r^2 = 0.47$).

This improvement in correlation suggests that the rainwater mass, as well as M_{BC} , is also an important controlling factor of C_{BC} in each rain event.

For the CAPE-selected data set, the average values of m_v , WCR , and m_l were $21 \pm 1.7 \text{ g m}^{-3}$, 0.98 ± 0.033 , and $21 \pm 1.4 \text{ g m}^{-3}$, respectively. The low variance of m_l led to the high C_{BC} - M_{BC} correlation for this data set. The estimated C_{BC} values were smaller than observed C_{BC} values by about a factor 3 (Figure A3.12). This discrepancy may arise, for example, from precipitation occurring at altitudes lower than EL. A more quantitative analysis will require more sophisticated numerical simulations of the wet removal process of BC.

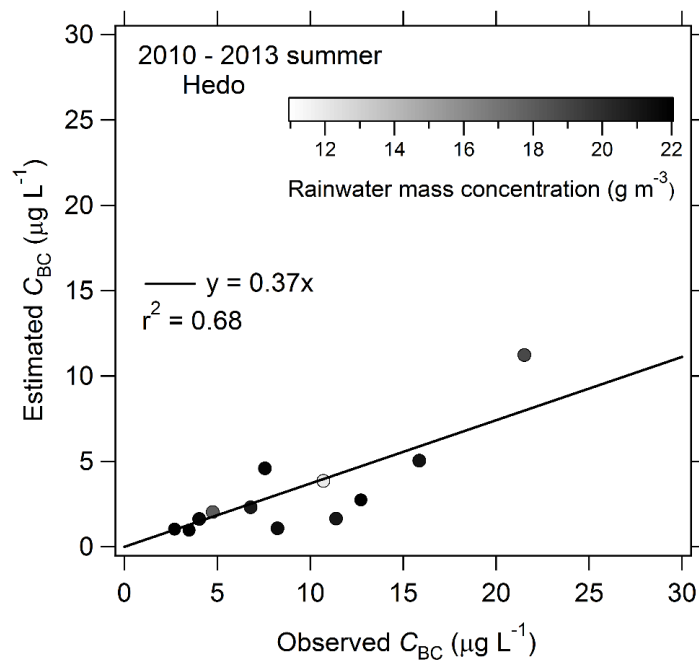


Figure A3.12. Correlation between calculated and observed BC mass concentrations in rainwater for the summers of 2010–2013 with least squares fitted line. The rainwater mass concentration m_l calculated with NCEP data is also depicted.

This model to the CAPE-selected data set for the spring season was also applied. As the average value of CAPE was $275 \pm 215 \text{ J kg}^{-1}$, the atmosphere was marginally unstable. The average values of m_v , WCR , and m_l were $25 \pm 3.0 \text{ g m}^{-3}$, 0.76 ± 0.24 , and $19 \pm 6.5 \text{ g m}^{-3}$, respectively. The estimated C_{BC} value was not correlated with the observed C_{BC} value ($r^2 = 0.04$). The variance of m_l for spring is about 34%, much higher than that for summer of about 7%, leading to poorer correlation. The larger variance also suggests that the assumption of local convection may not apply for spring. In fall and winter, there were few positive CAPE events, reflecting much weaker solar heating of the surface.

A3.5. Summary

BC mass concentrations in surface air (M_{BC}) and rainwater (C_{BC}) simultaneously were made at Cape Hedo in Okinawa Island for 3 years (April 2010 to March 2013) with accuracies of about 10% and 25%, respectively. The monthly M_{BC} and C_{BC} values showed marked seasonal variations, being highest in spring ($0.32 \pm 0.13 \text{ } \mu\text{g m}^{-3}$ and $92 \pm 76 \text{ } \mu\text{g L}^{-1}$, respectively) and lowest in summer ($0.06 \pm 0.03 \text{ } \mu\text{g m}^{-3}$ and $8.0 \pm 4.1 \text{ } \mu\text{g L}^{-1}$, respectively). The average M_{BC} and C_{BC} were well correlated ($r^2 = 0.58$).

The high value of C_{BC} in spring was caused by M_{BC} transported from the Asian continent by monsoonal northwesterly winds. The wet deposition flux of BC (F_{BC}), calculated as the product of C_{BC} and precipitation, also showed distinct seasonal variations. The monthly average F_{BC} during the four spring seasons ($16.8 \pm 6.7 \text{ mg m}^{-2} \text{ month}^{-1}$) was about 3 times higher than the annual average F_{BC} ($5.5 \pm 9.9 \text{ mg m}^{-2} \text{ month}^{-1}$) owing to the high C_{BC} and precipitation amount (about $230 \text{ mm month}^{-1}$) in spring, which is comparable to the value for summer. As a result, about 76% of the annual BC deposition occurred in spring on average.

The observed F_{BC} value at Hedo was close to the net emission flux of BC in North China (33–50°N). The regional model predicts very low F_{BC} in North China as a result of low precipitation in spring. It is likely that a substantial fraction of BC emitted in this region is transported to latitudes south of 33°N, where precipitation is much higher. This analysis points out the importance of precipitation along the Bai-u frontal system as an efficient removal mechanism for BC transported from North China.

The correlation of C_{BC} and M_{BC} was poor for individual precipitation events. The correlation greatly improved for summertime local convective events with positive CAPE values. A one-dimensional model was developed to predict C_{BC} from M_{BC} , water vapor content at the surface, and vertical thermodynamic structure of the atmosphere. For CAPE-selected summer events, the calculated C_{BC} was highly correlated ($r^2 = 0.68$) with observed values, suggesting that M_{BC} in the PBL strongly influenced C_{BC} .

Appendix A4

A4.1. Automated Wet-Only Sampler

The automated wet-only sampler consists of a stainless steel shelter (H180 × W90 × D65 cm), a rain collector, and a rain sensor. The rainwater collector funnel (20 cm maximum diameter) was made of stainless steel coated with Teflon. The lid of the sampler opened automatically when the rain sensor detected raindrops larger than approximately 0.5 mm in diameter. Rainwater collected during A34 h period starting at 0900 JST was fed through a Teflon tube into a polypropylene bottle. After collection, each bottle was stored in a refrigerator at 5°C for up to 2 weeks as shown in Figure A3.2a. The lid was closed while rain was not falling to keep out dry deposition of gases and particles. In addition, the funnel and the Teflon tube were washed automatically with pure water at 0900 JST every day.

A4.2. Method to Calculate WCR

We explain the procedure for calculating the mass fraction of water vapor transformed to rain water (WCR) in an air parcel, an important parameter in our model to estimate C_{BC} (equation (A3.5) in the text). The total water mixing ratio (w_{tot}) and BC mixing ratio (w_{BC}) in the air parcel are defined as

$$w_{tot} \equiv \frac{m_v}{m_d} \quad w_{BC} \equiv \frac{M_{BC}}{m_d} \quad (\text{A4.1})$$

where m_v , M_{BC} , and m_d are mass concentrations of water vapor, BC, and dry air, respectively. As w_{tot} is assumed to be conserved from the surface to the equilibrium level (EL), it is expressed as

$$w_{tot} = w_v + w_l \quad (\text{A4.2})$$

where w_v and w_l are mixing ratios of water vapor and liquid water, respectively; w_{tot} is equal to w_v below the lifting condensation level (LCL) because w_l is zero. WCR is defined at the EL as

$$WCR = \frac{w_l(\text{EL})}{w_{tot}} \quad (\text{A4.3})$$

To determine EL, we calculated temperature versus pressure for the moist air parcel over a trajectory between the surface and the upper troposphere (~200 hPa), assuming adiabatic change. The calculated temperature profile was compared with the ambient temperature profile given by the NCEP data, as illustrated in Figure A3.10. For internal consistency, we also used NCEP data for w_{tot} and the initial temperature and pressure of the air parcel at the surface. First, we calculated the LCL, the pressure level at which the saturation water vapor mixing ratio agrees with w_{tot} . EL was calculated as the level where moist adiabat (starting from the LCL) intersects the ambient profile according to the NCEP data (Figure A3.10). We calculated liquid water mixing ratio at the EL as

$$w_l(\text{EL}) = w_{tot} - w_v(\text{EL}) \quad (\text{A4.4})$$

where the water vapor mixing ratio at the EL, $w_v(\text{EL})$, is defined as the saturation water vapor mixing ratio at the temperature and pressure of the EL. WCR is determined by

substituting equation (A4.4) into equation (A4.3).

REFERENCES

- Adachi, K., S. H. Chung, and P. R. Buseck (2010), Shapes of soot aerosol particles and implications for their effects on climate, *J. Geophys. Res.*, 115, D15206, doi:10.1029/2009JD012868.
- Armališ, S. (1999), Wet deposition of elemental carbon in Lithuania, *Sci. Total Environ.*, 239, 89–93.
- Baron, P. A., and K. Willeke (2001), *Aerosol measurement: Principles, Techniques and applications*.
- Bauer, S. E., D. L. Wright, D. Koch, E. R. Lewis, R. McGraw, L.-S. Chang, S. E. Schwartz, and R. Ruedy (2008), MATRIX (Multiconfiguration Aerosol TRacker of mIXing state): an aerosol microphysical module for global atmospheric models, *Atmos Chem and Phys.*, 8, 6003–6035.
- Bohren, C. F., and D. R. Huffman (1983), *Absorption and Scattering of Light by Small Particles*, John Wiley and Son, New York.
- Bond, T.C., et al. (2013), Bounding the role of black carbon in the climate system: A scientific assessment, *J. Geophys. Res. Atmos.*, 118, 1–173, doi:10.1002/jgrd.50171.
- Cerqueira, M., C. Pio, M. Legrand, H. Puxbaum, A. Kasper-Giebl, J. Afonso, S. Preunkert, A. Gelencsér, and P. Fialho (2010), Particulate carbon in precipitation at European background sites, *J. Aerosol Sci.*, 41, 51–61.
- Chen, S. H., and Y. L. Lin (2005), Effects of moist Froude number and CAPE on a conditionally unstable flow over a mesoscale mountain ridge, *J. Atmos. Sci.*, 62, 331–350.
- Chýlek, P., L. Kou, B. Johnson, F. Boudala, and G. Lesins (1999), Black carbon concentrations in precipitation and near surface air in and near Halifax, Nova Scotia.

- Atmos Environ.*, 33, 2269–2277.
- Dasch, J. M., and S. H. Cadle (1989), Atmospheric carbon particles in an urban area: Wintertime sources and sinks, *Aerosol Sci. Technol.*, 10, 236–248.
- DeCarlo, P. F., J. G. Slowik, D. R. Worsnop, P. Davidovits, and J. L. Jimenez (2004), Particle morphology and density characterization by combined mobility and aerodynamic diameter measurements. Part 1: Theory, *Aerosol Sci. Technol.*, 38(12), 1185–1205.
- D’Errico, M., C. Cagnazzo, P. G. Fogli, W. K. M. Lau, J. von Hardenberg, F. Fierli, and A. Cherchi (2015), Indian monsoon and the elevated-heat-pump mechanism in a coupled aerosol-climate model, *J. Geophys. Res. Atmos.*, 120, 8712–8723, doi:10.1002/2015JD023346.
- Donner, L. J., et al, (2011), The dynamical core, physical parameterizations, and basic simulation characteristics of the atmospheric component AM3 of the GFDL global coupled model CM3, *Journal of Climate*, 24(13), 3484–3519, doi:10.1175/2011JCLI3955.1.
- Ducret, J., and H. Cachier (1992), Particulate carbon in rain at various temperate and tropical locations, *J. Atmos. Chem.*, 15, 55–67.
- Dubovik, O., B. Holben, T.F. Eck, A. Smirnov, Y. J. Kaufman, M. D. King, D. Tanre, and L. Slutsker (2002), Variability of absorption and optical properties of key aerosol types observed in worldwide locations, *J. Geophys. Res. Atmos.*, 59(3), 590–608, doi:10.1175/1520-0469(2002)059<0590:VOAAOP>2.0.CO;2.
- Ehara, K., C. Hagwood, and K. J. Coakley (1996), Novel method to classify aerosol particles according to their mass-to-charge ratio—aerosol particle mass analyser. *Journal of Aerosol Science.*, 27(2), 217–234.

- Feingold, G., and A. J. Heymsfield (1992), Parameterizations of condensational growth of droplets for use in general circulation models, *J. Atmos. Sci.*, *49*(23), 2325–2342.
- Feingold, G. (2003), Modeling of the first indirect effect: Analysis of measurement requirements, *Geophysical research letters.*, *30*(19).
- Flossmann, A. I., W. D. Hall, and H. R. Pruppacher (1985), A theoretical study of the wet removal of atmospheric pollutants. Part I: Their distribution of aerosol particles captured through nucleation and impaction scavenging by growing cloud drops, *J. Atmos. Sci.*, *42*, 583–606.
- Flossmann, A. I., and W. Wobrock (2010), A review of our understanding of the aerosol–cloud interaction from the perspective of a bin resolved cloud scale modelling, *Atmos Res.*, *97*(4), 478–497, doi:10.1016/j.atmosres.2010.05.008.
- Fountoukis, C., et al. (2007), Aerosol–cloud drop concentration closure for clouds sampled during the International Consortium for Atmospheric Research on Transport and Transformation 2004 campaign, *J. Geophys. Res.*, *112*, D10S30, doi:10.1029/2006JD007272.
- Fujita, S., A. Takahashi, J. H. Weng, L. F. Huang, H. K. Kim, C. K. Li, F. T. C. Huang, and F. T. Jeng (2000), Precipitation chemistry in East Asia. *Atmos. Environ.*, *34*, 525–537.
- Hadley, O. L., C. E. Corrigan, and T. W. Kirchstetter (2008), Modified thermal-optical analysis using spectral absorption selectivity to distinguish black carbon from pyrolyzed organic carbon, *Environ. Sci. Technol.*, *42*, 8459–8464.
- Hadley, O. L., and T. W. Kirchstetter (2012), Black-carbon reduction of snow albedo, *Nature Climate Change.*, *2*(6), 437–440.
- Hodnebrog, Ø., G. Myhre, and B. H. Samset (2014), How shorter black carbon lifetime

- alters its climate effect. *Nature communications* 5.,5065, DOI:10.1038/ncomms6065.
- Hoshi, J., S. Amano, Y. Sasaki, and T. Korenaga (2008), Investigation and estimation of emission sources of 54 volatile organic compounds in ambient air in Tokyo, *Atmospheric Environment*, 42(10), 2383–2393.
- Intergovernmental Panel on Climate Change (2013), *IPCC Fifth Assessment Report: Climate Change 2013.*, Cambridge, Univ. Press, Cambridge, U. K.
- Jayne, J. T., D. C. Leard, X. Zhang, P. Davidovits, K. A. Smith, C. E. Kolb, and D. R. Worsnop (2000), Development of an aerosol mass spectrometer for size and composition analysis of submicron particles, *Aerosol Sci. Technol.*, 33(1-2), 49–70, doi: 10.1080/027868200410840.
- Jacobson, M. Z. (2000), Physically-based treatment of elemental carbon optics: Implications for global direct forcing of aerosols, *Geophysical Research Letters.*, 27(2), 217–220.
- Jacobson, M. Z. (2001), Strong radiative heating due to the mixing state of black carbon in atmospheric aerosols. *Nature.*, 409, 6821.
- Kondo, Y., L. Sahu, M. Kuwata, Y. Miyazaki, N. Takegawa, N. Moteki, J. Imaru, S. Han, T. Nakayama, N. T. Kim Oanh, M. Hu, Y. J. Kim, and K. Kita (2009), Stabilization of the mass absorption cross section of black carbon for filter-based absorption photometry by the use of a heated inlet, *Aerosol Sci. Technol.*, 43, 741–756.
- Kondo, Y., N. Oshima, M. Kajino, R. Mikami, N. Moteki, N. Takegawa, R. L. Verma, Y. Kajii, S. Kato, and A. Takami (2011a), Emissions of black carbon in East Asia estimated from observations at a remote site in East China Sea, *J. Geophys. Res.*, 116, D16201, doi:10.1029/2011JD015637.
- Kondo, Y., L. Sahu, N. Moteki, F. Khan, N. Takegawa, X. Liu, M. Koike, and T.

- Miyakawa (2011b), Consistency and traceability of black carbon measurements made by laser-induced incandescence, thermal-optical transmission, and filter-based photo-absorption techniques, *Aerosol Sci. Technol.*, 45, 295–312, doi:10.1080/02786826.2010.533215.
- Kondo, Y., N. Moteki, N. Oshima, S. Ohata, M. Koike, Y. Shibano, N. Takegawa, and K. Kita (2016), Effects of wet deposition on the abundance and size distribution of black carbon in East Asia, *J. Geophys. Res. Atmos.*, 121, 4691–4712, doi:10.1002/2015JD024479.
- Kuwata, M., Y. Kondo, M. Mochida, N. Takegawa, and K. Kawamura (2007), Dependence of CCN activity of less volatile particles on the amount of coating observed in Tokyo, *J. Geophys. Res.*, 112, D11207, doi: 10.1029/2006JD007758.
- Kuwata, M., Y. Kondo, Y. Miyazaki, Y. Komazaki, J. H. Kim, S. S. Yum, H. Tanimoto, and H. Matsueda (2008), Cloud condensation nuclei activity at Jeju Island, Korea in spring 2005, *Atmos. Chem. Phys.*, 8, 2933–2948.
- Kuwata, M., Y. Kondo, and N. Takegawa (2009), Critical condensed mass for activation of black carbon as cloud condensation nuclei, *J. Geophys. Res.*, 114, D20202, doi: 10.1029/2009JD012086.
- Laborde, M., P. Mertes, P. Zieger, J. Dommen, U. Baltensperger, and M. Gysel (2012), Sensitivity of the Single Particle Soot Photometer to different black carbon types, *Aerosol Sci. Technol.*, 5, 1031–1043.
- Lamarque, J. F, et al. (2012), CAM-chem: Description and evaluation of interactive atmospheric chemistry in the Community Earth System Model, *Geosci. Model. Dev.*, 5, 369–411.
- Lim, S., X. Fäin, M. Zanatta, J. Cozic, J. L. Jaffrezo, P. Ginot, and P. Laj (2014),

- Refractory black carbon mass concentrations in snow and ice: Method evaluation and inter-comparison with elemental carbon measurement, *Atmos. Meas. Tech.*, 7, 3307–3324, doi:10.5194/amt-7-3307-2014.
- Linho and B. Wang (2002), The time-space structure of the Asian-Pacific summer monsoon: A fast annual cycle view, *J. Climate.*, 15(15), 2001–2019.
- Linho, L. H., X. Huang, and N-C. Lau (2008), Winter-to-spring transition in East Asia: A planetary-scale perspective of the South China spring rain onset, *J. Climate*, 21(13), 3081–3096.
- Liu, X., et al. (2013), Seasonal variations of black carbon observed at the remote mountain site Happo in Japan, *J. Geophys. Res. Atmos.*, 118, 3709–3722, doi:10.1002/jgrd.50317.
- Lohmann, U, and J. Feichter (2005), Global indirect aerosol effects: a review, *Atmos Chem and Physics.*, 5(3), 715–737.
- Matsui, H, and M. Koike (2012), New source and process apportionment method using a three-dimensional chemical transport model: Process, Age, and Source region Chasing ALgorithm (PASCAL), *Atmos. Environ.*, 55, 399–409, doi:10.1016/j.atmosenv.2012.02.080.
- Matsui, H., M. Koike, Y. Kondo, N. Moteki, J. D. Fast, and R. A. Zaveri (2013a), Development and validation of a black carbon mixing state resolved three-dimensional model: Aging processes and radiative impact, *J. Geophys. Res. Atmos.*, 118, 2304–2326, doi:10.1029/2012JD018446.
- Matsui, H., M. Koike, Y. Kondo, N. Oshima, N. Moteki, Y. Kanaya, A. Takami, and M. Irwin (2013b), Seasonal variations of Asian black carbon outflow to the Pacific: Contribution from anthropogenic sources in China and biomass burning sources in

- Siberia and Southeast Asia, *J. Geophys. Res. Atmos.*, 118, 9948–9967, doi:10.1002/jgrd.50702.
- Matsui, H., M. Koike, Y. Kondo, and J. D. Fast (2014), Development of an aerosol microphysical module: Aerosol Two-dimensional bin module for foRmation and Aging Simulation (ATRAS), *Atmos. Chem. Phys.*, 14, 10315–10331.
- McConnell, J. R., R. Edwards, G. L. Kok, M. G. Flanner, C. S. Zender, E. S. Saltzman, J. R. Banta, D. R. Pasteris, M. M. Carter, and J. D. W. Kahl (2007), 20th-century industrial black carbon emissions altered arctic climate forcing, *Science.*, 317, 1381–1384, doi:10.1126/science.1144856.
- Menon, S., J. Hansen, L. Nazarenko, and Y. Luo (2002), Climate effects of black carbon aerosols in China and India, *Science.*, 297, 5590, 2250–2253.
- Mikami, A., T. Kawabata, S. Satoh, J. Furumoto, S. Nagai, Y. Murayama, and T. Tsuda (2011), Meso- γ -scale convective systems observed by a 443-MHz wind-profiling radar with RASS in the Okinawa subtropical region, *J. Atmos. Solar-Terrestrial Phys.*, 73, 996–1009.
- Ming, Y., V. Ramaswamy, and G. Persad (2010), Two opposing effects of absorbing aerosols on global-mean precipitation, *Geophys. Res. Lett.*, 37, L13701, doi:10.1029/2010GL042895.
- Miyazaki, Y., Y. Kondo, N. Takegawa, Y. Komazaki, M. Fukuda, K. Kawamura, M. Mochida, K. Okuzawa, and R. J. Weber (2006), Time-resolved measurements of water-soluble organic carbon in Tokyo, *J. Geophys. Res.*, 111, D23206, doi:10.1029/2006JD007125.
- Mochida, M., C. Nishita-Hara, Y. Kitamori, S. G. Aggarwal, K. Kawamura, K. Miura, and A. Takami (2010), Size-segregated measurements of cloud condensation nucleus

- activity and hygroscopic growth for aerosols at Cape Hedo, Japan, in spring 2008, *J. Geophys. Res.*, 115, D21207, doi:10.1029/2009JD013216.
- Mori, T., Y. Kondo, S. Ohata, N. Moteki, H. Matsui, N. Oshima, and A. Iwasaki (2014), Wet deposition of black carbon at a remote site in the East China Sea. *J. Geophys. Res. Atmos.*, 119, 1716, 10485–10498, doi:10.1002/2014JD022103.
- Mori, T., N. Moteki, S. Ohata, M. Koike, K. Goto-Azuma, Y. Miyazaki, and Y. Kondo (2016), Improved technique for measuring the size distribution of black carbon particles in liquid water, *Aerosol Sci. Technol.*, 50(3), 242–254.
- Moteki, N., Y. Kondo, Y. Miyazaki, N. Takegawa, Y. Komazaki, G. Kurata, T. Shirai, D. R. Blake, T. Miyakawa, and M. Koike (2007), Evolution of mixing state of black carbon particles: Aircraft measurements over the western Pacific in March (2004), *Geophys. Res. Lett.*, 34, L11803, doi:10.1029/2006GL028943.
- Moteki, N., and Y. Kondo (2008), Method to measure time-dependent scattering cross sections of particles evaporating in a laser beam, *J. Aerosol Sci.*, 39(4), 348–364.
- Moteki, N., and Y. Kondo (2010), Dependence of laser-induced incandescence on physical properties of black carbon aerosols: Measurements and theoretical interpretation, *Aerosol Sci. Technol.*, 44, 663–675.
- Moteki, N., Y. Kondo, and S. Nakamura (2010), Method to measure refractive indices of small nonspherical particles: Application to black carbon particles, *J. Aerosol Sci.*, 41, 513–521.
- Moteki, N., Y. Kondo, N. Oshima, N. Takegawa, M. Koike, K. Kita, H. Matsui, and M. Kajino (2012), Size dependence of wet removal of black carbon aerosols during transport from the boundary layer to the free troposphere, *Geophys. Res. Letter.*, 39, L13802, doi:10.1029/2012GL052034.

- Moteki, N., and T. Mori (2015), Theoretical analysis of a method to measure size distributions of solid particles in water by aerosolization, *J. Aerosol Sci.*, 83, 25–31, doi:10.1016/j.jaerosci.2015.02.002.
- Ogren J. A., P. J. Groblicki, and R. J. Charlson (1984), Measurement of the removal rate of elemental carbon from the atmosphere, *Sci. Total. Environ.*, 36, 329–338.
- Ohata, S., N. Moteki, and Y. Kondo (2011), Evaluation of a method for measurement of the concentration and size distribution of black carbon particles suspended in rainwater, *Aerosol Sci. Technol.*, 45, 1326–1336.
- Ohata, S., N. Moteki, J. Schwarz, D. Fahey, and Y. Kondo (2013), Evaluation of a method to measure black carbon particles suspended in rainwater and snow samples, *Aerosol Sci. Technol.*, 47, 1073–1082.
- Ohata, S., J. P. Schwarz, N. Moteki, M. Koike, A. Takami, and Y. Kondo (2016a), Hygroscopicity of materials internally mixed with black carbon measured in Tokyo, *J. Geophys. Res. Atmos.*, 121, 362–381, doi:10.1002/2015JD024153.
- Ohata S., N. Moteki, T. Mori, M. Koike, and Y. Kondo (2016b). A key process controlling the wet removal of aerosols: new observational evidence, *Nature Sci. Rep.*, 6, 34113, DOI: 10.1038/srep34113.
- Orsini, D., Y. Ma, A. Sullivan, B. Sierau, K. Baumann, and R. Weber (2003), Refinements to the particle–into–liquid sampler (PILS) for ground and airborne measurements of water soluble aerosol composition, *Atmos. Environ.*, 37, 1243–1259, doi:10.1016/S1352-2310(02)01015-4.
- Oshima, N., M. Koike, Y. Zhang, Y. Kondo, N. Moteki, N. Takegawa, and Y. Miyazaki (2009), Aging of black carbon in outflow from anthropogenic sources using a mixing state resolved model: Model development and evaluation, *J. Geophys. Res.*, 114,

- D06210, doi:10.1029/2008JD010680.
- Oshima, N., and M. Koike (2013), Development of a parameterization of black carbon aging for use in general circulation models, *Geosci. Model Dev*, 6(2), 263–282.
- Park, K., D. B. Kittelson, and P. H. McMurry (2004), Structural properties of diesel exhaust particles measured by transmission electron microscopy (TEM): Relationships to particle mass and mobility, *Aerosol Sci. Technol.*, 38(9), 881–889.
- Park, R. J., et al. (2005), Export efficiency of black carbon aerosol in continental outflow: Global implications, *J. Geophys. Res. Atmos.*, 110(D11).
- Pendergrass, A. G., and D. L. Hartmann (2012), Global-mean precipitation and black carbon in AR4 simulations, *Geophys. Res. Lett.*, 39, L01703, doi:10.1029/2011GL050067.
- Petters, M. D., and S. M. Kreidenweis (2007), A single parameter representation of hygroscopic growth and cloud condensation nucleus activity. *Atmos. Chem. Phys.*, 7(8), 1961–1971, doi:10.5194/acp-7-1961-2007.
- Riemer, N., M. West, R. A. Zaveri, and R. C. Easter (2009), Simulating the evolution of soot mixing state with a particle-resolved aerosol model, *J. Geophys. Res.*, 114, D09202, doi:10.1029/2008JD011073.
- Riemer, N., M. West, R. A. Zaveri, and R. C. Easter (2010), Estimating soot aging time scales with a particle-resolved aerosol model, *J. Aerosol Sci.*, 41, 143–158.
- Samset, B. H. et al. (2014), Modelled black carbon radiative forcing and atmospheric lifetime in AeroCom Phase II constrained by aircraft observations, *Atmos. Chem. Phys.*, 14, 22, 12465–12477.
- Sato, Y., H. Miura, H. Yashiro, D. Goto, T. Takemura, H. Tomita, and T. Nakajima (2016), Unrealistically pristine air in the Arctic produced by current global scale

- models, *Scientific Reports.*, 6, 26561.
- Schwarz, J. P., S. J. Doherty, F. Li, S. T. Ruggiero, C. E. Tanner, A. E. Perring, R. S. Gao, and D. W. Fahey (2012), Assessing single particle soot photometer and integrating sphere/integrating sandwich spectrophotometer measurement techniques for quantifying black carbon concentration in snow, *Atmos. Meas. Tech.*, 5, 2581–2592, doi:10.5194/amt-5-2581-2012.
- Schwarz, J. P., R. S. Gao, A. E. Perring, J. R. Spackman, and D. W. Fahey (2013), Black carbon aerosol size in snow, *Nature Sci. Rep.*, 3, 1356, doi:10.1038/srep01356.
- Seinfeld, J. H., and S. N. Pandis (2006), *Atmospheric chemistry and physics*. John Wiley & Sons, New York.
- Shiraiwa, M., Y. Kondo, N. Moteki, N. Takegawa, L. Sahu, A. Takami, S. Hatakeyama, S. Yonemura, and D. Blake (2008), Radiative impact of mixing state of black carbon aerosol in Asian outflow, *J. Geophys. Res.*, 113, D24210.
- Stephens, M., N. Turner, and J. Sandberg (2003), Particle identification by laser-induced incandescence in a solid-state laser cavity, *Appl. Opt.*, 42, 3726–3736.
- Tajima, N., N. Fukushima, K. Ehara, and H. Sakurai (2011), Mass range and optimized operation of the aerosol particle mass analyzer, *Aerosol Sci. Technol.*, 45(2), 196–214.
- Takegawa, N., et al. (2006), Seasonal and diurnal variations of submicron organic aerosol in Tokyo observed using the Aerodyne aerosol mass spectrometer, *J. Geophys. Res. Atmos.*, 111, D11, doi: 10.1029/2005JD006515.
- Takami, A., T. Miyoshi, A. Shimono, N. Kaneyasu, S. Kato, Y. Kajii, and S. Hatakeyama (2007), Transport of anthropogenic aerosols from Asia and subsequent chemical transformation, *J. Geophys. Res.*, 112, D22S31, doi:10.1029/2006JD008120.
- Tang, M. J., R. A. Cox, and M. Kalberer (2014), Compilation and evaluation of gas phase

- diffusion coefficients of reactive trace gases in the atmosphere: volume 1. Inorganic compounds. *Atmos. Chem. Phys.*, 14, 9233–9247.
- Taylor, J. W., et al. (2014), Size-dependent wet removal of black carbon in Canadian biomass burning plumes, *Atmos. Chem. Phys.*, 14, 13755–13771.
- Textor, C., et al. (2006), Analysis and quantification of the diversities of aerosol life cycles within AeroCom, *Atmos. Chem. Phys.*, 6(7), 1777–1813.
- Twomey, S (1974), Pollution and the planetary albedo, *Atmos. Environ.*, 8(12), 1251–1256.
- Ueda, H., T. Yasunari, and R. Kawamura (1995), Abrupt seasonal change of large-scale convection activity over the western Pacific in northern summer, *J. Meteor. Soc. Japan.*, 73, 795–809.
- Verma, R. L., Y. Kondo, N. Oshima, H. Matsui, K. Kita, L. K. Sahu, S. Kato, Y. Kajii, A. Takami, and T. Miyakawa (2011), Seasonal variations of the transport of black carbon and carbon monoxide from the Asian continent to the western Pacific in the boundary layer, *J. Geophys. Res.*, 116, D21307, doi:10.1029/2011JD015830.
- Wang, B., and L. H. Linho (2001), Rainy of the Asian-Pacific summer monsoon, *J. Climate.*, 15, 386–398.
- Wang, X., L. Zhang, and M. Moran (2010), Uncertainty assessment of current size-resolved parameterizations for below-cloud particle scavenging by rain. *Atmos. Chem. Phys.*, 10, 12, 5685–5705.
- Warren, S. G., and W. J. Wiscombe (1980), A Model for the Spectral Albedo of Snow, II, Snow Containing Atmospheric Aerosols, *J. Atmos. Sci.*, 37, 2734–2745.
- Weber, R. J., D. Orsini, Y. Daun, Y. -N. Lee, P. J. Klotz, and F. Brechtel (2001), A particle-into-liquid collector for rapid measurement of aerosol bulk chemical composition, *Aerosol Sci. Technol.*, 35, 718–727.

- Wendl, I. A., J. A. Menking, R. Färber, M. Gysel, S. D. Kaspari, M. J. G. Laborde, and M. Schwikowski (2014), Optimized method for black carbon analysis in ice and snow using the single particle soot photometer. *Atmos. Meas. Tech.*, 7, 2667–2681, doi:10.5194/amt-7-2667-2014.
- Yasunari, T. J., R. D. Koster, W. K. M. Lau, and K.-M. Kim (2015), Impact of snow darkening via dust, black carbon, and organic carbon on boreal spring climate in the Earth system, *J. Geophys. Res. Atmos.*, 120, 5485–5503, doi:10.1002/2014JD022977.
- Yihui, D., and J. C. L. Chan (2005), The East Asian summer monsoon: An overview, *Meteorol. Atmos. Phys.*, 89, 117–142, doi 10.1007/s00703-005-0125-z.
- Zaveri, R. A., J. C. Barnard, R. C. Easter, N. Riemer, and M. West (2010), Particle-resolved simulation of aerosol size, composition, mixing state, and the associated optical and cloud condensation nuclei activation properties in an evolving urban plume, *J. Geophys. Res.*, 115, D17210, doi:10.1029/2009JD013616.
- Zhang, Q., et al. (2009), Asian emissions in 2006 for the NASA INTEX-B mission, *Atmos. Chem. Phys.*, 9, 5131–5153.

Acknowledgments

I am deeply grateful to Prof. Y. Kondo at National Institute of Polar Research (NIPR) for his continuing support and encouragement during the course of my study. I also deeply grateful to Prof. M. Koike and Dr. N. Moteki at the Earth and Planetary Science (EPS), the University of Tokyo, for invaluable advice and encouragement throughout my study. I would like to Dr. S. Ohata, at EPS, the University of Tokyo, for insightful comments and suggestions on my study. I would also like to thank Prof. K. Goto-Azuma at NIPR, Dr. N. Oshima at Meteorological Research Institute (MRI), and Dr. H. Matsui at Nagoya University, Prof. Y. Miyazaki at Institute of Low Temperature Science, Hokkaido University for generous supports and various suggestions from during the course of my study. I want to thank many researchers at MRI, National Institute for Environmental Studies, and Japan Agency for Marine-Earth Science and Technology, who are BC-CARE field observation campaign participants at Tokyo and Okinawa, for their corporation and support on my study. I gratefully acknowledge Cape Hedo Atmosphere and Aerosol Monitoring Station (CHAAMS) for the acquisition of precious observation data. I received generous support from many researchers in Okinawa Prefectural Institute of Health and Environment for collecting the rain samples. I wish to appreciate Prof. R. Tada, Prof. Y. Sekine at EPS, the University of Tokyo, Prof. K. Suzuki, and Prof. M. Uematsu at Atmosphere and Ocean Research Institute, the University of Tokyo, for their insightful comments and suggestions on my study. Finally, I would also like to show my greatest appreciation to my family.

I was supported by Japan Society for the Promotion of Science (JSPS) KAKENHI Grant Number JP16J04452.

Publication List

Mori, T., Y. Kondo, S. Ohata, N. Moteki, H. Matsui, N. Oshima, and A. Iwasaki (2014), Wet deposition of black carbon at a remote site in the East China Sea, *J. Geophys. Res. Atmos.*, *119*, 17, 10485–10498, doi:10.1002/2014JD022103.

Moteki, N., and **T. Mori**, (2015). Theoretical analysis of a method to measure size distributions of solid particles in water by aerosolization. *J. Aerosol Sci.* *83*, 25–31, doi:10.1016/j.jaerosci.2015.02.002.

Mori, T., N. Moteki, S. Ohata, M. Koike, K. Goto-Azuma, Y. Miyazaki, and Y. Kondo (2016). Improved technique for measuring the size distribution of black carbon particles in liquid water. *Aerosol Sci. Technol.*, *50*, 3, 242–254, doi:10.1080/02786826.2016.1147644.

Yoshida, A., N. Moteki, S. Ohata, **T. Mori**, R. Tada, P. Dagsson-W, and Y. Kondo (2016), Detection of light-absorbing iron oxide particles using a modified single-particle soot photometer. *Aerosol Sci. Technol. letter.*, *50*, 3, doi:10.1080/02786826.2016.1146402.

Sho Ohata., N. Moteki, **T. Mori**, M. Koike, and Y. Kondo (2016). A key process controlling the wet removal of aerosols: new observational evidence, *Science Reports.*, *6*, 34113, doi: 10.1038/srep34113.

論文の内容の要旨

論文題目 Observational studies on wet deposition mechanism of black carbon particles

(ブラックカーボン粒子の湿性除去メカニズムの観測的研究)

氏 名 森 樹 大

1. 背景と目的

化石燃料やバイオマスの燃焼に伴い放出される炭素性エアロゾルの一種であるブラックカーボン (BC) は太陽光を効率的に吸収し、メタンに次ぐ正の放射強制力を持つと推定されている。さらに、水循環や極域雪氷面の融解速度にも影響を及ぼす。現在の数値モデル群では、対流圏中の BC 質量濃度の空間分布の予測値が異なるモデル間で1桁以上異なるため、BC による気候影響評価の不確実性は極めて大きい。BC 空間分布のモデル予測における最大の不確実要因の一つは、湿潤対流に伴う BC の湿性除去(と鉛直輸送)過程について、計算資源的な制約から大幅に簡略化した計算手法が用いられていることである。湿性除去過程の再現性能に優れた数値モデルを設計する土台として、実大気の間々の湿潤対流セルにおいて BC 湿性除去効率を決める主な因子が何であるのか、観測から具体的に理解しておくことが必要である。

本研究では、地上大気中と降水中の BC の粒径別数濃度分布の同時観測と雲パーセルモデルを組み合わせた新たなアプローチにより、個々の降水イベントで BC の湿性除去効率とその支配因子の解明を試みる。

2. 手法

本研究では、水中に分散する BC 粒子の粒径別数濃度の測定法を初めて確立した。さらに、BC 粒子の分裂や凝集による粒径変化は、雲粒・降水粒子・捕集した降水試料・分析装置内で起こらないことを実験的・理論的に確かめた。これにより、降水試料中と地上大気中の BC

粒径別数濃度の定量的比較が可能となり、初めて BC の除去効率の粒径依存性を観測できるようになった。

降水している雲の中でエアロゾルの除去の効率を決定するのはエアロゾルが水滴（雲粒または雨粒）に取り込まれる段階であり、これは（1）雲粒化、（2）雲粒との衝突、（3）雨粒との衝突の3種のメカニズムのうちいずれかによって起こりうる。BC 粒子の水滴取り込み効率の粒径依存性は、これら3種のメカニズムで著しく異なることから、観測された BC の除去効率の粒径依存性にに基づき、実際の降水雲の中で、どの取り込みメカニズムがどの程度寄与しているのかを解析することができる。

2.1. 観測手法

空気中に浮遊する BC の粒径別数濃度と、他のエアロゾル成分による BC 粒子の被覆の厚さは、レーザー誘起白熱法（SP2）を用いて測定した。本研究では、検出光学系の改良により SP2 の BC 粒径検出上限を従来の 850nm から 4000nm まで拡張した。

降水中の BC を空気中に取り出して SP2 で測定するために、水試料を噴霧乾燥させてエアロゾルを抽出する装置（粒子抽出装置）を用いる。本研究では、近年製品化された同軸型空気流噴霧方式の粒子抽出装置について、実験・理論的な性能評価を初めて行い、粒径 2000 nm 以下の BC を一様な効率 50%で取り出せることを確かめた。

これらの測定法を用いて、地上大気中と降水中の BC の粒径別数濃度の同時測定を行い、BC の湿性除去効率の粒径依存性を観測した。

2.2. データ解析手法

観測された湿性除去効率の粒径依存性にに基づき、除去された BC 粒子が経験した水滴取り込みメカニズムとして、（1）雲粒化、（2）雲粒との衝突、（3）雨粒との衝突のうちどれがどの程度寄与したのかを解析するため、雲パーセルモデルを用いたデータ解析手法を開発した。

この解析手法では、直接観測できない上昇流と雲中滞在時間の2変数の値を仮定し、パーセルの中で起こる3種の取り込みメカニズムの寄与を順的に計算する。そして、計算される BC 除去効率の粒径依存性が観測結果の一致するような上昇流と雲中滞在時間の値の組み合わせ、多数の試行計算を繰り返すことで経験的に探る。探索に成功すれば、取り込みメカニズムごとの寄与率を決定できる。上昇流と雲中滞在時間以外に入力パラメータ（エアロゾル濃度や雨粒の粒径別濃度など）の多くは、観測値を与えている。

3. 観測と結果

発生直後のエイジングが進んでいない汚染空気を観測できる東京（本郷キャンパス）と中国起源のエイジングした汚染空気を観測できる沖縄（辺戸岬）において連続観測を行った。東京では湿性除去効率に顕著な粒径依存性が見られるイベントが多く、沖縄では多くのイ

ベントで粒径依存性がほとんど見られなかった。この観測された除去効率の粒径依存性に基づき、3種の水滴取り込みメカニズムのそれぞれの寄与を解析した結果、質量濃度の大部分を占める粒径 100nm 以上の BC では、支配的なメカニズムは雲粒化であることを示した。エイジングに伴い BC の周りの被覆がある程度厚くなると（シェルコア比 $> \sim 1.2$ ）、被覆成分の変動幅や最大過飽和度の変動幅によらず、高い効率で除去されることがわかった。エイジングが進んでいない東京大気中のような裸に近い BC（シェルコア比 < 1.2 ）では、被覆量と被覆成分の変動や最大過飽和度の変動に依存して除去効率が大きく変わることがわかった。

4. 結論

降水性の雲において、雲粒化が主に BC の除去効率を支配するメカニズムであることを明らかにした。除去効率の値は、エイジングが進んだ被覆の厚い BC 粒子（シェルコア比 > 1.2 ）では、被覆成分や最大過飽和度の変動範囲内で、ほぼ 1 である（完全に除去される）ことがわかった。一方、エイジングが進んでいない都市大気などの BC（シェルコア比 < 1.2 ）では、除去効率は被覆成分や最大過飽和度に依存して大きく変動することがわかった。

本研究で解明した、BC 湿性除去効率の支配因子についての定量的知見は、BC 湿性除去過程のモデリング手法の改良するための土台として役に立つと考えられる。